STRUCTURAL AND PHOTOPHYSICAL CONSIDERATIONS OF SINGLET FISSION ORGANIC THIN FILMS FOR SOLAR PHOTOCHEMSITRY

By

Joseph L. Ryerson

B.A. Chemistry, University of Colorado Boulder, 2009

A thesis submitted to the

Faculty of the Graduate School of the

University of Colorado in partial fulfillment

of the requirements for the degree of

Doctor of Philosophy

Department of Chemistry & Biochemistry

2016

This thesis entitled:

Structural and Photophysical Considerations of Singlet Fission

Organic Thin Films for Solar Photochemistry

written by Joseph L. Ryerson

has been approved for the Department of Chemistry and Biochemistry

_____

Arthur J. Nozik

_____

Justin C. Johnson

*Date*_____

The final copy of this thesis has been examined by the signatories, and we find that both the content and the form meet acceptable presentation standards of scholarly work in the above mentioned discipline.

Ryerson, Joseph L. (Ph.D., Chemsitry)

Structural and Photophysical Considerations of Singlet Fission Organic Thin Films for Solar Photochemsitry

Thesis directed by Research Professor, Senior Research Fellow Emeritus, Arthur J. Nozik

Abstract text:

Singlet fission (SF) is a multichromophore charge multiplication process in organic systems in which a singlet exciton shares its energy with a neighboring chromophore, thus generating two triplet excitons from one photon. SF chromophores can boost photocurrent in solar cells, raising the maximum theoretical power conversion efficiency of a single-junction solar cell from ~33% to ~45. Thin film (TF) preparation techniques,steady-stateand time-resolved spectroscopic methods, and numerous advanced calculations were used to study the three systems presented here, all of which exhibit polymorphism.

TFs of 1,3-diphenylisobenzofuran (**1**), were prepared and two polymorphs, α-**1** and β-**1,** were discovered and characterized. α-**1**films exhibit $\Phi_T$near 200% and low Φ_F, whereas the dominant photophysical processes in the β-**1** polymorph are prompt and excimer emissions, with Φ_T around 10%. Absorption fitting revealed that the S_1 state of β-**1** is lower than α-**1**, and therefore SF and the correlated triplet ^{1}(TT) is energetically inaccessible to β-**1**. The SF mechanism in TFs of each polymorph is outlined in great detail.

Polymorphism in tetracene (Tc), a near 200% Φ_T SF material, has been previously documented, although morphology considerations have been neglected. While crystallite size has been shown to affect dynamics, the two Tc polymorphs, I and II, have not been analyzed in a

thorough comparison of dynamics and photophysics. Tc II films show SF rates that are independent of crystallite size and SF occurs more rapidly than in Tc I. The slower Tc I SF rates are highly dependent on grain size. Coupling calculations suggested that Tc I should be faster, but these calculations are limited,and more sophisticated, multimolecule calculations are needed to support experimental results.

Two extremely stable indigo derivatives, Cibalackrot (**2**) and a tert-butylated derivative(**3**) were structurally and photophysically characterized in solution and in TFs. Two crystalline polymorphs (**2α**, **2β**) and an amorphous phase (**2a**), as well as a crystalline (**3α**) and amorphous (**3a**) phase of **3** were deposited by thermal evaporation. Φ_T values of less than 25% were observed for all morphologies, except in 2β(Φ_T= 50%). Excimer formation dominates relaxation pathways in TFs of **2** and **3**.

Acknowledgements

First I would like to thank my mother, Benita Oechsli, for raising me with ambition, love, encouragement, high expectations, hard work ethic, and a "Shred 'em!" mentality. She is a strong-willed and powerful woman, whom I have the utmost respect for, and I owe much of my confidence and compassion to the example she set. I would also like to thank my sisters, Ava and Maria Ryerson for their incredible support and artistic contributions to this world. They bring true beauty and amazing spirituality to this world, one which is unrivaled in my experiences. They have helped shape me into the gentleman and scholar I am today, and have provided endless advice, counseling, and love during tough times, and I will always value our Trifecta. I would also like to thank Margo Josephs, as she has taught me many lessons about strength, love, personal growth, compassion, and relationships. I would like to thank my advisor, Art Nozik, for his technical and personal guidance throughout my thesis work, always encouraging me to think outside the box and pursue my own agenda, and to keep in mind the big picture, without losing sight of the ultimate motivation of my work. Next, and most significantly, I would like to thank Justin Johnson. He has offered guidance, expertise, advice, and lab snacks since day one at NREL. My success and progress would not have been possible without his patience, wisdom, astounding intelligence, organization, and collaborative spirit. I would like to thank Joel Schrauben for being a great lab mate, and for always being down to rock out and play music after a long day in a dark laser lab. I would also like to thank Dylan Arias for his care-free, stress-free demeanor, love of soccer and beverages, and also for his data wizardry that was essential in so much of this work. I would like to thank Todd Deutsch for seeing my potential, hiring me as a SULI, introducing me to the NRELian culture, and for all those powder days and amazing concerts at Red Rocks. I would like to thank John Turner for encouraging

Hawaiian shirts at all possible formal events. I would also like to thank Linda Lung for making possible my attendance and talk at an international ECS meeting, and for encouraging the use of 3D glasses, professional development, and pursuit of a graduate degree (and ukuleles). I would like to thank Garry Rumbles for his leadership of the program, securing of funding, and general comic relief and jovial spirit. I would like to thank Jeff Blackburn, Nate Neale, and Jao van de Lagemaat for their management skills, diligence, and expert advice. I would like to thank Josef Michl for his pivotal role during the graduate application process, as well as for invaluable research experience working in his group, and finally for several years of fruitful and incredibly productive collaboration. I would also like to thank Paul Dron for all of the hard work on synthesis of unreasonable amounts of compounds and patience with insoluble compounds, and for patiently waiting for results from my end. I would like to thank Pance Naumov, Subash Sahoo, Simon Teat, Bohdan Schatschneider, E. Głowacki, Mihai Irimia-Vladu, and Uwe Monkowius for crystal characterization and Zdenek Havlas, A. Wahab, and J. Ludvík for many valuable calculations. I would like to thank Niels Damrauer for a rewarding collaboration, for his great sense of humor, and for many productive conversations regarding experiments, calculations, and manuscript revisions. I would like to thank Brian Stepp for his early work on Cibalackrot, and for guidance in my early days as a researcher working in the Michl Group. I would like to thank Dave Ostrowski for powder days, his genuine friendship, sense of humor, and gue(o)rilla tactics on the mountain. Next I would like to thank several lab mates that have offered experimental advice and have been there to share stories and insight, and are absolutely wonderful people to work with: Ashley Marshall, Dan Kroupa, Jessica Ramirez, Joey Luther, Barbara Hughes, Matt Beard, Boris Chernomordik, Natalie Pace, Natalia Azarova, Greg Pach, Ryan Crisp, Nikos Kopidakis, Bryon Larson, Candy Mercado, Andrew Ferguson, Erin Sanehira,

Lance Wheeler, Nick Anderson, Obadiah Reid, Rachelle Ihly, Sungwoo Kim, Tyler Clikeman, Steve Christensen, Matt Bergren, Sanjini Nanayakkara, and Jeff Christians. I would like to thank several professors that had a profound impact on my education and helped me achieve much appreciated chemistry enlightenment on various topics: J. Mathias Weber, David Jonas, Joel Eaves, Steve George, Veronica Bierbaum, and Henry Kapteyn. I would like to thank several classmates in my cohort, as we banded together through what was arguably the best, yet most stressful times of our lives: Jessie Porterfield, Jaime DuMont, Laura Gonzalez Palacios, Sean Ryan, Amanda Grenell, Jasper Cook, Joel Clancey, and Brett Fiedler. Finally I would like to thank several other chemists for a great time along the way and for fruitful, lifelong friendships: Jon Travis, Chas Nichols, Casey Christopher, Phil Calabrese, and Daniel Higgs.

This research was funded by the US Department of Energy, Office of Basic Energy Sciences, Division of Chemical and Biosciences, under Contract DE-AC36-08GO28308 with NREL and DE-SC0007004 at CU-Boulder.

Contents

Tables

Figures

1. Introduction

1.1. Motivation

The pursuit of new and diverse clean energy production avenues continues to become increasingly vital as the global energy demand increases. The vast majority of global energy production, currently estimated to be over 13 terawatts annually, is generated by combustion of fossil fuels, and approximately 20 terawatts of carbon neutral energy generation needs to be generated by 2050 in order to avert catastrophic global environmental and economic disasters and consequences.[1] Representatives from almost 200 nations convened in Paris in the 2015 United Nations Climate Change Conference, COP 21, to address climate change and agreed to limit global temperature increases to less than 2° C above pre-industrial levels by transitioning to renewable, carbon neutral energy production and infrastructure and drastically reducing global greenhouse gas emissions, representing a major improvement to the outdated Kyoto Protocol of 1997.[2]The Paris Agreement supports the global paradigm that atmospheric warming and climate change are widely accepted and irrefutable. Although this was a step in the right direction, some would argue that this agreement does not go far enough.

An integrated web of renewable energy production (solar, wind, geothermal, tidal, hydroelectric, etc.) and storage (batteries, hydrogen fuel, biofuels, etc.) will be necessary in order to overcome geological resource limitations, transmission, and intermittency challenges to producing a reliable, steadfast supply of energy to meet global needs. The sun, estimated to have about 5 billion years of fuel left, outputs an astounding amount of energy, with more energy hitting the earth in just a few hours than the global demand in an entire year![3] Photovoltaic (PV) materials play an essential role in power generation, and consequently, efficiency becomes

paramount in the search for commercially viable solar cells. Overcoming fundamental limits to photovoltaic (PV) efficiency, first laid out by Shockley and Quiesser,[4] could lower barriers to utilization of solar power in a variety of practical scenarios.

Silicon has dominated the solar market for decades, as it is generally abundant, stable, non-toxic, and efficient. The initial cost of silicon is relatively high, though, as preparation and manufacturing costs are significant. Although the cost continues to decrease as production volume increases, purification and fabrication processes are optimized, and efficiency is improved, researchers are obliged to seek out other materials with efficiency, cost, longevity, and energetic considerations. Several other viable solar energy harvesting materials, such as CIGS, GaAs, dye-sensitized solar cells, organic photovoltaics, quantum dots, CdTe, CZTSSe, perovskites, etc., have been investigated, both fundamentally and in current-producing solar cells.[5]

The work presented here focuses on photophysical and structural investigation of organic materials that undergo singlet fission (SF), in an effort to assess quantum yields and lifetimes of excitons, stability, and solid-state morphology. While these studies are largely fundamental, the end-goal, although outside the scope of this dissertation, is to determine if these could be candidates utilized as components in a solar cell by considering a path to practical and commercial viability. Various spectroscopies and theoretical calculations were employed to characterize and evaluate a wide range of properties relevant to solar photochemical energy production.

1.2. Singlet Fission Overview, Origins, and Potential Applications

SF is a process in which a chromophore in an excited singlet state interacts with a nearby chromophore in its ground electronic state to yield two triplets, and is the molecular analogue of

multiple exciton generation observed in semiconductor nanocrystals.[6,7] A simplified graphic of SF is presented in Figure 1.1.[8]It was discovered in polyacene crystals decades ago[9-11] but has only recently been investigated in a wider variety of organic compounds.[8] In 1965, Singh and coworkers were studying the photophysics and excited state dynamics of anthracene crystals using laser induced excitations studying fluorescence decays. They noticed that two triplet excitons could be generated from a singlet excitation.[9] A few years later in 1969, two studies by Pope*et al.* and Merrifield *et al.* outlined efficient SF in crystalline tetracene, attributing SF as the dominant radiationless decay pathway, while also observing and presenting results on triplet-triplet annihilation (TTA), as well as addressing that the SF rates are magnetic field dependent.[10,12] More in depth and quantitative SF, TTA, and magnetic field affect tetracene studies were published in 1971 and 1975.[13,14]SF was discovered in spirilloxanthin, a carotenoid, in 1980 and in polydiacetylene (or poly(4BCMU), a conjugated polymer) in 1989.[15,16]These exciting and important initial studies helped set the stage for a now flourishing and exciting field of work.

The potential utility of SF for photovoltaics has been recognized[17] and lies in the generation of two electron-hole pairs per absorbed photon. When paired with red/near-infrared absorbing chromophores, green/blue absorbing SF chromophores can boost photocurrent in solar cells via triplet injection or energy transfer and raise the maximum theoretical power conversion efficiency of a single-junction solar cell from ~33% to ~45% (Figure 1.2), beyond the Shockley-Quiesser limit,[4,8,17-20] with the added potential of molecular and crystallographic control through chemical synthesis. A dye-sensitized solar consisting of a mix of a conventional, ~1eV bandgap sensitizer, as well as a ~2eV $S_0 \rightarrow S_1$ bandgap SF sensitizer producing ~1eV bandgap T_1 excitons could be prepared such that charges are collected onto TiO_2 in parallel. This could be

accomplished without the current matching constraints of other architectures. Figure 1.2 also presents optimal bandgap potentials for such a device. During SF an excited singlet exciton splits into two triplet excitons each with approximately half the energy, a process which could accentuate the performance of a lower bandgap semiconductor such as silicon by generating photocurrent rather than losing excess photon energy to heat. A higher bandgap SF absorber could be deposited directly onto a silicon solar cell in order to absorb high-energy photons more efficiently, thus, as previously stated prevent detrimental thermodynamic losses.

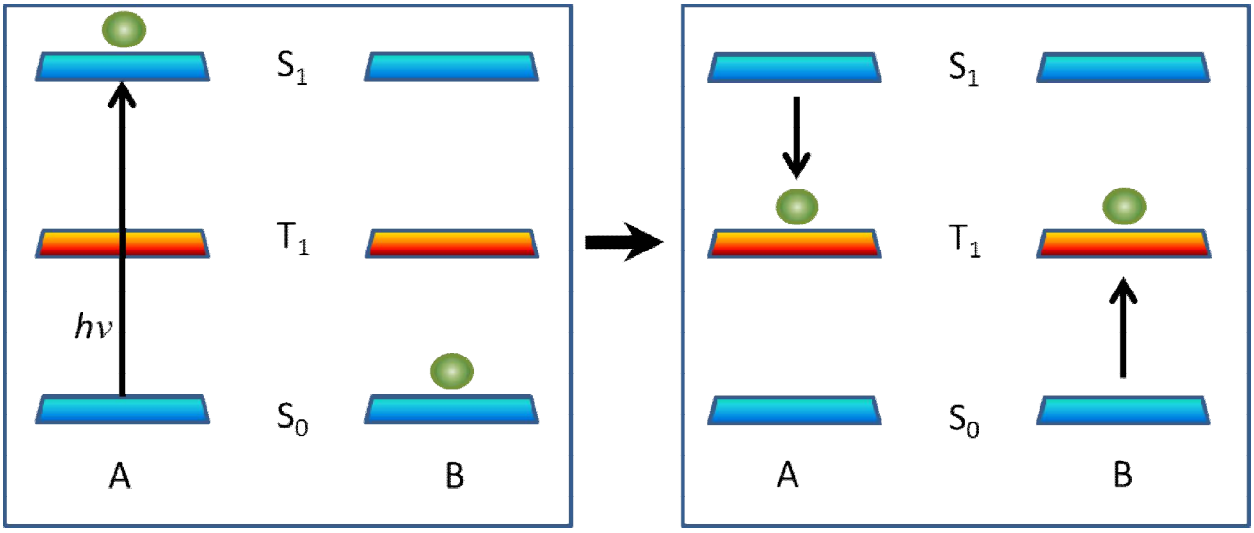

Figure 1.1

Simplified view of the net SF process, A and B represent individual chromophores.

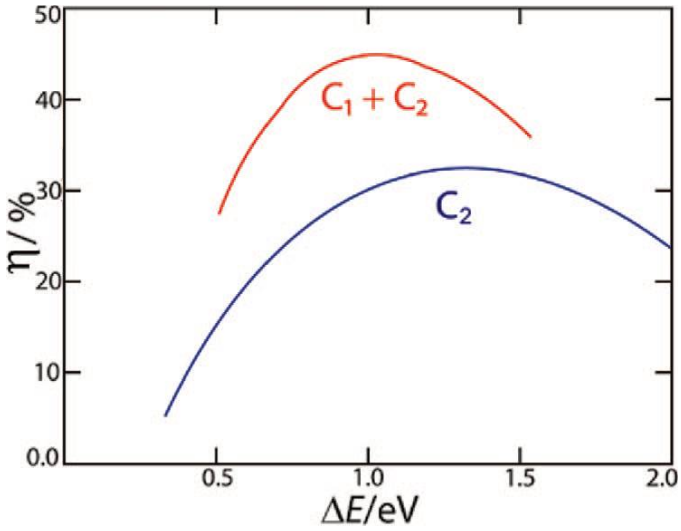

Figure 1.2

Theoretical maximum solar cell efficiencies of a standard dye-sensitized solar cell (blue) and a dye-sensitized solar cell with a SF chromophore and a conventional sensitizer (red) as a function of $S_0 \rightarrow T_1$ band gap. Reproduced from Reference 8.

1.3. Criteria and Mechanism

There are several practical requirements that must be met for the maximum increase in PV efficiency to be realized, but at present a lack of detailed scientific understanding of SF is the biggest obstacle to further progress. SF is a multichromophoric, spin-allowed process occurs through a correlated triplet ^{1}(TT) state, in which the spin functions of the two triplets are coupled to that of a pure singlet, and therefore does not violate selection rules. After the ^{1}(TT) state is formed, the triplets can undergo some dephasing process, either spin, electronic or other dephasing, to become two uncorrelated T_1 excitons. The overall process is summarized by Equation 1.1:

$$S_0 + S_1 \leftrightarrow {}^1(TT) \leftrightarrow T_1 + T_1 1 \qquad (1.1)$$

SF can occur via a few different mechanisms, either following a direct or charge transfer (CT) mediated pathway. These processes, spin states, and matrix elements are described in Figure 1.3.

The typically ultrafast direct mechanism is shown in blue, whereas the mediated process is shown in the upper and lower routes of the scheme by the purple arrows. The CT state energy must be close to that of the S_0S_1 in order for CT mediated SF to occur. In the mediated mechanism the CT state serves as a virtual state, and is not formally populated. Indirect SF can occur if the CT state is slightly lower than the S_1 state, whereupon the CT state is populated in an intermediate step before the correlated ^{1}(TT) is formed.

Prompt SF occurs if the singlet excitation resides on a site where the interchromophore alignment, coupling, and geometry favor SF. If the intermolecular alignment is not favorable to SF, the singlet exciton can migrate by hopping across adjacent molecules until it finds a location where two chromophores that are aligned optimally such that SF becomes highly favored. This is observed experimentally by, for instance, fluorescence decays having two decay time constants, corresponding to the prompt SF and for the SF resulting from the singlet migration. If SF occurs on ultrafast time scales, the singlet is likely delocalized over at least one molecule, whereas if SF occurs more slowly, the singlet can become localized within one area of the molecule. A detailed analysis of the mechanistic considerations can be found in recent reviews.[8,21] The two triplets combine in a coherent superposition of the nine sub-level wave functions to form the singlet wave function, the form of which is presented in Equation 1.2,[8]

$$\psi_k = \varphi_S C_s^k |S\rangle + \varphi_T \sum_{l=2}^{4} C_T^{k,l} |T^l\rangle + \varphi_Q \sum_{l=5}^{9} C_Q^{k,l} |Q^l\rangle \tag{1.2}$$

where the *C* coefficients are normalized to 1 for the singlet, 3 for the triplet, and 5 for the quintet. A detailed mathematical explanation of wave functions and matrix diagonalization can be found in the Smith and Michl review.[8]

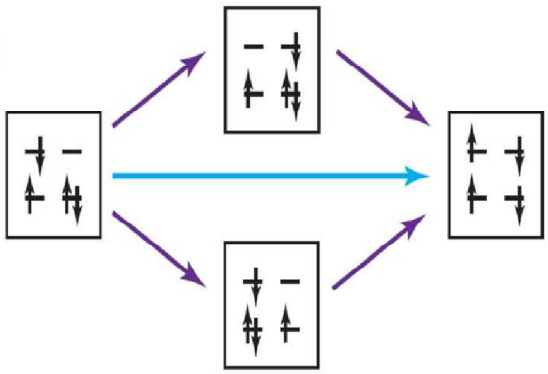

Figure 1.3

SF direct (red arrow) and CT mediated (cyan and blue arrows) mechanisms. Reproduced from Reference 21.

In order for SF to be efficient and not wasteful of potential energy, the first excited singlet state energy (E_{S1}) should be close to twice the energy of the lowest triplet state (E_{T1}). If E_{S1} is significantly less than $2\times E_{T1}$, SF can still occur to some degree, but it is likely to be thermally activated. In addition, chromophores need to be coupled strongly enough to be able to generate the coupled triplet pair ^{1}(TT)rapidly (typically ps or sub-ps) before other excited state processes occur (fluorescence, internal conversion, non-radiative decay, etc.), but weakly enough such that subsequently the triplet excitons can become independent.[22] Recent studies regarding the nature of the magnetic field dependent ^{1}(TT) state help build insight and understanding about how this state forms and how this state differs from an uncorrelated, dephased T_1 exciton originating from SF or from sensitization experiments.[23-25]

Electronic coupling, energetics, and mixing between singlet, charge transfer, and doubly excited states determine whether the SF mechanism is coherent or incoherent, or if it is a mediated or direct process.[26] These can be affected by molecular structure, such as changing the energetics by adding electron donating or withdrawing groups to the chromophore;[27] and can also be affected by the crystal structure, which can be influenced by substitution of side chains[28-

[31] or altering the film preparation conditions to access unique polymorphs.[32-34] In addition to these controlling properties, which may be thought of as intrinsic to the molecular and crystallographic structure, there may be extrinsic effects due to defects, impurities, interfaces, and differing dielectric environments. Whereas it has long been observed that crystallite size, and therefore grain boundaries, affects charge carrier mobilities and other semiconductor properties,[35,36] only recently has it been shown that crystallite size affects the rate of SF in polyacenes, specifically in polycrystalline films of tetracene (Tc).[37]

From the limited number of applications, it is clear that taking full advantage of SF requires a more complete understanding of the mechanism and a wider array of systems supporting efficient SF.

1.4. Recent Work

Only a few classes of molecules have demonstrated efficient SF, including carotenoids, perylene diimides, semiconducting polymers, and polyacenes, some demonstrating triplet quantum yields, arguably the most relevant performance based metric, close to 200% in crystalline solids and films.[26,28,38-62] Typically, highly conjugated, alternant hydrocarbon systems, like those listed above, and biradicals give rise to appropriate alignment of singlet and triplet energy levels, as ascribed above.[8] In the class of carotenoids, zeaxanthin has shown yields from 90-200%, and has proved to be a model chromophore.[60]Polyacenes and their derivatives (referenced above), such as tetracene, pentacene, hexacene, diphenyltetracene, TIPS-tetracene, TIPS-pentacene, and tetracene dimers, have been investigated and shown to exhibit varying performance, most showing triplet yields over 100%. A vast number of functionalized acenes has been identified and photophysics have been considered by Anthony, and thus the exploration of this molecular space is extraordinary.[63]Conjugated polymers, such as methyl-substituted

ladder-type poly(*p*-phenylene), poly(*p*-phenylene vinylene), polythiophene, and poly(diethyl dipropargylmalonate), show give extremely low yields, less than 1%, and are known to have extremely high, >1eV, activation energies.[64]

Thin films are optimal in that the appropriate optical density that would be practical in a solar cell can be achieved, and in addition thin film crystallites can give rise to molecular packings that are suitable for the intermolecular coupling necessary for efficient SF. It has been predicted and observed that slip-stack alignment of nearest neighbor pairs is optimal for SF with high yields.[8,65] Covalently linked dimers, in some cases, exhibit low yields due to various competing processes associated with the molecules being bonded and because of their close proximity, in addition to geometric arrangements unfavorable to SF.[66] For instance, singlet-singlet annihilation followed by ultrafast internal conversion or TTA can lower triplet yields significantly. It is also not trivial to engineer a dimer where the two chromophores will stack in a slip-stacked arrangement optimal for efficient SF. Finally, a dimer system can significantly lower the S_1 state compared to that of the monomer, such that the SF manifold is energetically inaccessible.[8]

Although crystallinity typically facilitates efficient SF, high triplet yields have also been observed in amorphous diphenyltetracene films.[43] Various devices designed to leverage SF, utilizing tetracene and pentacene, have been produced thus far; however, with working device efficiencies at less than a few percent, a deeper understanding of the process will inevitably facilitate a more expedient approach to practical utility.[35-37,49-53]Recent theoretical investigations have produced exciting advancements in understanding of SF, especially with regard to structural, energetic, and mechanistic criteria.[34,65,67-74] Structural modifications to core and substituent groups can substantially alter molecular packing in crystalline thin films, tuning

intermolecular coupling and orientations suitable for efficient triplet exciton generation, while largely maintaining energy level requirements.[28,29,31,39,40,75-77] Thin film (TF) morphology substantially influences triplet yields, as some polymorphs, obtained by various deposition and annealing techniques, give rise to fast competing pathways, such as internal conversion or excimer formation.[32-34,57,78] Moreover, crystallite size, defects, and interfaces can affect triplet yields and SF rates.[37,78,79]

1.4.1. 1,3-Diphenylisobenzofuran

This dissertation will cover studies of three SF chromophore systems, all of which show polymorphism in TFs. 1,3-Diphenylisobenzofuran (**1**) has biradical character and has been shown to have two polymorphs that have drastically different triplet yields. While one polymorph has been shown to display near unity SF yields, the other, more stable polymorph suffers from excimer formation and exhibits very low triplet yields. This is an intriguing system, because its polymorphs are quite similar, but the subtle disparities in structure give rise to considerably different photophysics. In addition to investigating structural differences between the two polymorphs, steady state and time-resolved studies have helped reveal the mechanism of SF and other dynamics.

1.4.2. Tetracene

While a considerable amount of work has been conducted on **1**, a relatively new system, over the past few years, exciting results from systems that have been examined for decades continue to emerge. Tc is known to have multiple polymorphs, and although many groups study this chromophore, morphology is rarely discussed or considered. While there have been reports of crystallite size affecting dynamics,[37] a thorough examination and comparison of structural, electronic, and dynamic properties of the two known Tc polymorphs has not been pursued until

now. The Tc chapter presented here looks at photophysical differences between the two polymorphs in addition to considering effects of crystallite size. One polymorph undergoes SF more rapidly than the other and crystallite size does not appear to have any impact on the SF kinetics, whereas the other polymorph exhibits longer SF time constants and the size of crystallites affects rate constants significantly. It is important to learn everything possible about a system, and studies on Tc and its derivatives will undoubtedly continue, but it also vital to explore new materials.

1.4.3. Indigo Derivatives

Cibalackrot (**2**), a robust indigo derivative and highly conjugated biradicaloid, has been predicted to have appropriate singlet and triplet energy level spacings. In addition to demonstrating high fluorescence yields in solution, long fluorescence lifetimes, and excellent charge transfer characteristics, **2** also has multiple bulk and TF polymorphs. Analogous to **1**, the less stable polymorph of **2** shows much higher triplet yields than the thermodynamically stable polymorph of **2**, albeit the efficiency of SF is much higher in **1** than in **2**. A tert-butylated derivative of **2** was also investigated, although triplet yields of the derivative are even lower. Nonetheless, in the final main chapter of this dissertation, **2** and the derivatized counterpart are structurally and photophysically characterized by similar means as the other aforementioned systems. Despite low SF yields, valuable insight was gained from this investigation. The systems presented here, along with their relative S_1 and $2\times T_1$ energy levels are pictured in Figure 1.4, along with the band gaps for the theoretical maximum efficiency bandgap region.

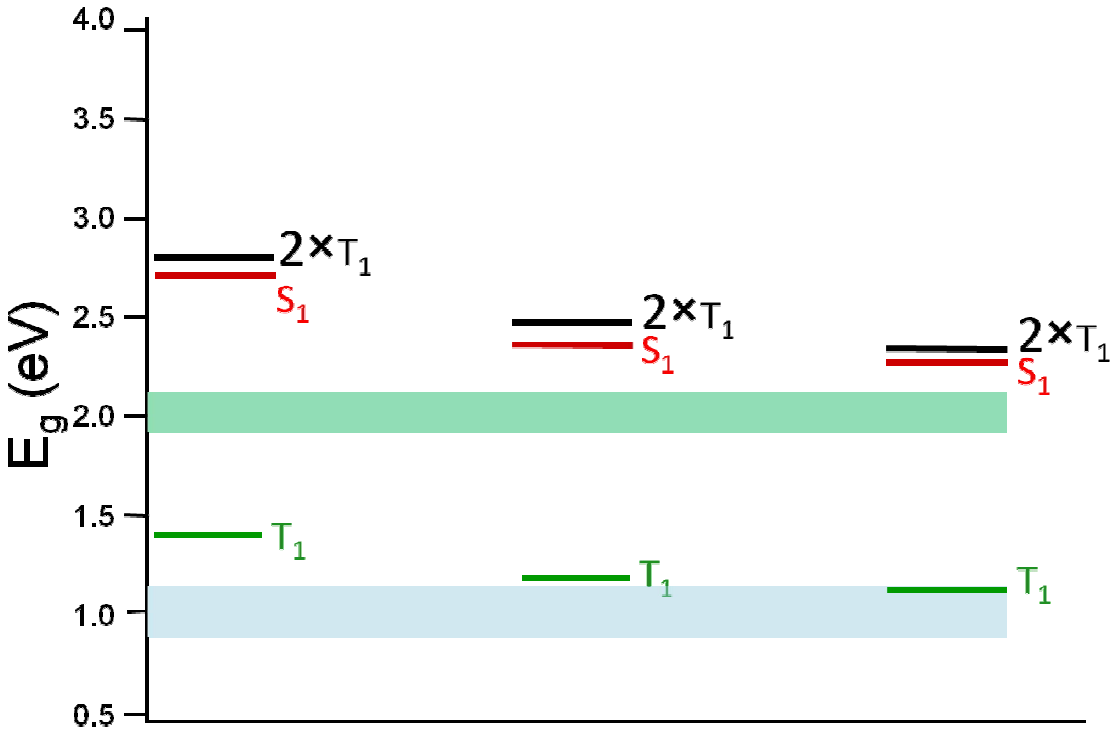

Figure 1.4

Molecules presented below, along with their S_1, T_1, and $2\times T_1$ bandgap energies. The green and blue bars highlight the optimal S_1 and T_1 bandgap energies necessary for maximum theoretical solar cell efficiency in a multichromophore device.

2. Experimental Methods

The methods presented in this chapter are generally those used throughout the various studies presented below. Any modifications to these methods and setups are noted within each subsequent chapter, where relevant.

2.1. X-ray Diffraction

Powder X-ray diffraction (XRD) analysis of TFs was performed on a Rigaku D/Max 2500 diffractometer. An alignment procedure was performed on substrate blanks to optimize signal intensity and calibration before sample data collection. Typical scan rates were 1˚/min scanning from 5–50˚ using CuKα radiation (λ = 1.54Å) in order to generate intensity (counts per second) as a function of 2θ diffraction angle.

2.2. Atomic Force Microscopy (AFM)

AFM was performed on a Park Systems XE-70 AFM using a Tap 300-G AFM tip. Sample areas scanned were 30, 10, and 5 μm^2, with a resolution of 512 × 512 pixels at 0.2 Hz line scan rate.

2.3. Thin Film Preparation

TFs were deposited by thermal evaporation of the material in powder form onto heated, cooled, or room temperature substrates (80 – 475 K). Depositions were performed at pressures of about 1×10^{-6} Torr in an Angstrom Engineering Nexdep thermal evaporator using a RADAK I evaporation source. The evaporator is coupled to a glovebox under nitrogen atmosphere, enabling samples to be deposited and sealed under inert conditions, thus preventing exposure to oxygen and water vapor. About 50 mg of material was placed in an alumina crucible, and vaporization was induced by resistively heating a tungsten filament. The total deposition

thickness was monitored by an Inficon quartz crystal microbalance operating around 60 MHz, and the substrate stage, about 18 inches away from the source, was rotated at 30 rpm in order to generate high quality, reproducible TFs. Typical deposition rates were 0.1 – 10 Å/s, and film thickness varied from 2 to 200 nm. Annealing of TFs was performed in air at room temperature, or it was expedited by placing a sample on a hot plate at elevated temperatures under inert atmosphere for 10–60 min, depending on film thickness and degree of annealing desired.

Prior to time resolved measurements, films were sealed with a matching glass cover slip by placing a Surlyn (60 μm thick) frame outlining the film to be analyzed between the two cover slips. In a glovebox under inert atmosphere, this sandwich configuration was placed on a hot plate at 95°C for approximately 15 seconds to melt the Surlyn and pressed to seal. This prevents film photobleaching and oxygen quenching of triplet excitons, essential to probing the true SF dynamics.

2.4. UV-Vis Absorption and Extinction Measurements

Optical extinction spectra were collected using a Varian Cary 500 UV-Vis-NIR spectrophotometer with a scan speed of 600nm/min and a scan range of 200– 1200nm. The baseline was collected in dual-beam mode with blank substrates in the front and rear beam paths. Sample data were referenced against a blank substrate in the rear beam path. Variable temperature (VT) absorption measurements were performed by placing samples in an Oxford Instruments Optistat DN cryostat. The cryostat was then positioned in a Hewlett-Packard HP8453 UV-Vis Spectrophotometer, and extinction spectra were taken over a range of temperatures from 76 to 293 K. No accounting for scattering or reflection was made with this instrument. Absorption measurements employing an integrating sphere (IS) are a more accurate representation of the true absorbance of these films than extinction measurements due to the

sequential measurement of transmittance (*T*) and reflectance/scattering (*R*). A Shimadzu UV-3600 UV-Vis-NIR spectrophotometer and an Agilent Cary 6000 UV-vis-NIR spectrophotometer were used to determine optical density (OD) of the films from OD = –log(*R* + *T*).

2.5. Steady-State Fluorescence and Fluorescence Quantum Yield

Fluorescence measurements of TFs of **1**were performed on a Horiba Yvon Model FL-1039/40 Fluorolog, a Horiba JobinYvon iHR320 monochromator, and a Horiba Jobin Yvon SPEX Instruments S.A. Group Spectrum One G35 CCD camera. The excitation wavelength for measurements ranged from 400 to 550nm, with a detection range of 300 to 1000 nm. VT uncorrected absorption and VT fluorescence measurements were performed by placing samples in a cryostat and cooling from room temperature to 76 K. A Lab Sphere integrating sphere was used in conjunction with the fluorimeter in order to obtain fluorescence quantum yields, Φ_F, at room temperature. Peak areas of both excitation and emission spectra were integrated and Φ_F was calculated using the expression: $\Phi_F = \left(\int Em_{\text{sample}} / \left(\int Ex_{\text{blank}} - \int Ex_{\text{sample}}\right)\right) d\tilde{\nu} . \int Em_{\text{sample}} d\tilde{\nu}$is the integrated area of the emission spectrum, $\int Ex_{\text{blank}}\, d\tilde{\nu}$is the integrated area of the excitation peak for the blank, and$\int Ex_{\text{sample}}\, d\tilde{\nu}$ is the integrated area of the excitation peak with the sample in place.

2.6. Time-Resolved Fluorescence Spectroscopy

Time-resolved fluorescence measurements were performed using a supercontinuum fiber laser (Fianium, SC-450-PP) operating at 1 – 10 MHz as the excitation source. Various excitation wavelengths were utilized. Time correlated single photon counting methods were employed to measure fluorescence decays at various emission wavelengths with an instrument response function incorporated into the fitting. Fluorescence decays at various emission wavelengths from

460 nm to 800 nm were fitted using a multiexponential function convoluted with an instrument response function, which was measured by scattering the excitation beam through a Ludox solution (40 wt. % colloidal silica suspension in water).

2.7. Ultrafast Transient Absorption Spectroscopy

Transient absorption measurements were performed on an Ultrafast Systems Helios/Eos setup as outlined in previous work.[57,78] In summary, a Coherent Libra regeneratively amplified Ti:sapphire laser generated laser pulses with 100 fs pulse width, a frequency of 1 kHz, and a power of 4 W at 800 nm. About 30% of this beam was picked off and directed into a TOPAS-C optical parametric amplifier in order to produce pump wavelengths of 300 – 600 nm. About 100μJ of the 800 nm beam entered the Helios/EOS and passed through a continuously moving CaF_2 crystal or a stationary sapphire crystal in order to generate a white light continuum probe (330 – 850 nm). This probe was split into two beams, one that passed through the sample to measure the excited state absorption and one that was directed into the detector as a reference. The pump, with a spot size of about 250 μm diameter, and probe beams were overlapped at the sample, and spectra were recorded at various pump-probe time delays dictated by the delay stage, which changes the path length of the probe. After passing through an optical chopper (500 Hz), the probe and reference were focused into fiber optic light guides and measured by matched photodiode arrays. Scans spanned time delays from Δt = 0 – 400 μs, depending on the kinetics of the system. The scans were usually acquired in a bidirectional manner, scanning in increasing time delay and then decreasing time delay to ensure that these spectral and kinetic scans matched in both directions, verifying that the samples were not photodegrading over time. The Helios/Eos software was used to collect and calculate the transient signal, and the Surface Explorer software enabled for background, chirp, time-zero corrections, and singular value

decomposition (SVD). In general, low fluence excitation was used to avoid singlet-singlet annihilation, multi-photon absorption, and other effects that result from using high fluence excitation.[52]

VT measurements were performed either using an Oxford Systems Optistat DN cryostat capable of achieving temperatures within a range of 77 – 500 K, or a Janis cryostat controlled by a Lakeshore Cryotronics Model 325 Temperature Controller with a temperature range of 77 – 325 K. TF fluorescence and transient absorption spectra were collected at various temperatures. The elevated temperature (295 – 500 K) transient absorption was performed on highly annealed films to maintain morphology, as heating can induce undesirable morphological changes.

3. Two Thin Film Polymorphs of the Singlet Fission Compound 1,3-Diphenylisobenzofuran

3.1. Background

1,3-Diphenylisobenzofuran (**1**) was identified in earlier theoretical work as a candidate that fulfills the optimal energy requirements for efficient SF.[62] We subsequently characterized the properties of isolated monomers[80] and measured a 200% quantum yield of SF in polycrystalline TFs at 77 K.[56] Weakly coupled and linearly linked covalent dimers of **1** exhibited only a small triplet yield in solution,[81] probably due to a suboptimal inter-chromophore geometry for SF.[8] Crystals of **1** contain slip-stacked columns of molecules, a geometry identified as favorable for fast SF, whether the mechanism is primarily via direct or mediated coupling.[21] Most other observations of efficient SF have also been in molecular crystals or TFs, and polycrystalline films of pentacene have been recently shown to exhibit fast triplet formation kinetics[51,82-84] and greater than 100% external quantum efficiency in a photovoltaic device.[85]

In the previous work on TFs of **1**, we reported several observations that could not be explained without further investigation: (i) a morphology-dependent triplet yield; (ii) a non-monotonic temperature-dependent triplet yield; and (iii) biexponential triplet formation kinetics. In addition to addressing issues (ii) and (iii),[57] we present here an investigation of two polymorphs of **1** and their basic photophysical properties that most likely lead to observation (i). Until very recently, the only report in which different crystal morphology of a chromophore affected SF concerned perylene.[86] α-Perylene and β-perylene are two crystalline polymorphs, the former of which is known to readily form excimers. It was suggested that excimer formation in α-perylene impedes SF, dominating the photophysics unless at least 3500 cm^{-1} of excess energy is provided. In Tc, the most commonly studied SF compound, phase transitions are known to

affect emission spectra as a function of temperature,[87] but the influence of the variation in inter-chromophore coupling during the phase change on SF has not been reported. In the case of diphenyltetracene,[88] films have been fabricated that have heterogeneity inferred from their amorphous nature. The inter-chromophore interactions are essentially divided into SF-active (triplet formation time less than 50 ps) and SF-inactive (triplet formation time greater than 0.5 ns), suggesting that only a select set of molecular pairs produces the fast SF rate and that excitations produced at suboptimal sites must undergo diffusion before SF can occur.

A recent example of morphology dependent SF is diphenylhexatriene, which exists in both monoclinic and orthorhombic forms.[89] In that case, both the formation of the triplet pair from the initially excited singlet (k_{-2}) and the separation of the singlet-coupled triplet pair (k_{-1}) depend on the unique intermolecular geometries found in the two polymorphs. In many instances multiple phases or polymorphs of a particular organic compound exist in both bulk and TF form, resulting in unique intermolecular geometries and absorption spectra.[90,91] If a pure phase cannot be obtained or if a phase change occurs by varying temperature or pressure, the resulting photophysics are likely to be influenced. Subtle changes in inter-chromophore geometry or S_1/T_1 energy level alignment could have a large effect on SF. Solid **1** appears to be a suitable system for investigating such effects.

In this chapter we elucidate the structural and photophysical characteristics of films of **1**, which naturally contain a mixture of two different polymorphs,α and β, the structures of which we have identified by comparison with bulk crystals. We control the composition of the film by choice of deposition conditions and subsequent thermal annealing and measure a variety of spectroscopic observables. We find a ~600 cm^{-1}red shift in the onset of S_1 absorption for theβ-polymorph, which provides a clue toward rationalizing the lower triplet yields and higher

fluorescence yield in β–**1** films. Although coupling between molecules in a slip-stacked configuration has been previously shown to be important for SF, interactions between molecules in adjacent stacks may play a large role in processes that compete with SF, and their significance should not be underestimated.

In order to investigate the mechanism of SF in TFs of **1**, we have performed ultrafast transient absorption spectroscopy as a function of sample temperature and excitation fluence on polycrystalline TFs composed of two polymorphs. Our earlier investigations revealed that films enriched in a particular polymorph of **1** displayed near 200% efficiency for triplet formation at 77 K, while films composed primarily of a second polymorph had a very low triplet quantum yield. Data confirm the triplet yield disparities in the two polymorphs and demonstrate the distinct fates of the initially prepared singlets in films of different structure. SF is inhibited in the more stable polymorph due to rapid excimer formation and trapping. The less stable polymorph undergoes highly efficient SF with a dominant time constant of 10-30 ps and without strong thermal activation. Transient absorption measurements with varying excitation fluence indicate that singlet-singlet annihilation is a primary competitor of SF at higher fluence, and that fission from higher-lying states can also contribute to the triplet formation process. Measurements employing different excitation energies and sample temperatures reveal the role that trapping processes play in attenuating the triplet quantum yield to produce the complex temperature dependence of the SF yield. The rate constants for SF itself are essentially temperature independent.

3.2. Experimental

3.2.1. Materials

Reagent grade acetone, anhydrous acetonitrile, anhydrous chloroform, anhydrous cyclohexane, anhydrous and reagent grade hexane, and anhydrous toluene were all purchased from Aldrich and used without further purification. All solvents were degassed by flushing with argon before use. Fused silica, sapphire, glass, quartz, and indium-doped tin oxide conducting glass (ITO) were rinsed with acetone and isopropyl alcohol and treated with an O_2 plasma. Powdered **1** (97%) was obtained from Aldrich.

3.2.2. Single Crystal Growth

Bulk crystals were grown by making nearly saturated solutions of **1** in various solvents, filtering through a Pall Life Sciences Acrodisc CR 13 mm syringe filter with a 0.2μmPTFE membrane, and slowly evaporating the solvent in a nitrogen environment. Considerable morphological control was achieved by employing various solvents and evaporation rates. Solvent evaporation times ranged from 1 to 10 days, depending on the vapor pressure of the solvent used. Vapor diffusion was another method utilized for crystal growth, wherein a nearly saturated filtered solution of **1** in cyclohexane was placed in proximity to a poor solvent, ethyl ether, in a dark, inert, enclosed atmosphere. A small amount of ether diffused into the saturated solution and slowly precipitated out large crystallites of **1**, suitable for X-ray analysis.

3.2.3. X-Ray Diffraction (Single Crystal and Powder XRD)

Crystals were attached to a loop (Hampton Research) with Paratone-N, cooled, and kept in a temperature-controlled stream of dry nitrogen gas during data collection. The temperature of the samples was controlled with Cryosystream Plus (Cobra) low-temperature system from

Oxford Cryosystems. The data for forms α and β of **1** were collected[92] on a Bruker APEX DUO diffractometer with Mo*K*α radiation (λ = 0.71069 Å) with a CCD area detector. Frames of 0.5° width were collected by φ and ω scans with exposure time of 10 s/frame (form β) and 20 s/frame (form α). To ascertain that there are no phase transitions, the data collection was performed at both room (298 K) and at low (100 K) temperature for both crystals. The data were merged and integrated with the SAINT software.[93] The multi-scan method was used for absorption correction with SADABS.[94] The structures were solved by direct methods using the program SHELXS-97[95,96] and refined with SHEXL-97.[97] The coordinates and the anisotropic thermal displacement parameters for all non-hydrogen atoms were refined on *F*.[93] The hydrogen atoms were calculated using fixed distances. The data for the oxidized open-ring product were collected on a Bruker[98] APEX2 diffractometer (Bruker AXS) by using MoKα radiation (λ = 0.71069 Å) monochromated with a confocal multilayer X-ray mirror, a CCD as the area detector, and a rotating anode as X-ray source. The data were collected up to 2θ = 46.98° at room temperature, with frames width of 0.5° by ω scans with exposure time of 10 s/frame. The data were merged and integrated with SAINT[93] and corrected empirically with SADABS.[94] The structure was solved by direct methods with either SIR92[99] or SHELXS-97[95,100] and refined with SHEXL-97.[95,97] All non-hydrogen atoms were refined anisotropically. The hydrogen atoms were fixed as riding bodies. Selected crystallographic data are summarized in Table 3.1. These diffraction data were used to predict powder patterns of the bulk material (Mercury 3.0 Build RC5). Bulk crystal structure determinations were performed by Pance Naumov and Subash Sahoo.

3.2.4. Thin Film Preparation

TFs of **1** were deposited at room temperature by thermal evaporation of the powder onto substrates as described above. Solution dropcasting was also used to produce TFs. About 50 mg of **1** powder was placed in a vial with 10mL of a 1:1 chloroform:toluene mixture to create a roughly 20 mM nearly saturated solution. A 10–100 μL aliquot of this solution was dropped on the substrate and allowed to spread, generating nice continuous, optically transparent α-**1** films. The drying process was accelerated by placing the substrate in a stream of dry nitrogen, which helped to produce more continuous and homogeneous TFs. By mixing chloroform and toluene at ratios other than 1:1,the drop-casting process enabled preparation of films with enriched β character.

Annealing of crystallites from α- to β-**1**was performed by placing a sample on a hot plate at 90°C under inert atmosphere for 10–60 min, depending on film thickness. Considerable control of α:β composition can be achieved based on annealing time and temperature. Films that were predominantly of form α were often annealed in a few steps in order to produce predominantly form β. Spectroscopy was performed along this composition gradient to elucidate observable differences between the two polymorphs.

3.2.5. Calculations

Excitonic coupling (Davydov splitting) between molecules within the unit cells of the two known crystal structures of **1** at room temperature was calculated using the intermolecular geometries derived from the crystal structures and the electron repulsion integrals from the computed transition densities of **1**.[80] The diagonal elements (shift of the center of the Davydov doublet) were not calculated. SF matrix elements were calculated in the HOMO–LUMO approximation.[8] The mediated contribution was evaluated under the assumption that the charge-

transfer states are 25 kcal/mol above the initial and final states. All the calculations were performed using the 6-31G basis set.[101] The SCF molecular orbital coefficients and the repulsion integrals were evaluated using the PSI3 program.[102] The SF matrix elements and the Davydov splitting were calculated with a customized code ("SFMat"). All of these calculations were performed by the Michl Groups in Boulder and Prague (Michl and Havlas).

3.3. Results

3.3.1. Bulk Crystal Growth and Determination

Screening for polymorphs of **1** was done by slow evaporation from a variety of solvents in the dark under inert atmosphere. In ethyl acetate solution the compound was unstable, and crystals of the open-ring (oxidized) product were obtained, as confirmed with XRD analysis. Efflorescent yellow prisms (form β) were obtained from dichloromethane solution and by diffusion of diethyl ether vapors into cyclohexane solution. Slow evaporation of acetonitrile solution afforded orange-yellow blocks (form α). Photographs of these crystals are shown in Figure 3.1, and the structural parameters of the unit cells are presented below. When protected from light, all crystals were stable at room temperature. One of the structures closely matches that previously reported with a *P*2/c space group.[80]

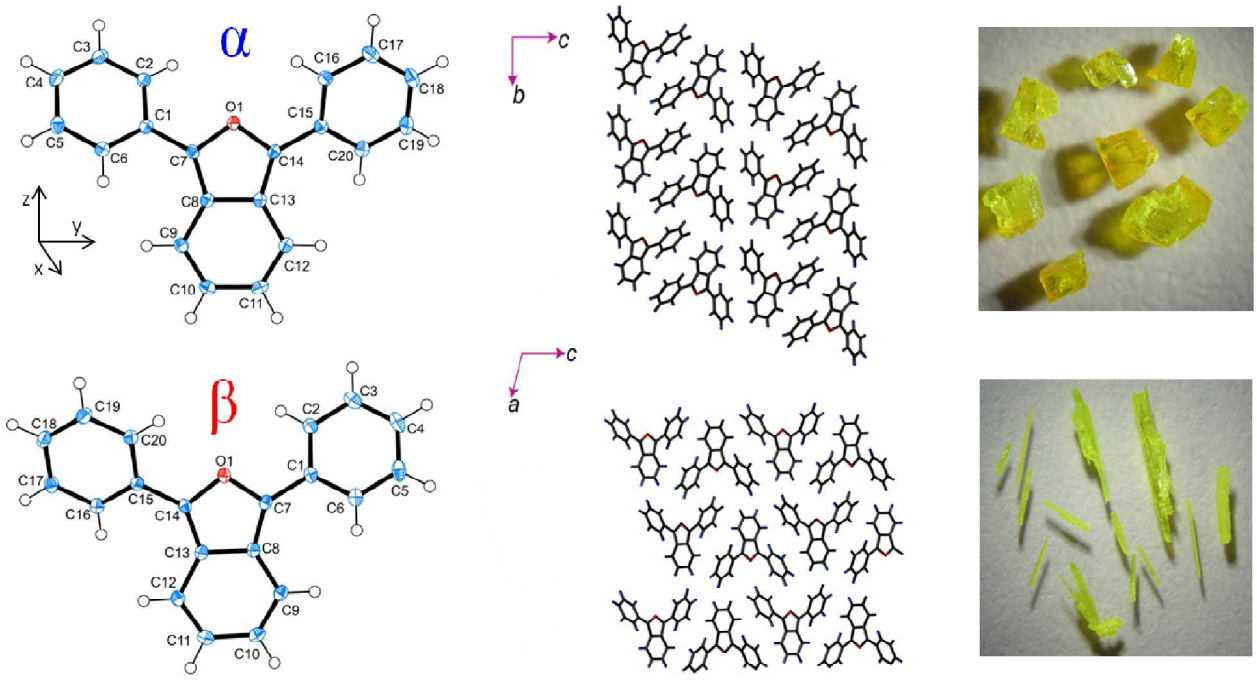

Figure 3.1
(Left to right): Molecular structures, long-range packing, and photographs of α-**1** (top) and β-**1** (bottom).

All molecules adopt a conformation with C_2 symmetry (phenyl groups twisted in a disrotatory fashion), with the difference in dihedral angles of the phenyl rings less than 0.9°. The dihedral angles of polymorph α were 22.895° and 23.208° and those of polymorph β were 22.718° and 23.589°.

Small differences exist between the lattice parameters of the two morphologies (Table 3.1, Figures3.1,3.2). The lengths of the *c* axis of the unit cells of α-**1** and β-**1** are 20.271 and 19.423Å, respectively. The angle β of the unit cell for form α and form β is 106.215˚ and 93.534˚, respectively. The differences in *c* and β directly affect the (002) interplanar spacing. In both forms, the *z* axis of **1** is perpendicular to the *ab* plane of the crystal; however, only in the α form is the *z* axis parallel to the *c* axis. This difference results in a unique tiling in the *b*-*c* or *a*-*c*

plane shown in Figure 3.1. Translationally equivalent molecules form infinite chains along the *b*-axis for α-**1**, resulting in the isobenzofuran cores of **1** being nearly perpendicular to those of molecules in all adjacent stacks. The closest co-planar inter-stack distance is 11.96 Å (measured between O atoms). For β-**1**, the chains in the *a*-*c* plane are disrupted after each pair of molecules, resulting in pairs of molecules that have co-planar isobenzofuran cores at a separation of 6.67 Å.

The average π-stacking distance is 3.444 Å for blocks(α) vs. 3.436 Å for rods (β), differing by only about 0.01 Å. The intermolecular distance is 5.590Å for blocks and 5.584Å for rods (it occurs in the same relative direction for both forms).The slip distance along the long axis of the molecule, D_L, and short axis, D_S for α-**1** is 4.78 and 0.1 Å, where those distances for β-**1**are about 4.78 and ~0 Å. Upon cooling from room temperature to 100 K, the unit cell of each form contracts by about 3%, or about 45 $Å^3$. Although the slip distances and orientations are very similar, they are nonetheless included for completeness in Figure 3.2. The crystal does retain its space group, however, and no obvious phase change occurs within the temperature range of 100 to 298 K.

Table 3.1

Crystallographic parameters at 100 K and room temperature for single crystals of both form α and form β, and comparison with TF diffraction peaks at room temperature.

	Form α		Form β	
Habit	Block		prism	
T / K	298	100	298	100
Color	orange-yellow	orange-yellow	yellow	yellow
Crystal system, Space group	monoclinic, P2/c	monoclinic, P2/c	monoclinic, $P2_1/c$	monoclinic, $P2_1/c$
a / Å	12.998(5)	12.845(2)	5.584(4)	5.5584(8)
b / Å	5.590(2)	5.5390(10)	12.995(8)	12.8474(19)
c / Å	20.271(8)	20.027(3)	19.423(12)	19.100(3)
β/ °	106.215(9)	106.533(7)	93.534(15)	92.815(5)
V / $Å^3$	1414.2(10)	1366.0(4)	1406.9(15)	1362.3(3)
Z	4	4	4	4
ρ(g cm^{-3})	1.270	1.324	1.276	1.318
(002) predicted/ TF angle	9.08/9.06	9.20	9.12/9.12	9.27
(004) predicted/ TF angle	18.22/18.20	18.47	18.28/18.28	18.59

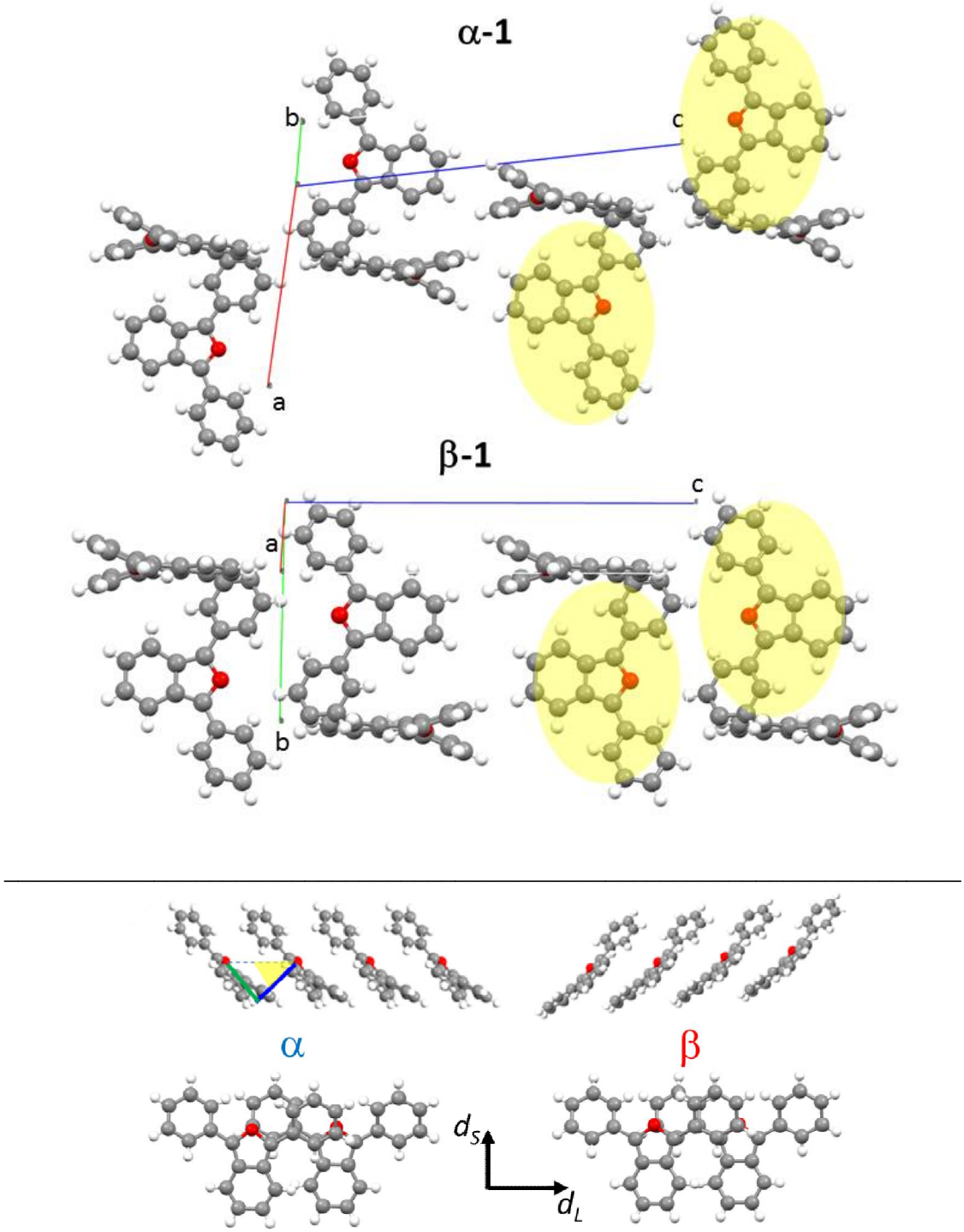

Figure 3.2

Top: slice of molecular stacks viewed perpendicular to π-stacking directions for form α and form β crystals of **1**. Nearest non-orthogonal molecules in adjacent stacks are highlighted, note yellow ellipses highlighting major differences in long-range crystal packing. Bottom: slippage views also presented.

3.3.2. Film Preparation and Characterization

The morphology of TFs prepared by thermal evaporation depends strongly on thickness and to some extent on the substrate. Films thinner than ~40 nm exhibit properties of predominantly β-form crystallites, regardless of substrate. As growth proceeds, a mixture of α and β crystallites results, and by a certain thickness, the films become predominantly form α. This threshold thickness, l_{th}, was about 125nm for films deposited on glass, fused silica, quartz, and sapphire, and about 70nm for films deposited on ITO.

The crystallinity of the TFs was determined by XRD. Typical diffraction patterns of the two film polymorphs are shown in Figure 3.3. The patterns are sparse, indicative of highly textured films, with the dominant peak, previously assigned to a reflection from the (002) plane, at about 9.08º for α-**1** and 9.12º for β-**1** films. These diffraction angles correspond to (002) interplanar spacings of 4.88 Å and 4.86Å, respectively. The peaks have widths of about 0.1˚, varying little between films of different composition.

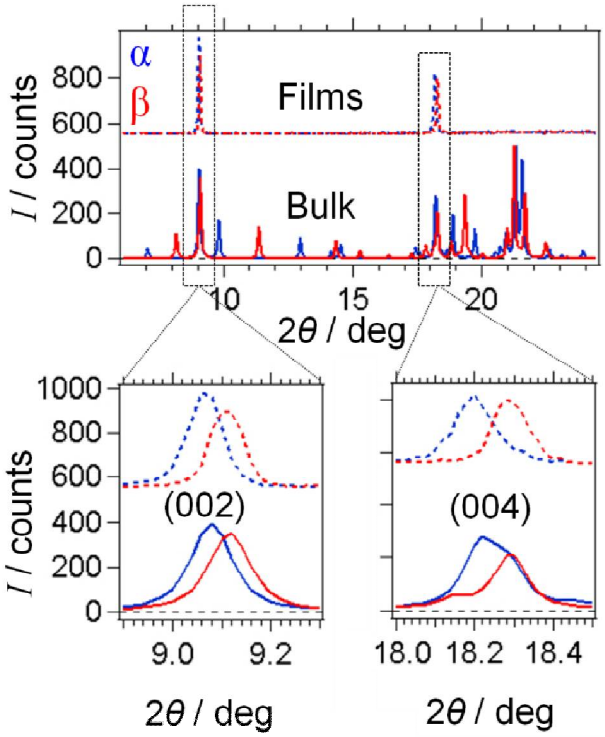

Figure 3.3

XRD of thermally evaporated films of **1** compared to bulk. Films show a high degree of crystalline texture about the (002) reflection plane. Bulk α (blue) and bulk β (red) calculated powder diffraction patterns (solid lines)from the single crystal XRD, compared to the measured TF (002) and (004) peaks (dashed lines).

A relatively fast deposition rate (~1 nm/sec) minimizes l_{th}, whereas slower rates yield films with higher β:α composition ratios. As the deposition chamber pressure is lowered below ~1 × 10^{-6} Torr, a significant amount of **1**sublimes from the substrates during the deposition, necessitating even faster deposition rates to prepare a thick film. TFs were also deposited on substrates cooled to 90 K, which did not have a significant effect on film morphology. Cold substrates did serve to reduce the amount of **1**lost by sublimation after deposition, thus enabling the substrate to retain more material while under vacuum. The effect of polarity of the substrate surface was investigated using a series of organosilane treatments, but regardless of whether a hydrophilic or hydrophobic surface was prepared, films tended to be highly scattering with broad

absorption features. Variations in crystallite size, shape, and orientation likely affected the reflectivity and scattering of the films, but there was no clear change in the α:β ratio. Substrate surface roughness may have some effect on these parameters (ITO tends to exhibit higher roughness factors), but was not tested systematically.

A solvent mixture of 1:1 chloroform:toluene proved to be the most effective at generating solution-dropcast films that were predominantly of α form. Overall, the dropcast films are less uniform than vapor deposited films, so the comprehensive spectroscopic studies were performed on vapor-deposited films, although most measurements were performed at least once on films made by both methods. Except where noted, all trends reported for vapor-deposited films were the same for dropcast films. Under ambient laboratory conditions, the α polymorph readily converts to the β polymorph over the course of days, suggesting that the β polymorph is more thermodynamically stable. At temperatures below 0°C the films retain their α:β composition ratio indefinitely. Preservation of film crystallite composition is also significantly enhanced by sealing the substrate under atmosphere. Solvent annealing was also carried out on these films. Films convert from α to β morphology after being exposed to methanol and toluene solvent vapors for just a few hours. The annealed films become highly scattering and inhomogeneous after a 24 h period.

The UV-vis absorption spectrum can be used as an expeditious means of identifying crystallite composition in films of **1** (*vide infra*). Figure 3.4a shows extinction spectra for a series of films of varying thickness deposited on ITO. Presented in Figure 3.4b are extinction spectra of TFs of similar thickness deposited on various substrates. A detailed analysis of the absorption spectra can be found below.

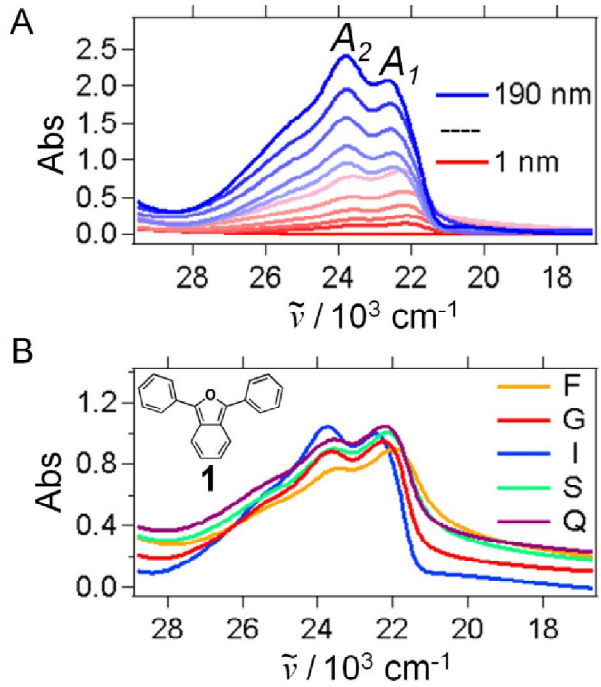

Figure 3.4

(a)Extinction spectra for films of **1** of varying thickness deposited on ITO. The two peaks most relevant to further analysis are identified as A_1 and A_2. (b) Extinction spectra for films of **1** of similar thickness on various substrates (F = fused silica, G = glass, I = ITO, S = sapphire, Q = quartz).

TFs of **1** of varying thickness were characterized by atomic force microscopy (AFM, Figure 3.5). For the thinnest samples, the β polymorph is dominant (as deduced from XRD and absorption studies), and nucleation of these crystallites can be seen in the 2 nmthrough40 nm thick samples. In the 80nm sample, nucleation of elongated crystallites can be detected. When a much thicker layer (80–200nm) is deposited, a very distinct patterning of crystallites becomes apparent. Crystallites of form α are densely packed 0.1 × 3μm ribbon-like structures that arrange in a continuous layer on the substrate, whereas β crystallites are disordered and bordered by exposed substrate. It appears as though nearly full substrate coverage is required in order to grow α-form crystallites, probably because crystals in contact with the substrate favor the lower energy β phase at thermodynamic equilibrium. Upon thermal annealing, the crystallites sinter or

fuse into rods with dimensions of about 1 × 5μm. Crystallite sizes and shapes are less clear in solvent dropcast samples, but the XRD peak FWHM values are similar to those of thermally evaporated films, indicating similar grain sizes.

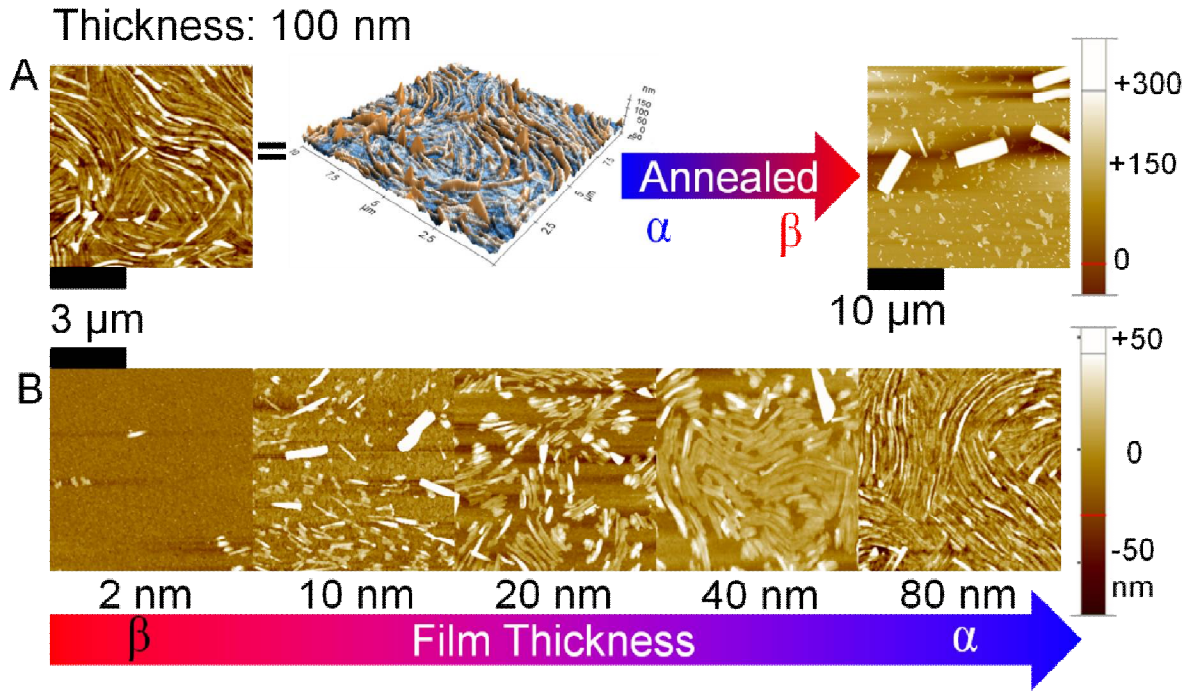

Figure 3.5

AFM images of films:(a)Effect of annealing on evaporated films. (b) Evaporated film morphology as a function of thickness.

XRD and UV-vis absorption spectra of TFs were collected during a room temperature annealing series (Figure 3.6a), monitoring the conversion of the films from α to β form. The relative intensity of the form β diffraction peak increased with respect to the intensity of that of the α form. The XRD data were background subtracted directly using the spectra of a blank substrate and were fitted using a function consisting of a series of Pearson curves, Equation 3.1.

$$\sum_{N=0}^{N_{tot}} \frac{A_N}{\left(1+\left[\frac{(x-x_{0N})}{\gamma_N}\right]^2\right)^n} \qquad (3.1)$$

In (1), A_N is the amplitude, $(x - x_{0N})$ represents the specific diffraction peak position on the 2θ axis, γ_N is the peak width parameter, and n is a variable exponent. Also included in the fit is a quadratic baseline function. An example of the fitting function and its individual components can be found in Figure 3.6b. The individual Pearson curves were extracted from the fit function and integrated. The ratios of areas of $\alpha:(\alpha + \beta)$ peaks from XRD analysis were mapped to a mole fraction χ_α, assuming that X-ray scattering cross sections for the (004) peaks are the same in the two polymorphs. Mole fractions were plotted against the A_2:A_1 ratio of intensities of the first two vibronic features of the UV-vis absorption spectra (Figure 3.4). The results are shown in Figure 3.6c, exhibiting a linear correlation. We note that while this is semi-quantitative (amplitudes are measured from extinction and not pure absorption spectra and are not determined by a fit), this analysis does provide practical guidelines for quickly and reliably gauging the morphology of TFs of **1**.

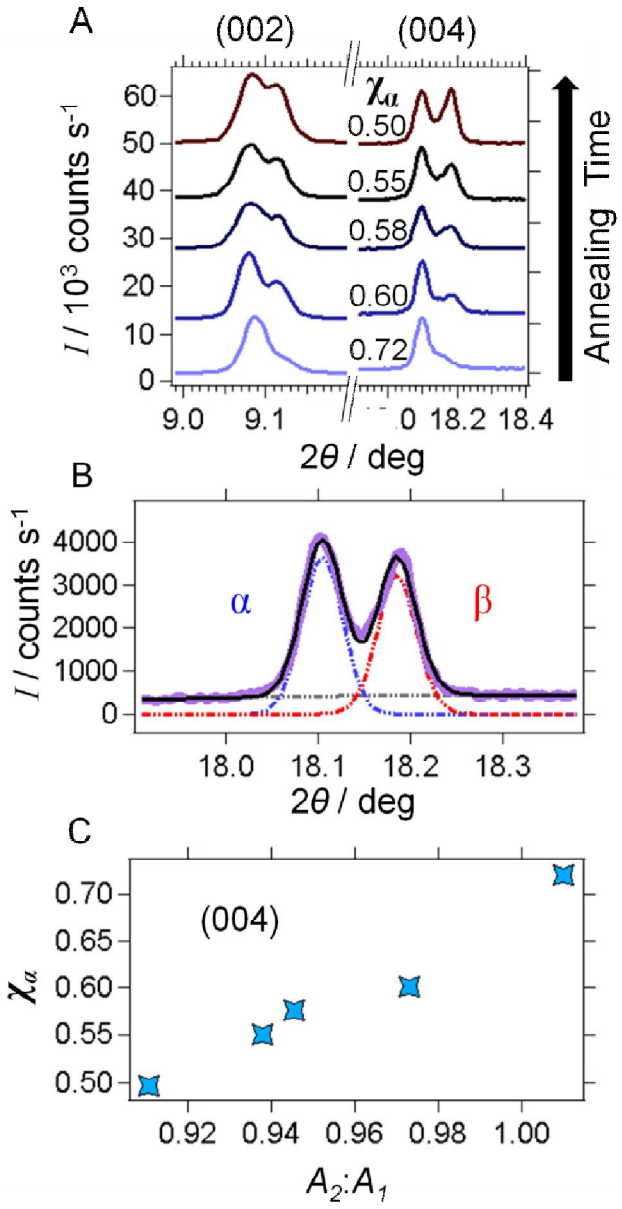

Figure 3.6

XRD analysis of room-temperature annealing of TFs of **1**.(a) Overview of the (002) and (004) reflection regions vs. annealing time. (b)Fit of α and β (004) diffraction peaks. (c)Mole fraction α, χ_α, determined from fits of the (004) diffraction peaks vs. A_2:A_1.

The extinction spectra of α and β films of **1** differ significantly, and the distinctions can be used to immediately characterize the film polymorph (Figures 3.4,3.7). β-**1** films contain a lowest energy vibronic feature that is larger in amplitude than the neighboring peak, and for α-

1films the opposite is true. During the thermal annealing process the ratio of the two peaks changes, in line with what is observed in XRD. A thermal annealing series of a TF of **1** is shown in Figure 3.7b. It is evident that some material is lost during the annealing process, as the overall extinction decreases with each annealing step. This is due to sublimation and not degradation, since dissolving annealed β-**1** films in acetonitrile and comparing the solution spectra to those of unannealed α-**1** films also dissolved in acetonitrile revealed no evidence for the presence of degradation products of **1**. This is also confirmed by the loss of material when stored in ambient conditions for a few days, as the films eventually disappeared completely. Thermal annealing steps were carried out on a hot plate under inert conditions, so the well-known oxidation products of **1**, which include insoluble oligomers,[103,104] were not expected to form.

3.3.3. Determination and Analysis of Pure Optical Absorption

Considering the crystallite shapes and sizes for α vs. β films determined by AFM, it is not surprising that β-**1** films exhibit a larger degree of visible light scattering. Scattering by nano- or microscopic crystallites would be difficult to account for by simply assuming a functional form of the scattering efficiency vs. wavelength and subtracting it from the extinction spectra. Moreover, the reflectivity of the two film polymorphs is not separated from pure absorption by extinction measurements. In order to accurately correct for these effects, an absorption spectrophotometer with an integrating sphere (IS) was utilized to measure reflectance (scattering) and transmission, and thus obtain the pure absorption spectra. The IS absorption spectra films were fitted using a modified Franck-Condon (FC) progression, which is a function consisting of a series of Gaussian curves, Equation 3.2.

$$\sum_{N=0} \frac{AS^N e^{-S^N}}{N!} \left(1 - \frac{BSe^{-S}G_m}{2}\right)^2 e^{-\frac{1}{2}\left(\frac{E-\left(E_{00}-NE_{\mathrm{ph}}\right)}{w/\sqrt{8\ln 2}}\right)^2} \qquad (3.2)$$

In this expression, *A* and *B* are amplitudes, *w* is the peak width,[105,106] E_{00} is the absorption onset, E_{ph} is the energy of the dominant vibrational mode coupled to the transition, *S* is the Huang-Rhys factor and $G_m = \sum_{m,n\ (m \neq n)} \frac{S^m}{m!(m-n)}$. With *B*> 0, the model describes a system in which H-type aggregation exists, such as has been observed in polymers and carotenoid aggregates.[105,106] Coupling of transition moments changes the distribution of oscillator strength among the vibronic features from what is expected in a FC progression.

The spectra of mixed α/β-**1** films could not be satisfactorily fitted with one or two FC progressions (B = 0). With *B* = 0.5, excellent fits are achieved for films dominated by crystallites of α-**1,** exhibiting *S* of about 1.9. A satisfactory fit of the β-**1** spectra is obtained with a single FC progression (*B* = 0), although a small degree of H-type interactions (B < 0.05) cannot be ruled out. β crystallites have an *S* value of 1.2. The absorption onsets of α and β crystallites are about 22800 cm^{-1} and 22200 cm^{-1}, respectively, and the vibrational mode energies are approximately 1350 cm^{-1} and 1280 cm^{-1}, respectively, characteristic of unsaturated ring skeletal modes. An example of the raw data, multiprogression fit, and individual progressions are shown in Figure 3.7c. Note that IS absorption measurements were performed in air due to the nature of the instrument and often required one to two hours to complete. Thus, a change in the composition of these films to higher χ_β values may have occurred during the measurement. The absorption spectra are slightly temperature dependent. Upon cooling, absorption features narrow, increase in intensity by 10–15%, and blue-shift by about 200 cm^{-1}. No other temperature-dependent changes were observed.

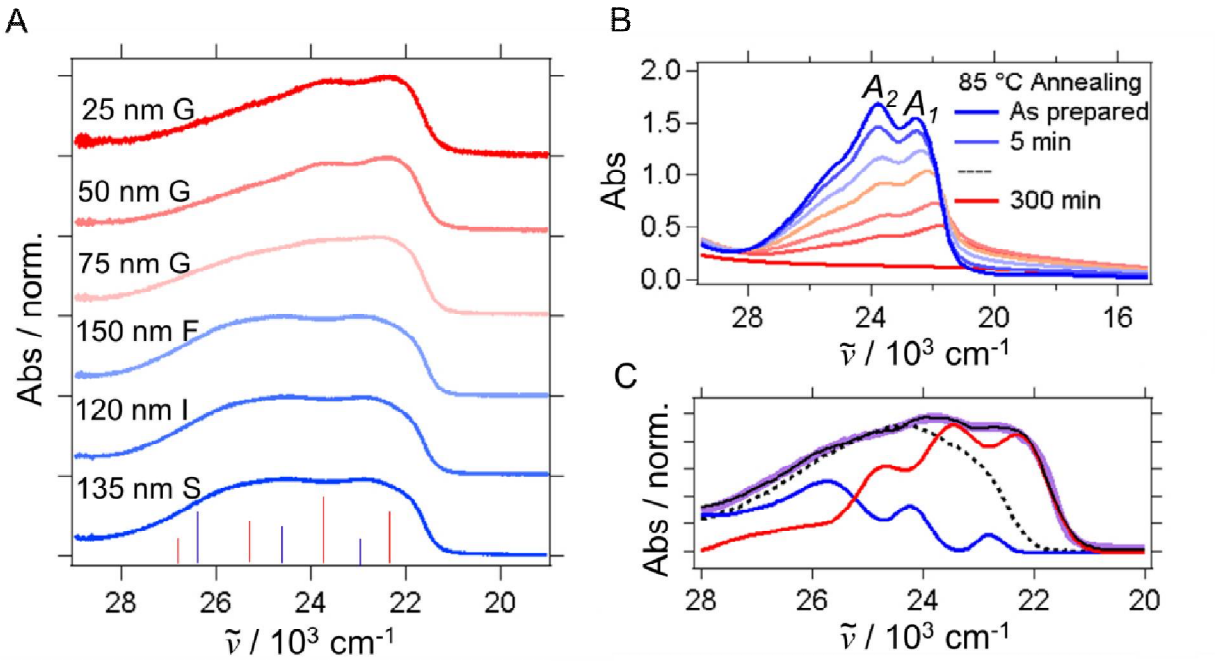

Figure 3.7

(a)Absorption spectra (red and blue traces) from UV-vis IS experiment, calculating absorbance using $A = -\log(T + R)$. Also listed are sample thicknesses and substrate: F = fused silica, G = glass, I = ITO, S = sapphire. (b) UV-vis extinction spectra of thermal annealing series. (c) Normalized raw data (purple) shown with multiprogression fit (black), α-**1** progression fit (blue), β-**1** progression fit (red), and **1** absorption in 3-methylpentane (dashed).

3.3.4. Bulk and Thin Film Fluorescence

Fluorescence spectra of the bulk crystals closely resemble those of the respective TF types. Emission from α-**1** crystals shows a greater intensity on the higher energy end of the spectrum than β-**1** crystals. Fluorescence quantum yields Φ_F of TFs at room temperature increase upon film annealing, from 0.16 for the α-**1** film to 0.59 for a highly β-**1** film. Φ_F for bulk crystals could not be reliably obtained, but visual inspection (Figure 3.1) clearly indicates more strongly fluorescent rods compared with blocks. The steady state fluorescence spectra of both film polymorphs display a complex temperature dependence (Figures3.8a,b), with more than one vibronic progression contributing. Fluorescence spectra of α- and β-**1** (80 nm thick, *OD*

values of ~0.8) films at various temperatures were integrated, and their areas were plotted as a function of temperature in Figure 3.8c.

For thick films, excitation through the substrate yields a fluorescence spectrum that contains less of the highest energy feature and less of the low energy tail, consistent with preferential excitation of β-**1** that forms near the substrate. Excitation of the top surface of the TF produces greater fluorescence intensity in the higher energy region of the spectrum, likely due to the α-**1** material grows more readily farther from the substrate. These TF spectra closely resemble those of the bulk crystals. The emission lineshape of a β-**1**TF is comprised of a FC progression arising from prompt fluorescence from vibronic levels of the S_1 state, as well as a broad Gaussian feature (Figure 3.9). The Gaussian peak is enhanced under excitation at higher photon energies.

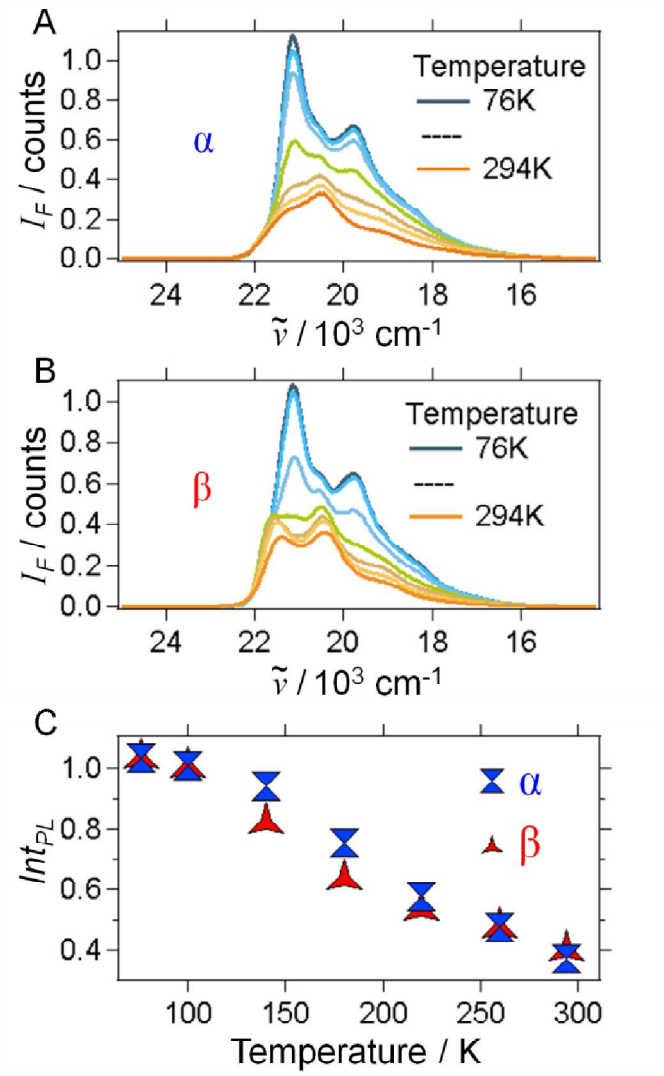

Figure 3.8

(a), (b)Temperature-dependent fluorescence spectra (normalized to the peak intensity at 76 K) of α and β-**1** films. (c)Integrated areas, Int_{PL}, of α and β TF fluorescence spectra vs. temperature.

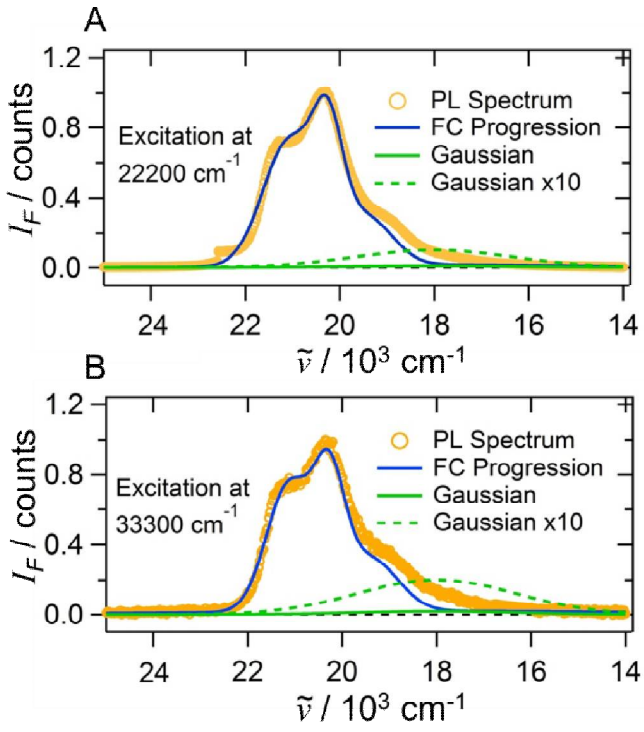

Figure 3.9

Fitting of steady-state fluorescence (normalized) of β-**1**TF at two excitation energies (a) 22200 cm^{-1} and (b) 33300 cm^{-1}.

3.3.5. Time Resolved Fluorescence

Time-resolved fluorescence decays (Figure 3.10) for α-**1** films detected at 20200 cm^{-1}contain at least four decay components, with lifetimes of ~380 ps, 1.3 ns, 5 ns, and 17ns. At 20200 cm^{-1} fluorescence decays are biexponential in β-**1** films with lifetimes of 1.3 ns and 3.3 ns. At 15385 cm^{-1} detection there is a significant long-lived fluorescence component only for α-**1** films. The fastest component is near instrument-limited and likely corresponds to the SF process that dominates the photophysics in α-**1** films, and has been previously shown by transient absorption to proceed with time constants of 2.0 ps and 25 ps at room temperature.[56] The slower than 15 ns component has a small amplitude when the fluorescence is detected at 20200 cm^{-1}, but has a much larger amplitude when monitoring the fluorescence at 15385 cm^{-1}. This slow

component is much less prevalent in β-**1** films and is considerably longer than the radiative decay time of S_1 of the isolated monomer (~6 ns). A compilation of the most relevant amplitudes and lifetimes can be found in Table 3.2.

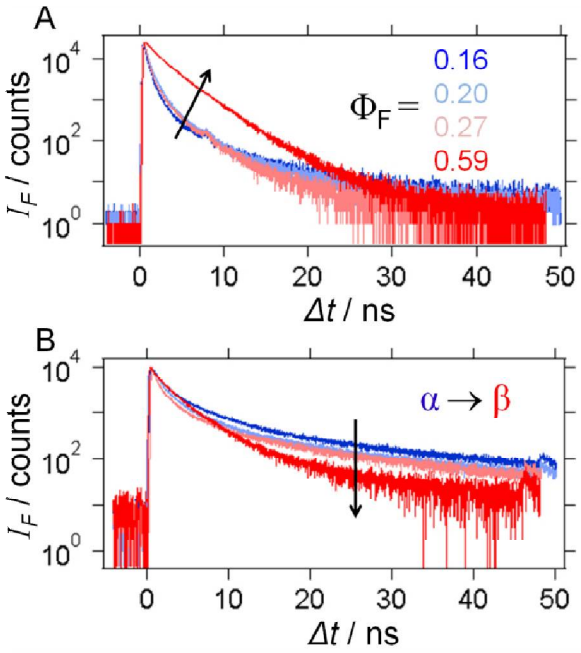

Figure 3.10

(a), (b)Time-resolved fluorescence data collected from films of varying composition at emission energies of 20200 and 15385 cm^{-1}, respectively.

Table 3.2

Fitting parameters of time-resolved fluorescence decays for α-**1** and β-**1**TFs.

	α	β
Φ_F	0.16	0.59
$\tilde{\nu}_{ex}$ (cm^{-1})	20200	20200
A_1	0.87	--
τ_1 (ns)	0.38	--
A_2	0.12	0.54
τ_2 (ns)	1.3	1.3
A_3	0.08	0.46
τ_3 (ns)	4.9	3.3
A_4	0.001	--
τ_4 (ns)	17	--

In bulk single crystals, fluorescence decay features similar to those of TFs are observed. For mostly β-**1** films, the fluorescence rises in intensity over the first few ns when detecting around 15385 cm^{-1}, indicating population transfer from higher to lower energy emitting states. At 20200 cm^{-1} (Figure 3.11a), α-**1** bulk crystals have two fluorescence decay components, one with a lifetime of 700 ps and a longer-lived decay component with a lifetime of 4.9 ns. β-form bulk crystals have decays with lifetimes of 1.9 ns and 5.8 ns when probed at 20200 cm^{-1}. At 15385 cm^{-1} (Figure 3.11b), α-form bulk crystals display two decay components with lifetimes of 4.9 and 16.6 ns, whereas β-**1** is dominated by a 5 ns decay after the initial rise.

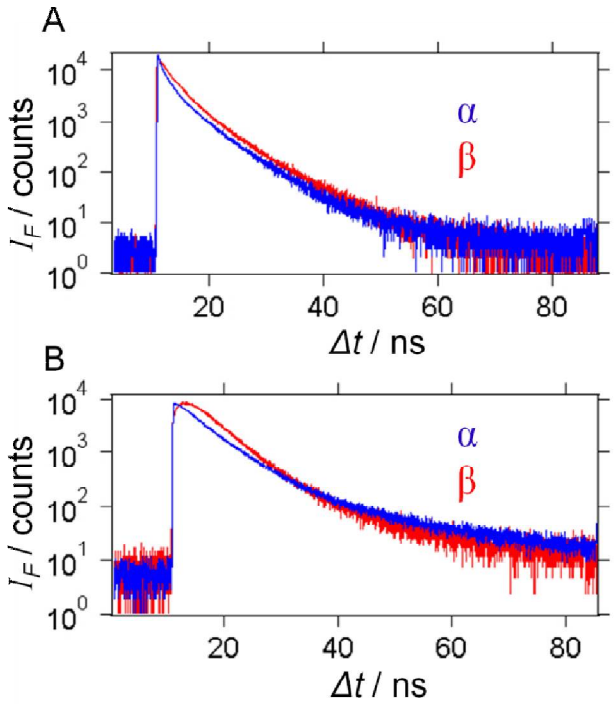

Figure 3.11

Time-resolved fluorescence decays from α (blue) and β-form (red) bulk single crystals of **1**, collected at emission energies of (a) 20200 cm^{-1} and(b)15385 cm^{-1}.

3.3.6. Singlet Fission and Davydov Splitting Calculations

Results of calculations of the Davydov splitting between pairs of molecules in the unit cell for α-**1** and β-**1** are shown in Table 3.3. The intermolecular geometries used in the SF and Davydov splitting calculations for the two morphologies are shown in Figure 3.12. The greatest Davydov coupling is roughly 750 cm^{-1}, slightly larger in β-**1** than in α-**1**. Calculation of the SF matrix elements divided into contributions from the direct and mediated mechanisms are also shown. The contribution from the direct mechanism is at most 0.021 meV, much smaller than the maximum mediated value of 1.85 meV. The value for the mediated contribution depends inversely on the energy separation between S_1 and the charge transfer state, estimated here to be 25 kcal/mol, which is approximately its value in a covalently bound dimer in a nonpolar medium.[81] It is notable that the molecular pairs producing the highest value of Davydov splitting and mediated SF matrix element were not situated within the molecular column with slip-stacked orientation but rather in neighboring columns.

Table 3.3

Calculated SF matrix elements (meV) and Davydov splittings (cm^{-1}) for pairs of molecules in the two different crystal polymorphs (Figure 3.12). Mediated pathway assumes ΔE=25 kcal/mol.

	Block (α-1)				Prism/Rod (β-1)			
	Direct	Mediated	Sum	Davydov	Direct	Mediated	Sum	Davydov
AB	0.0218	0.8266	0.8483	-30.7979 (248.4)	0.0218	0.9505	0.9722	29.9244 (241.4)
AC	0.0027	-1.8522	-1.8495	91.4630 (737.7)	-0.0027	1.6453	1.6426	93.0684 (750.6)
AD	0.0027	-0.0366	-0.0339	-8.5308 (68.8)	0.0027	-0.0373	-0.0346	8.5008 (68.6)
BC	-0.0109	0.3188	0.3079	8.5335 (68.8)	0.0109	-0.2960	-0.2852	8.9798 (72.4)
BD	0.0027	-1.8521	-1.8494	91.4602 (737.7)	-0.0027	1.6448	1.6421	93.0494 (750.5)
CD	0.0218	0.8266	0.8484	30.7951 (248.4)	-0.0245	-0.8295	-0.8540	29.9162 (241.3)

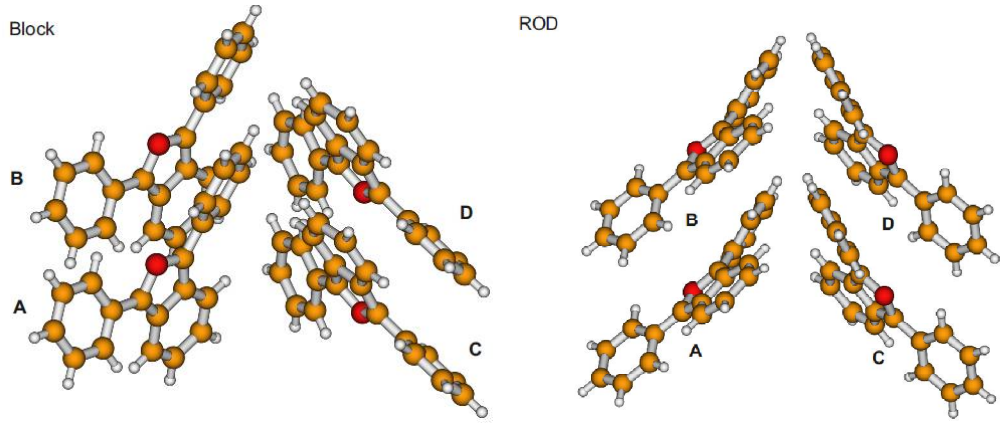

Figure 3.12
Block (α) and prism/rod(β) intermolecular geometries used for SF and Davydov calculations.

3.3.7. Transient Absorption

Much of this data was collected and analyzed by Joel Schrauben, and Joel, Justin, and I have effusively participated in determining the findings stated below. The S_1-S_n and T_1-T_n spectra can be extracted in an approximate fashion by adding to the observed transient spectra a scaled amount of the known S_0-S_1 absorption spectrum. The initial concentration of molecules with excitations in the S_1 state, $[S_1]$, is determined at a pump-probe delay of 400 fs, which lies just after the overlap of the pump and probe pulses. The maximum concentration of molecules in the T_1 state, $[T_1]$, is determined at 165 ps. The spectra collected at 400 fs and 165 ps time delay on a film of mostly α-**1** crystallites are shown in Figures 3.13 (c), (d). Using the molar extinction coefficients measured for solutions of **1** ($\varepsilon(S_1) = 23400\ M^{-1}\ cm^{-1}$ at 14500 cm^{-1}; $\varepsilon(T_1) = 32100\ M^{-1}\ cm^{-1}$ at 21800 cm^{-1}; $\varepsilon(S_0) = 25000\ M^{-1}\ cm^{-1}$) we calculate $[S_1]_{400\ fs} = 2.8\times10^{-5}$ mol $cm^{-3}$and $[T_1]_{165\ ps} = 4.7 \pm 0.2 \times10^{-5}$ mol cm^{-3}, indicating a 165 ± 10 % Φ_T.[107,108] Overall, Φ_T, is calculated by Equation 3.3.

$$\Phi_T = \frac{\Delta A^T}{\Delta A^{S_1}} \frac{\varepsilon_{S_1}}{\varepsilon_{T_1}} r \qquad (3.3)$$

where ΔA^{T} is the transient signal of the triplet absorption (T1 $\rightarrow$ Tn, late time), ΔA^{S_1} is the transient signal of the excited state singlet absorption, (S1 $\rightarrow$ Sn, early time), ε_{S1} is the extinction coefficient of the S1 state, ε_{T1} is the extinction coefficient of the T_1 state. The factor r is the correction that accounts for the special case of non-aligned (molecular frame) and non-isotropic (laboratory frame) bleach and triplet transition dipole moment orientations. The concentration of molecules with a depleted ground state is assumed to be equal to [S_1] at 400 fs. Using the known S_0-S_1 absorption spectrum and the extracted S_1-S_n and T_1-T_n spectra the concentrations of S_0, S_1, and T_1 can be extracted at each delay time of the transient absorption experiment, shown in Figure 3.13 (e). In this treatment the resulting S_1-S_n spectrum also contains the stimulated emission feature. The extracted concentrations as a function of pump-probe delay time are also represented as normalized to the initial [S_1] (Figure 3.13 (e), right axis). In addition to the normalized [T_1] reaching values much larger than one at delay times > 20 ps, further bleaching of [S_0] concomitant with the rise in [T_1] matches our previous report, and offers conclusive evidence for SF.[109]

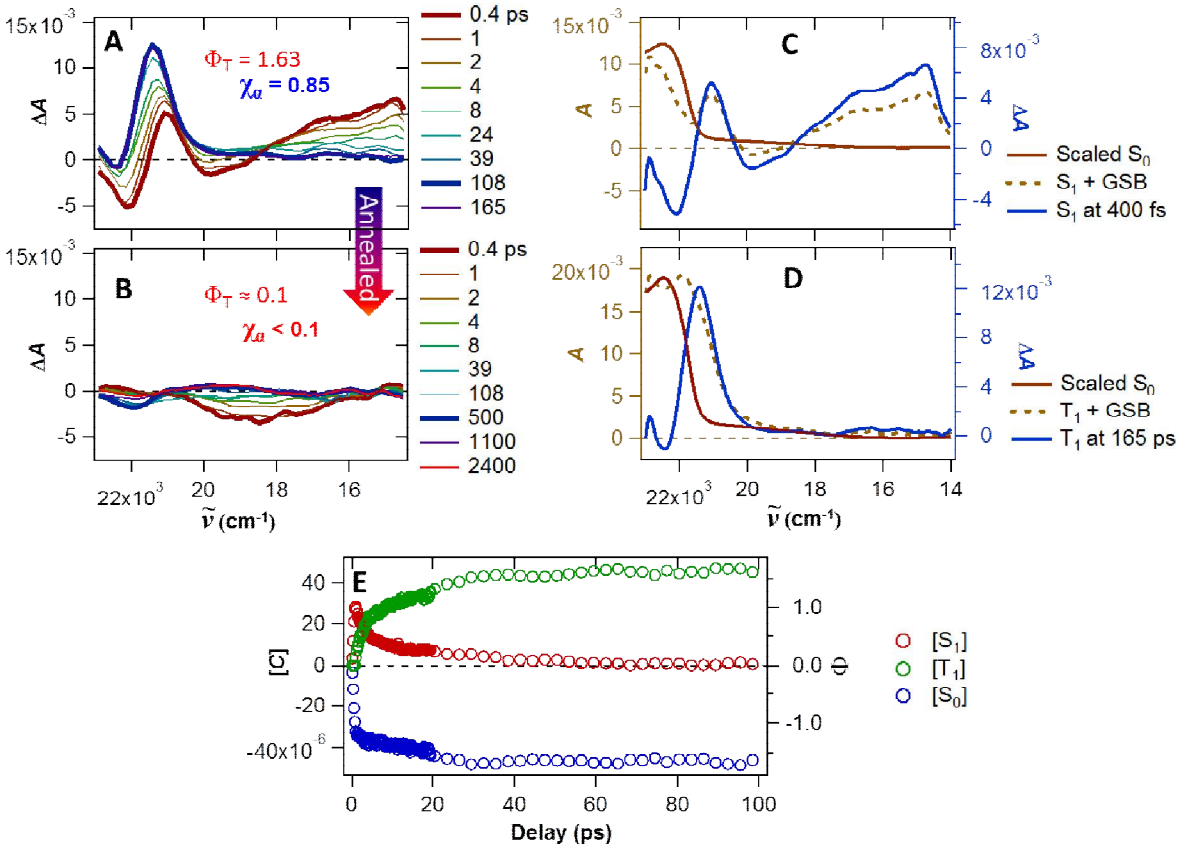

Figure 3.13

(a) Measured absorbance change Δ*A* vs. time of a mostly α-**1** film at 295 K. (b) Spectra after annealing to create a film of mostly β-**1**. (c) S_1-S_n and (d) T_1-T_n spectra for the α-**1** type film in panel A. *A* is the absorbance of each species determined from the extracted spectrum. (e) Extracted state concentrations at each delay time. [C] is concentration (in units of mol cm^{-3}) and Φ is the yield of population in S_0, S_1 and T_1 states.

As the films become further enriched in β-**1** crystallites, the transient absorption measurements become increasingly difficult due to increased light scattering from the larger β-**1** crystallites. The top panel of Figure 3.14 shows a typical series of transient spectra for a β-**1** film, and the lower panels compare the short and long delay time spectra to the extracted S_1-S_n and T_1-T_n absorptions for the α-**1** film from Figure 3.13. The spectra at delay times greater than 100 ps are somewhat similar to those observed for α-**1** films at longer delays, but appear to contain more residual S_1-S_5 absorption than α films at a similar delay. At 400 fs, the transient spectrum is

dominated by a broad stimulated emission feature that overlaps strongly with the S_0-S_1 bleach and the S_1-S_n absorptions. The broad stimulated emission is spectrally similar to steady-state fluorescence. Fluorescence excitation spectra were acquired for both mixed composition α/β and highly β films in order to distinguish features characteristic of each crystallite type. When the fluorescence spectra are normalized at 20355 cm^{-1}, both mixed and highly β-**1** enriched films show slightly larger amplitude at longer wavelengths (largest noticeable amplitude change at 18940 cm^{-1}) when excited above ~25000 cm^{-1}. This additional fluorescent component is quite broad, which suggests an origin from trapped exciton or excimer species. The broad, red-shifted fluorescence is more pronounced for the film composed mostly of β-**1**. At room temperature the fluorescence spectra of β-**1** can be well described by a single vibronic component with a Huang-Rhys factor of 0.6–0.75 and a vibronic spacing of 1070 cm^{-1} summed with a broad Gaussian component centered around 19600 cm^{-1} with a width of ~2000 cm^{-1}. These results are characteristic of fluorescence arising from both the S_1 state and from an excimer/trap state.

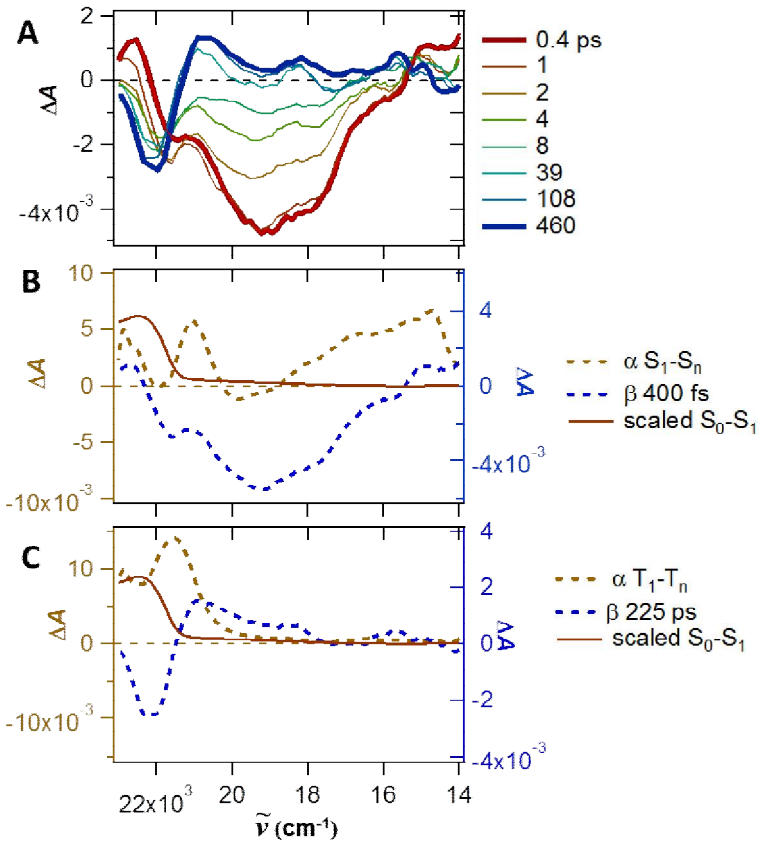

Figure 3.14

(a) Transient absorption spectra of a mostly β-**1** film ($\chi_\alpha \approx 0.25$) at 295 K with 25800 cm^{-1} excitation at delay times indicated. (b), (c) Comparison of the S_0-S_1 absorption and the extracted S_1-S_n and T_1-T_n features from Figure 3.13 with the (b) short and (c) long delay time features of a β-**1** enriched film.

The triplet formation onset for the β-**1** film, as measured through a series of flash photolysis experiments, is shifted to higher energy by approximately 900 cm^{-1} from the film absorptance onset (Figure 3.15, bottom spectrum).For a film containing roughly an equal mixture of the two polymorphs the triplet formation follows the absorptance onset (Figure 3.15, top spectrum).

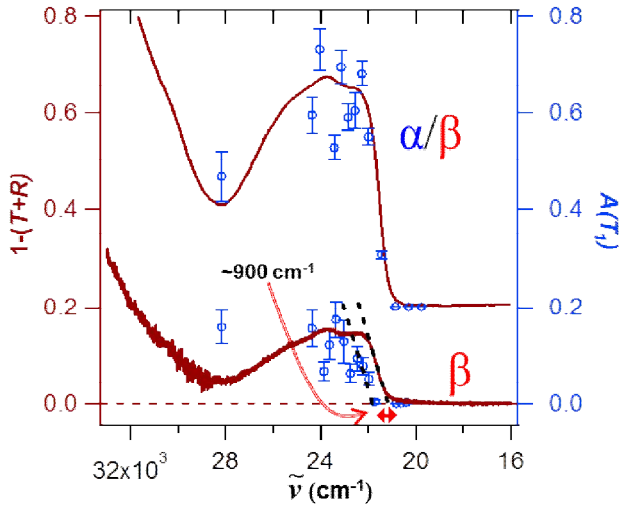

Figure 3.15

Circles, triplet action spectra of a mostly β-**1** film (bottom, χ_α<0.1) and α/β film (top, χ_α = 0.45), monitored at 21500 cm^{-1} while scanning the excitation energy. The triplet amplitudes are extracted from a monoexponential fit of the decay of the T_1 transient. Solid lines, absorptance spectra for the corresponding films.

Ultrafast transient absorption measurements as a function of excitation fluence were carried out to test whether annihilation processes may be affecting triplet formation kinetics and yield. Triplet formation and S_1 decay kinetics were monitored as a function of fluence at several temperatures from 30 K to 295 K. The experiments were carried out on a film of mostly α-**1**, and the concentration profiles were extracted as described above. While there are changes in the excited state kinetics with fluence, the spectral features for the S_1-S_n and T_1-T_n absorptions and the S_0-S_1 bleach are unaffected. The observed decrease in Φ_T at 80 K as a function of increasing fluence (Figure 3.16) reveals that singlet-singlet annihilation (SSA) plays a role in the excited state kinetic scheme at this temperature.[110] Further evidence for SSA can be found by monitoring the T_1-T_n and S_1-S_n absorption maxima, Figures 3.16 (c), (d). The kinetic traces in this figure are normalized at short delay times when measuring [S_1] and long delay times when monitoring [T_1],

and the traces are fitted with a biexponential function. As the excitation fluence is decreased, there is a clear loss of the fast decay component in [S_1] and the corresponding fast rise component in [T_1]. The fractional amplitude of the fast [S_1] decay component ($R_{fast}=A_{fast}/A_{total}$, monitored at 15000 cm^{-1}) at 80 K is plotted with Φ_T, showing that for the lowest fluences at which Φ_T is highest, the decay of [S_1] is described well by a single exponential. The increase in R_{fast} with higher fluence was observed at all temperatures, but the correlation with Φ_T varies. The temperature dependence of Φ_T previously reported[109] is reproduced at low fluences, Figure 3.16 (b), but the trend becomes weaker at higher fluences.

Transient spectra on films that are highly enriched in the α polymorph were also recorded at different excitation energies across the S_0-S_1 absorption. Upon comparing [S_1] and [T_1] kinetics for a few different fluences at room temperature, the kinetics are similar for those recorded at low and moderate fluences, indicating that a regime where SSA is negligible is accessible. Triplet yields at 30-295 K and representative transient kinetics, acquired at 80 K at different excitation energies across the S_0-S_1 absorption, are presented in Figure 3.17. Although the error bars for the measurements of Φ_T are quite large (especially at 22200 cm^{-1} excitation, where the scatter of the excitation beam overlaps strongly with T_1-T_n absorptions) Φ_T generally reaches a maximum of ~2 at 23810 cm^{-1} excitation (420 nm) at all temperatures, and at 30 K and 295 K decreases at higher and lower excitation energies, while at 80 K and 180 K the Φ_T values are within error. At high fluences triplet-triplet annihilation (TTA) is observed at delay times greater than 100 ps through monitoring the T_1-T_n absorption maximum, which persists for many ns with negligible decay at lower fluences.[111] As demonstrated by time-resolved fluorescence data,[112] TTA processes involving free and trapped triplet excitons can occur over time scales extending out to ~50 ns, accounting for the delayed fluorescence. The temperature dependence of

these processes, in addition to the likely presence of both polymorphs in any film, accounts for the rich variability observed in the temperature dependent fluorescence spectra.

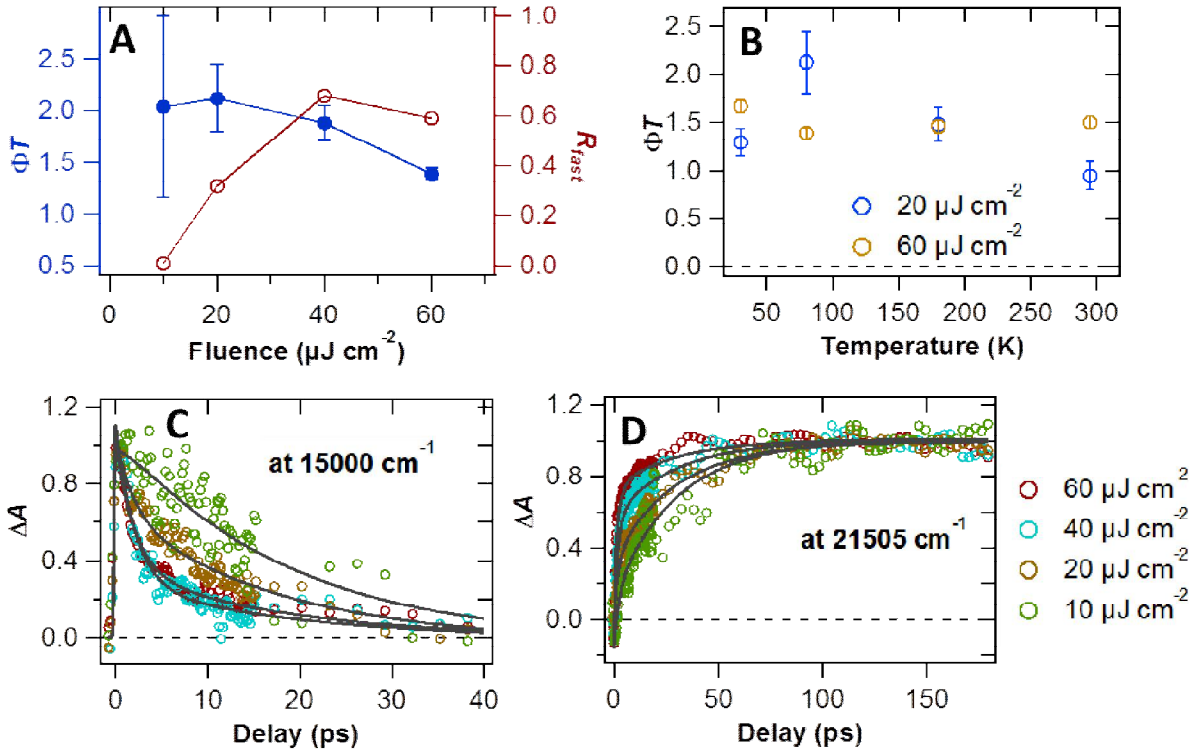

Figure 3.16

(a) Φ_T and R_{fast} as a function of excitation fluence (25800 cm^{-1}) at 80 K for an α-rich film (χ_α = 0.85). (b) Temperature dependence of Φ_T at high and low fluences. (c), (d)Normalized kinetics monitoring S_1-S_n (15000 cm^{-1}) and T_1-T_n (21505 cm^{-1}) absorption maxima at the indicated fluences at 80 K.

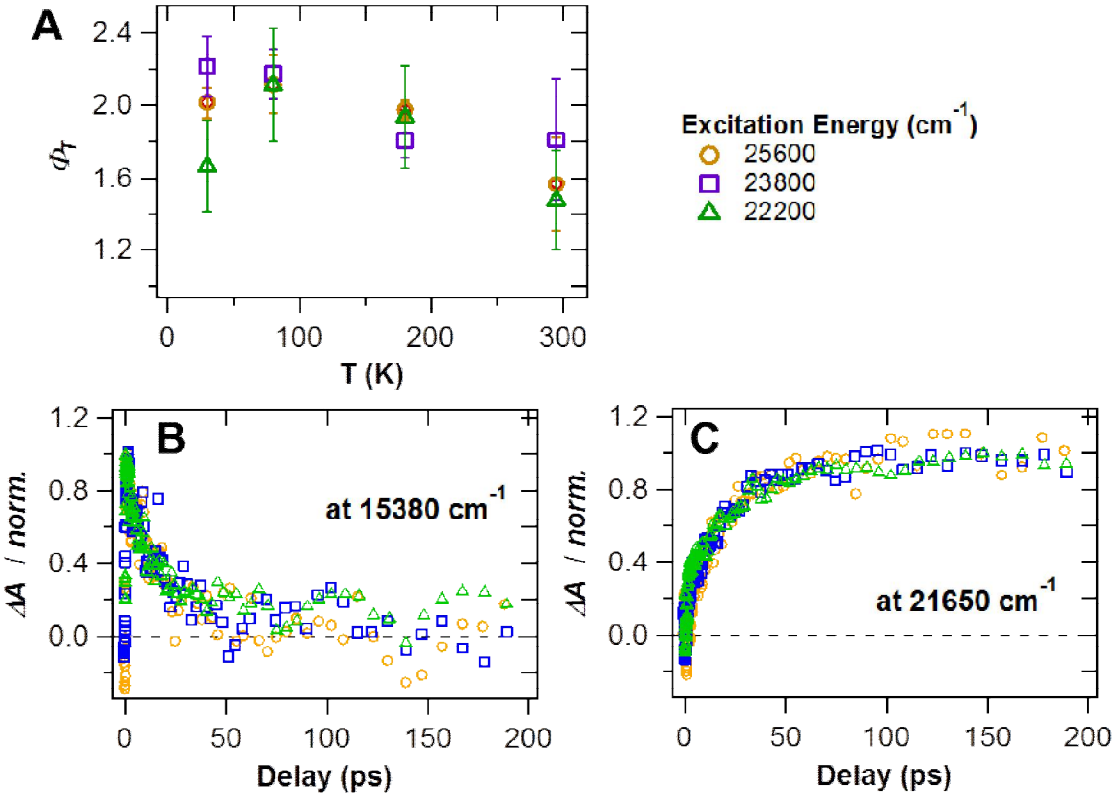

Figure 3.17

(a) Φ_T of a film composed of mostly α-**1** (χ_α = 0.83), at 30 K, 80K, 180 K and 295 K, recorded after excitation at three different energies across the S_0-S_1 absorption at low fluence (~10 μJ cm^{-2}). (b), (c) Normalized transient dynamics at 80 K as a function of delay time after excitation at three different energies across the S_0-S_1 absorption at low fluence (~10 μJ cm^{-2}), monitoring the decay of the S_1-S_n absorption at 15380 cm^{-1} (b) and the growth of the T_1-T_n absorption at 21650 cm^{-1},(c). Panels (b) and (c) use the same marker shapes and colors as panel (a).

The possibility of a phase change induced by cooling was explored as a possible additional modifier of Φ_T vs. temperature. Cycling the temperature several times from 30 – 295 K before performing a series of transient absorption measurements did not change Φ_T. Allowing the sample to equilibrate at 77 K for only a few minutes vs. > 1 hour prior to measurements also resulted in similar Φ_T. Morphology changes that are fast and reversible may not have been detected using this approach. The absorption spectra of films of α-**1** are very weakly temperature

dependent,[109,112] which provides further evidence that a temperature-dependent phase change is unlikely.

3.3.8. Modeling

3.3.8.1. Excited State Relaxation in Films of β-1

Fitting of the absorption spectra reveals that the spectrum of β-**1** can be described by a single Franck-Condon progression, whereas the α-**1** component requires a more complicated H-aggregate model.[112] This suggests that exciton delocalization is more important in the description of α-**1** than in β-**1**, but the similarity to the absorbance of isolated **1** implies that the delocalization is not great in either polymorph. This is in contrast, for example, to the very large differences in the absorption spectra of crystalline versus solution phase linear acenes.[113,114] Excitons in crystalline Tc, for example, can extend over ~10 molecules, as determined by superradiance.[115]

Fluorescence quantum yields at room temperature increase upon film thermal annealing, from 0.16 for α-**1**to 0.59 for β-**1**, suggesting that excited states of β-**1** decay primarily radiatively. The similarity between the low temperature fluorescence spectra of α and β films leads to the conclusion that at low temperatures, when α crystallites are highly efficient at SF, the small amount of β crystallites in these films are dominating the fluorescence. Fluorescence spectra indicate a broad fluorescent component that underlies the much stronger fluorescence that is presumably from S_1. The broad feature matches closely the excimer emission observed for crystalline perylene films.[116] This excimer fluorescence is much more pronounced at higher energy excitations and in β-enriched films. The more strongly fluorescent S_1 state dominates SSPL, and this state can be modeled with a single Franck-Condon progression. The time resolved fluorescence decays of these films reveal radiative decay from two different states, with

lifetimes of 1.3 ns and 3.3 ns. Similar decay lifetimes are observed, along with two other components, in mostly α-**1** films, again highlighting that even the most highly enriched α-**1** films contain some amount of fluorescent β crystallites.

The triplet action spectra (Figure 3.15), while containing considerable uncertainty, fit well with a model in which the β-**1** crystallites do not produce two T_1states from thermalized S_1 but can in higher lying vibrational levels. XRD studies revealed residual α-**1** features even after extensive annealing,[112] thus it remains possible that the triplets that are observed in an enriched β-**1** film are arising from a small fraction of α-**1** crystallites present in the sample, which have much higher Φ_T than β-**1** crystallites. However, the onsets in the triplet action and absorptance spectra for mixed films are nearly identical to the absorptance onset for β-**1,** while the triplet onset of β-**1** is blue-shifted, indicating that excess energy above thermalized S_1 is required to produce T_1 in β-**1.** The different triplet onsets for the mixed vs. β-**1** films suggest that residual α-**1** is not responsible for the small amount of triplets formed in highly β-**1** films.

The transient spectra at early delay times are dominated by a broad stimulated emission feature that resembles the excimer fluorescence identified in the steady state fluorescence of β-enriched films (*vide supra*). The transient spectra of β-**1** films at delay times longer than 100 ps appear somewhat similar to those observed for α-**1** films, and if the transient absorption feature near 21000 cm^{-1} is dominated by T_1-T_n contributions, then comparison of its amplitude with that of the S_0-S_1 bleach feature suggests a much lower Φ_T than in α-**1** films. Since it is known from the high Φ_F that a large number of singlets remain at times longer than 100 ps, S_1-S_5features in this spectral region convoluted with the ground state bleach could also produce transient spectral features that strongly overlap with T_1-T_n and result in the spectrum for β-**1** shown Figure 3.14 (c).

The unique triplet action spectrum of β-**1** compared with films enriched in α-**1** (Figure 3.15) suggests that β-**1** can form triplets only upon excitation with photon energies well in excess of the absorption onset. SSA could also occur at high excitation fluences, promoting **1** to a higher lying S_n state that can undergo SF more readily, which explains the observation under strong excitation of a fast rise component at the position of T_1-T_n absorbance (near 21500 cm^{-1}), even in highly β-**1** films. A fluence of the appropriate magnitude to incite SSA cannot be achieved in the time-resolved fluorescence experiment, thus the lack of a fast decay or delayed fluorescence is not evidence against SSA-induced SF. In transient absorption experiments that operate under much higher fluences, the effect is more likely at work, but the triplet yields even at the highest fluences used are still quite low, < 0.3.

Taken together, observations of excited state behavior for β-**1** crystallites strongly imply that the dominant relaxation pathway is fast (< 1 ps) formation of a species with excimer character followed by its cooling/trapping and radiative decay. Similar behavior is observed in the two polymorphs of perylene: SF occurs in β-perylene with little excess excitation energy but is suppressed in α-perylene, which forms excimers with rate constants exceeding 10^{12} s^{-1}.[117,118] In **1**-β we label this dominant singlet state as S_1/Ex (Figure 3.18) and note that as in α-perylene it forms in 1 ps or faster, based on the broad stimulated emission features observed at the earliest times in our ultrafast transient absorption experiment. Evidence is also present for triplet formation via SF that can arise at excitation energies more than 900 cm^{-1} higher than the absorption onset. The mechanism may be due to singlet fission proceeding from higher-lying S_n that is formed via SSA (again, with rise times less than 2 ps). A separate mechanism may be through a vibrationally hot S_1, similar to SF in α-perylene where the onset of triplet formation is blue-shifted by 3500 cm^{-1} from that of the β polymorph.[118]

3.3.8.2. Excited State Relaxation in Films of α-1.

The low Φ_F, high Φ_T, and observation of delayed fluorescence are all consistent with SF being the dominant excited state pathway in α-**1** films. The steady state fluorescence spectra of α-**1** films display a complex temperature dependence. For α-**1** the trend in Φ_T and SF rise times would suggest that fluorescence at 80 K (~200% Φ_T) is nearly entirely delayed in nature, while at higher and lower temperatures other species (*e.g.*, excimers, traps of various types)could be contributing. Also possible is that β-**1**, which was shown to grow near the substrate prior to the growth of α-**1**, is dominating the fluorescence via direct excitation or through energy transfer from α-**1** crystallites. At lower temperatures fluorescence spectra for a film primarily composed of β-**1**crystallites are very similar to those observed for films enriched in α-**1**. Apparently the dominant delayed fluorescence signals in α-**1** films at low temperatures arise from similar species as those in β-**1**films, and it is difficult to determine what fraction of the emission arises from the small amount of β-**1** that is present. In the time resolved fluorescence measurements the strong presence of decay components associated with β-**1**crystallitesis further evidence that the fluorescence of mostly α-**1**films is dominated by the small fraction of β-**1**. Unique fluorescence decay components of α-**1**crystallites are indicative of SF and delayed fluorescence.

The transient absorption spectra of α-**1** films at short delay times match closely the S_1-S_n absorption observed in solutions,[119] and at delay times greater than 100 ps the transient spectra are easily identified as arising from the T_1-T_n absorption, also through comparison with measurements in solution. Transient absorption measurements vs. excitation fluence indicate that SSA is an important process that modulates Φ_T and produces the faster triplet rise time. The temperature dependence of the SSA process, or that of a competing process, is evident in the large effect of SSA at low temperatures and the weaker influence at 295 K (data presented in

Figure 3.19). SSA still results in the formation of T_1, but if it were the only mechanism of triplet formation, the maximum Φ_T would be 100% because half of the S_1 excitons are lost in the SSA process. Thus, in systems where SF is fast and barrierless from S_1, SSA is a loss mechanism and is avoided by extrapolation to very low fluence conditions. However, in mixed films of **1** some gain in Φ_T could result at higher fluences because the SF rate constant increases sharply with excess energy given to the singlet species of β-**1** that, when fully relaxed, is unlikely to undergo SF. The unique temperature dependence of the TQY at high vs. low fluence is evidence that the relative impact of SSA on the dynamics is temperature dependent.

TTA is revealed by the delayed fluorescence observed for α-**1** films; the low fluence conditions of the time resolved fluorescence experiment result in a lifetime for the delay fluorescence of ~17 ns. At the higher fluences used in the transient absorption experiment higher overall concentrations of T_1 are produced and the delayed fluorescence lifetime is likely shorter.

Under low fluence conditions, at 25800 cm^{-1} excitation and temperatures other than 80 K, Φ_T is lower than the maximum of 2, indicating that a loss mechanism other than SSA is operative. This process may be trapping or excimer formation from S_1, or internal conversion from S_1 that competes with the ~25 ps SF process. Φ_T recorded at 30 K, 80 K, 180 K, and 295 K after low fluence excitation at different energies across the S_0-S_1 absorption, Figure 3.17, indicates that the excitation energy is also an important factor in the fate of the initially prepared S_1 species. The Φ_T values and $[S_1]$ and $[T_1]$ kinetics recorded after excitation at various energies at low fluences do not show a monotonic trend that is associated, for example, with higher rates of SF when SF is more exothermic; rather, at 30 K and 295 K Φ_T reaches at maximum at 23810 cm^{-1} excitation, near the peak of the S_0-S_1 absorption, and decreases at higher and lower excitation energies. At 80 K and 180 K the Φ_T values at the different excitation energies are

within error of each other, and near the maximum of 2.The [T_1] and [S_1] kinetics (presented in Figure 3.20) recorded at low fluence do not contain the rapid components observed at higher fluences and attributed to SSA. The high Φ_T at 23810 cm^{-1} excitation may indicate that there is a SF contribution arising from a vibrationally excited level of S_1. This is the case, for example, in the SF dynamics of rubrene, which shows two time constants for SF of 2 ps and 25 ps;[120,121] the faster time constant for SF has been attributed to "direct" SF from a vibrationally hot state, while the slower time constant arises from a thermally activated fission process.[120] k_{sf} also changes dramatically across the linear acene series (anthracene, Tc, pentacene) as the S_1-2×T_1 splitting increases.[122] The lack of a rapid T_1 formation component at higher excitation energies observed in Figure 3.20 indicates that if SF is occurring from higher-lying vibrational levels of S_1 that it is not nearly as rapid as in rubrene. The decrease in Φ_T at excitation energies higher than 23810 cm^{-1} may be indicative of strongly activated excimer or trap formation. The lower Φ_T at 22200 cm^{-1}, close to the S_0-S_1 absorption onset, arises from a competition between SF and trapping, both of which have barriers from the bottom of S_1.

Based on the observations described above we aim to develop a model that is capable of fitting [S_1] and [T_1] concentration profiles vs. time delay *t* at different fluences and correctly reproduces the temperature dependence of Φ_T. A simple model is used (Figure 3.18, middle) to first assess the role of SSA as a function of fluence. The α-**1**/high fluence model includes SSA, fast SF from the S_n prepared via SSA that competes with internal conversion back to S_1, and a slower SF process that occurs directly from S_1 to 2×T_1, accounting for the entire triplet population at sufficiently low fluences. TTA is not included in the α-**1**/high fluence model, which aims only to describe the kinetics at delay times shorter than 1 ns. Fast triplet formation via SSA to S_n accounts for the initial rapid rise in [T_1] over the first few ps. S_n sits well above the

threshold for SF, and the model assumes that SF is extremely efficient once S_n is formed. This is the case, for example, in rubrene crystals that have SF time constants of 2 and 20 ps when excited near the absorption onset, but display much faster SF ($\tau \sim 200$ fs) when excited into higher S_n.[121] In addition to the higher exothermicity of SF from S_n increasing the rate constant for SF, accessing higher S_n may also promote SF through accessing intermolecular vibrations that prepare intermolecular geometries poised to generate ^{1}(TT).[123]Figure 3.19 shows a global fit of fluence dependent measurements at 30 K, 80 K, 180 K and 295 K. The fits were carried out through numerical integration of the series of differential equations that describe the α-**1**/high fluence model. All of the rate constants were treated as global variables, and the initial $[S_1]$ concentration was linked between the solutions of $[S_1](t)$ and $[T_1](t)$ at a given fluence. The best fit parameters are presented in Table 3.4.

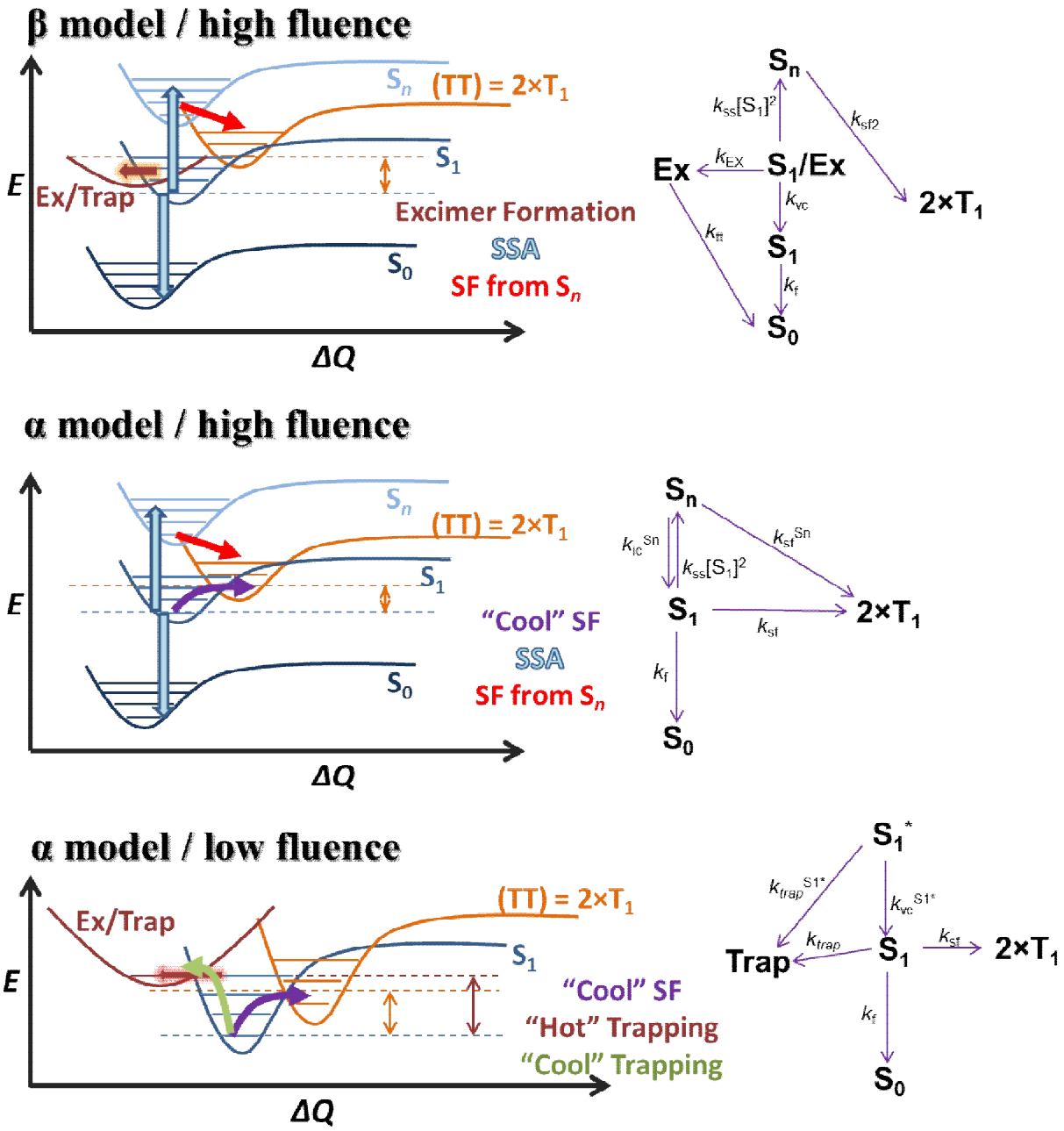

Figure 3.18

Top: Kinetic scheme for films of β-**1**. Middle: Kinetic scheme for fitting the fluence-dependent data. Bottom: Kinetic scheme for fitting the low fluence data.

The equations resulting from the α-**1**/high fluence model provide satisfactory fits to the data. The best fits of the fluence-dependent datasets reveal that the rate constant for SSA, k_{ss},

decreases as temperature is increased, from ~9×10^{-9} cm^{-3} s^{-1} at 30 K to ~5×10^{-9} cm^{-3} s^{-1} at room temperature. These values are comparable to the SSA rate constant recently reported for amorphous films of 5,12-diphenyltetracene (k_{ss} = 3.9×10^{-9} cm^{-3} s^{-1}),[110] and slightly lower than the SSA rate constant recently reported for Tc films (k_{ss} = 1.7×10^{-8} cm^{-3} s^{-1}).[124] SSA is much more pronounced at lower temperatures, perhaps indicating longer diffusion lengths at these temperatures,[125] or reflecting the contraction of the unit cell as the crystal is cooled.[112] k_{sf} roughly follows the observed temperature dependence of Φ_T. The ratio k_{sf}^{Sn}/k_{ic}^{Sn} indicates that SF is highly efficient from S_n, and k_{sf}^{Sn} values imply a time constant for this process of ~ 200 fs. The fluorescence rate constant k_f is small enough to have negligible effect on the fit over the time window of the experiment and was held near the value observed in time-resolved fluorescence experiments.

A shortcoming of the α-**1**/high fluence model is the poor fit of $[S_1]$ over the first few hundred fs for datasets recorded at the highest fluences. Constraining the fitted $[S_1]$ to be equal to the observed initial value resulted in poor fits to both the $[S_1](t)$ and $[T_1](t)$ profiles in all cases. We attribute the poor fits at the highest fluences to rapid S_1 decays within the instrument response as a result of SSA. This is consistent with the slight increase in Φ_T that are observed at higher fluences (*e.g.*, Figure 3.16 (b)), because the observed initial $[S_1]$ is defined after 200 fs of population evolution, and if it is already slightly depopulated, Φ_T becomes inflated. We note that the overshoot of $[S_1]$ in fits of α-**1** films mentioned above may also be due to altered peak molar extinction coefficients compared with solution, or incomplete separation of S_1-S_n and T_1-T_n spectra due to their considerable overlap and convolution with the instrument response at short delay times. Allowing the peak extinction coefficients to vary such that the fit improves also modifies the calculated Φ_T, but by a factor smaller than our reported uncertainty. The α-**1**/high

fluence model also tends to underestimate [S_1] at longer delay times and high excitation fluences, which could result from not accounting for TTA processes that feed population back to S_1.

Table 3.4

Extracted rate constants from fits to transient data using α-**1**/high fluence model.[a]

T (K)	k_{sf} (ps^{-1})	k_{sf}^{Sn} (ps^{-1})	k_{ss} ($cm^{-3}\ s^{-1}$)	k_{ic}^{Sn} (ps^{-1})	k_{sf}^{Sn}/k_{ic}^{Sn}
30	.023	5.0	8.7×10^{-9}	1.1	4.5
80	.028	6.0	8.9×10^{-9}	1.0	6.0
180	.025	5.0	5.0×10^{-9}	1.9	2.6
295	.030	5.0	5.2×10^{-9}	1.6	3.1

[a] k_f held at 0.0003 ps^{-1} in these fits.

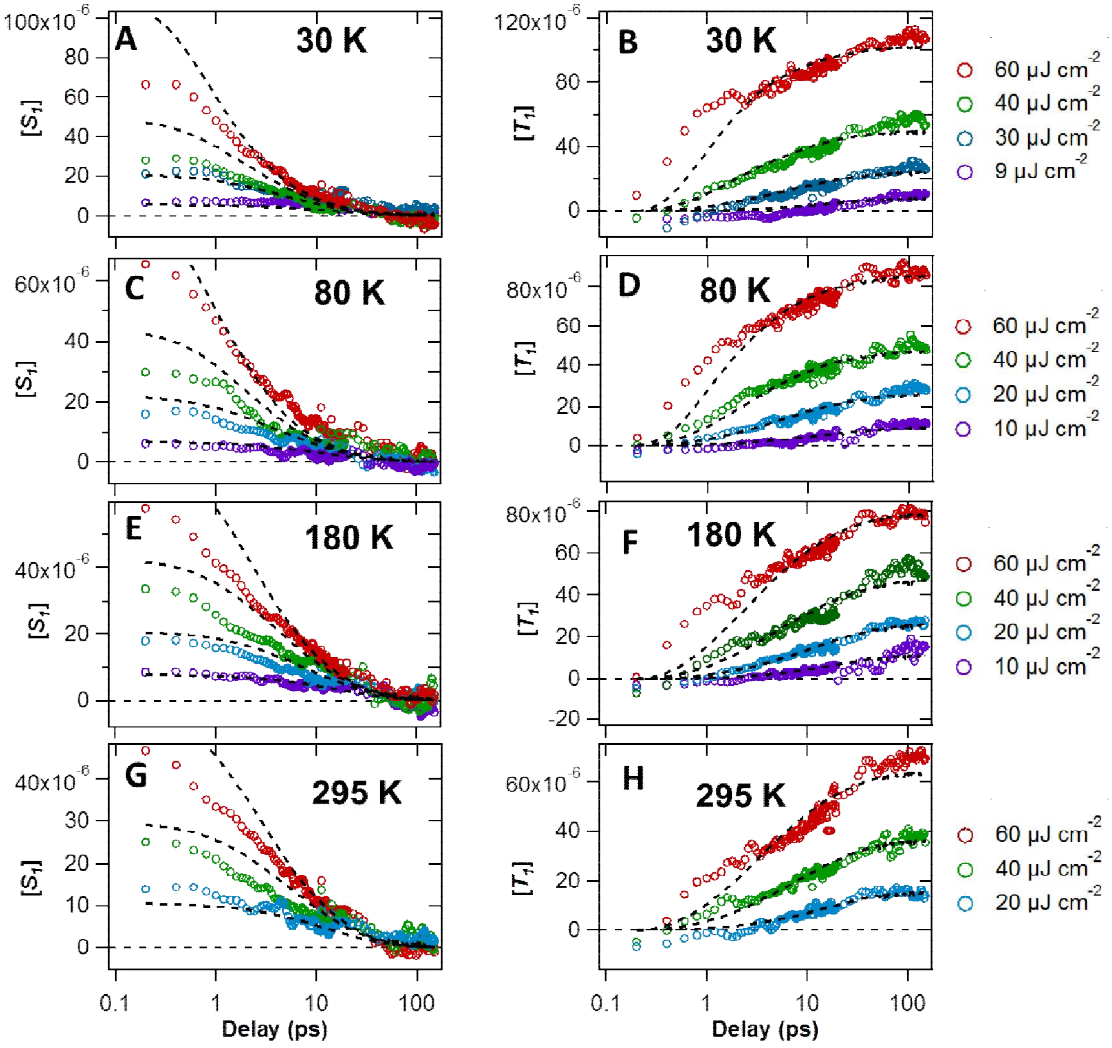

Figure 3.19

Fits with the α-**1**/high fluence model. Global fits (dashed lines) of (a) $[S_1]$ and (b) $[T_1]$ (both in mol cm^{-3}) of a highly α film (χ_α = 0.85) across a range of fluences. (a), (b) 30 K (the fluences are indicated in the legend to the right of panel B); (c), (d) 80 K; (e), (f) 180 K; and (g), (h) 295 K. The best fit parameters are presented in Table 3.4.

Next we examine the kinetics at low fluence in the absence of SSA using a model (Figure 3.18, bottom) that accounts for excitation energy dependent Φ_T values. A trap state, such as the excimer that dominates the excited state dynamics in β-**1** films, is invoked as a competitor to SF to account for $\Phi_T < 2$. The excitation energy dependent Φ_T values are rationalized by introducing a trapping process from the initially prepared (hot) S_1 state (S_1*) that competes with vibrational

cooling on the S_1 surface, as well as an additional slower trapping process from the thermalized S_1. The data and fits using these equations are presented in Figure 3.20, and the best fit parameters can be found in Table 3.5.

The best fit parameters reveal that "hot" trapping is an important contributor to α-**1** photophysics at higher excitation energies: k_{trap}^{S1*} increases with increasing excitation energy, and this trend is the most pronounced at 180 K and 295 K. At most temperatures and excitation energies Φ_T is very close to 2, and in these cases trapping is minimal. The fits also indicate a weaker impact from trapping via thermalized excitations as temperature decreased below 295 K, consistent with an activation barrier to trapping from the bottom of S_1. k_{sf} varies for different excitation energies at a given temperature, but the values remain within the considerable uncertainty for the low fluence measurements. k_{sf} does not track the excitation energy, or change significantly with temperature, so there does not seem to be any evidence for SF from vibrationally excited levels or for a significant barrier to SF. Although the calculated energetic barrier is approximately 800 cm^{-1}, entropic contributions could lower this barrier, as has been discussed for Tc.[126]

In summary, the analysis of the low-fluence variable temperature and excitation energy kinetics of $[S_1]$ and $[T_1]$ supports a nearly temperature independent rate of SF, but trapping becomes a significant competitor of SF at higher excitation energies and at temperatures above 180 K.

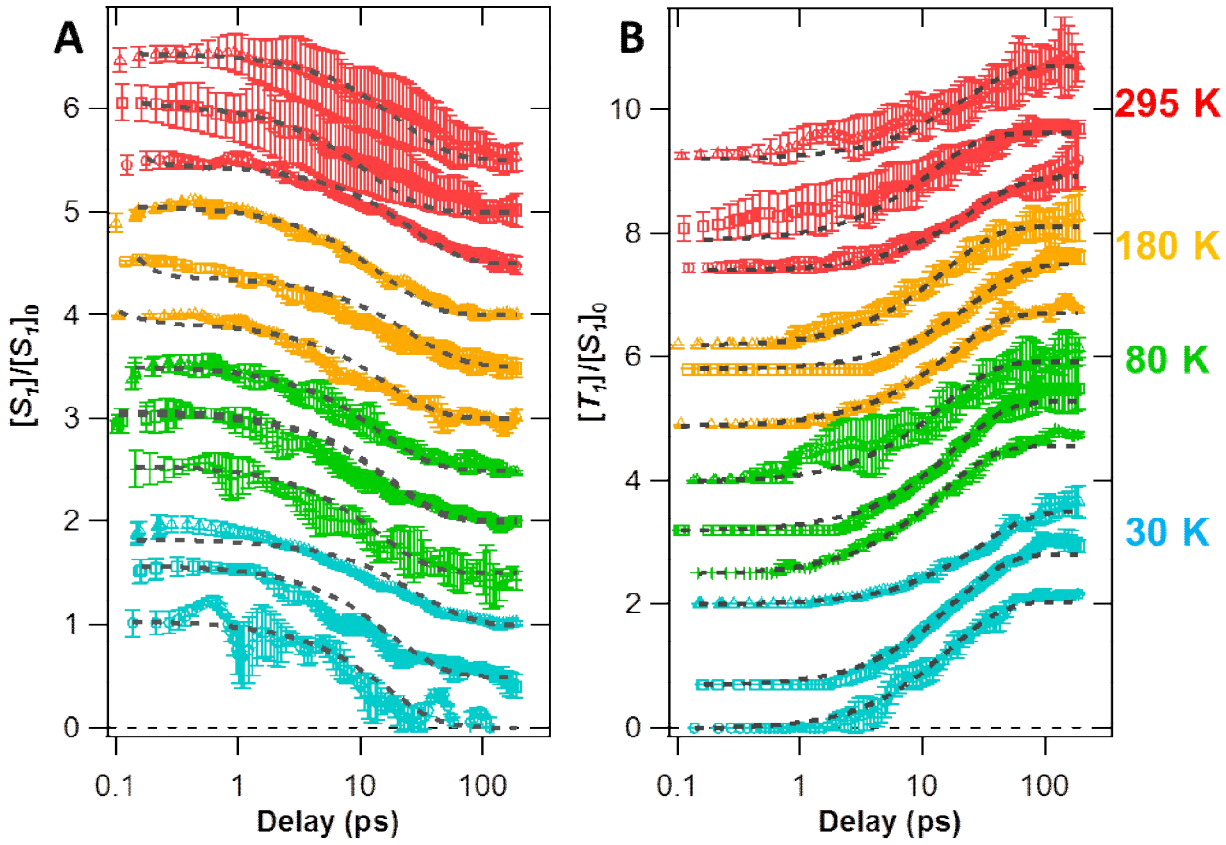

Figure 3.20

Fits with the low fluence α-**1**model.(a), (b) Global fits of A. $[S_1]$ and B. $[T_1]$ at 30 K, 80 K, 180 K and 295 K at three different excitation energies. The data and fits are normalized by the initial $[S_1]$ and offset for clarity. Circles: excitation at 25600 cm^{-1}; squares: excitation at 23800 cm^{-1}; triangles: excitation at 22200 cm^{-1}. The films have a high α-**1** content, with $\chi_\alpha = 0.85$. The error bars are one standard deviation of the extracted concentration, from measurements that sample several locations on the film.

Table 3.5

Extracted rate constants from the global fitting of the fluence-dependent datasets using the α-**1**/low fluence model (all rate constants are ps^{-1}).

T (K)	Excitation (cm^{-1})	Φ_T	k_{sf}	k_{sf} (avg)	k_{vc}	k_{trap}^{S1*}	k_{trap}
30	**2.22×10^4**	1.67 ± 0.25	0.031	0.049 ± 0.015	13.6	0.0001	0.0021
	2.38×10^4	2.22 ± 0.17	0.055		16.0	0.0001	0.0001
	2.56×10^4	2.02 ± 0.16	0.060		12.9	0.0770	0.0001
80	**2.22×10^4**	2.11 ± 0.31	0.066	0.064 ± 0.008	15.2	0.0001	0.0011
	2.38×10^4	2.17 ± 0.14	0.0547		15.8	0.0001	0.0001
	2.56×10^4	2.11 ± 0.16	0.071		16.0	0.0150	0.0001
180	**2.22×10^4**	1.94 ± 0.28	0.060	0.052 ± 0.013	16.1	0.0001	0.0050
	2.38×10^4	1.81 ± 0.10	0.038		14.9	0.6000	0.0001
	2.56×10^4	1.98 ± 0.05	0.060		14.1	1.8900	0.0001
295	**2.22×10^4**	1.48 ± 0.27	0.035	0.047 ± 0.023	16.1	0.0154	0.0124
	2.38×10^4	1.81 ± 0.34	0.073		15.4	0.5900	0.0127
	2.56×10^4	1.57 ± 0.26	0.032		15.0	1.1100	0.0071

[a] k_f held at 0.0003 ps^{-1} in these fits.

3.4. Discussion

3.4.1. Structural Properties of the Two Polymorphs

Photophysical From the close alignment of XRD peaks, the similar crystallite habits, and the fluorescence properties we can assign the film forms α and β of **1**with some degree of certainty to the bulk crystal structures with space groups *P*2/*c* (blocks) and $P2_1/c$ (rods or prisms), respectively. Remaining uncertainty resides in the known possibility of unique TF polymorphs not found in the bulk.[127] In the case of **1**, packing perpendicular to the substrate must remain similar in both polymorphs in order to account for the correlation between predicted and observed powder XRD peaks, but subtle changes in π-stacked columns parallel to the substrate

could occur. The similarity in molecular packing of the α and β-form bulk crystals suggests that the structures should be similar energetically, and indeed the difficulty in producing pure films of either polymorph is evidence of this. The proclivity of α-**1** films to undergo a phase transition to form β-**1** crystallites suggests that the latter form is more stable thermodynamically, and the fact that this can occur even at room temperature implies that minimal molecular rearrangement is necessary for the transition to occur. β-**1** films are also preferred at slower deposition rates, further implying their thermodynamic stability. Nonetheless, it is seems that once formed in thick layers, some amount of α-**1** persists even after relatively long periods of annealing (Figure 3.6a). For XRD analysis, some preferential probing of α-enriched regions farthest from the substrate (and slowest to convert to β-**1**) may occur, although the penetration depth should exceed the film thickness.[128] Higher temperature annealing may aid in the full conversion but also hastens sublimation.

The reason for the initial formation of a thin β-**1** layer during vapor deposition before α-**1** layers can grow is not immediately clear. One possibility is that the locally elevated temperature that results from molecular bombardment of the substrate surface favors β-**1**. We could then expect that substrates with higher thermal conductivity would form α-**1** layers more readily. This seems to be true: ITO and sapphire have the highest thermal conductivity and exhibit the lowest l_{th} for the changeover to α-**1** crystallite growth. However, a systematic correlation between thermal conductivity and l_{th} was not evident among all the substrates used. It was expected that deposition on a cooled substrate might lead to lower β:α composition ratios for thinner films, but this does not appear to be the case. Strain differences between the polymorphs on different substrates may also play a role, resulting in more facile growth of the α polymorph once a layer of **1** completely covers the substrate. Substrate polarity differences do not seem to be a major

factor, as evidenced by the lack of control over α:β ratios after treatment of the substrates with several hydrophobic or hydrophilic organosilanes.

The existence of similar polymorphs is common to many other material systems,[91,129] but a particularly relevant example is perylenetetracarboxylic dianhydride (PTCDA),[130] in which α and β forms are grown via thermal evaporation under different conditions. In that case, the α form is prevalent near the substrate and mixed α/β films are produced as the films thicken. Steady-state absorption PTCDATFs exhibit modified shapes and similar shifts (~500 cm^{-1}) to those observed for **1** as the α:β ratio is varied.[131,132] A specific growth mechanism for the two types of films or a model for the modified absorption was not presented but was generally ascribed to changes in electronic or exciton-phonon coupling. In some cases, thickness dependent absorption spectra have been misinterpreted as being due to polymorphism,[133] when in fact the polarized absorption due to Davydov splitting is responsible. We rule out such a contribution in the case of **1** since the presence of two polymorphs is clearly identified by XRD analysis.

Ostensibly, the strongest pairwise intermolecular interactions in both forms are within slip-stacked columns (aligned along the *b*-axis for blocks and *a*-axis for prisms), which are modified only slightly between α and β-**1** crystallites. However, differences in packing along different crystal axes are apparent. In β-**1**, the molecular arrangement within the unit cell is more compact than in α-**1**. For example, while viewing the unit cell down the *b*-axis, the two pairs of nearly perpendicular molecules are all eclipsed in β, while the equivalent view along the *a*-axis of the α form reveals that the two pairs are offset by 5.5 Å. These differences lead to unique longer-range molecular packing, as evident in Figures 3.1, 3.2.

3.4.2. Photophysical Differences Between α-1 and β-1 Polymorphs

The primary photophysical differences between α-**1** and β-**1** films are modified steady-state absorption and the dominance of SF vs. excimer formation. Here we list and discuss the most likely reasons for modified photophysical behavior given the polymorph crystal structures: (i) amorphous or disordered material; (ii) change in excitonic coupling; (iii) changes in inter-stack molecular interactions.

Although good fits to the XRD data for each of the bulk crystals were obtained, the possibility of a larger degree of disorder in the β-type crystal can be seen in the higher value of R_{int}, 6% vs. 1.6% for the α-type. R_{int} increases with temperature for β–**1** but not for α–**1**, possibly indicating that crystalline regions more easily become disordered in the β form upon heating. The degree of disorder may be even larger in the nano- and microcrystalline films grown from thermal evaporation. Surface effects could be substantial, creating quasi-amorphous regions that influence the photophysics even if the overall proportion of such regions is relatively small. Thermal annealing of TFs results in conversion of α-**1** crystallites to β-**1**, as well as sublimation. It is not apparent that amorphous material crystallizes upon annealing or that there is a significant amount of amorphous material present at all, as evidenced by no clear change in peak width or strength upon annealing, as well as the absence of broad features in the diffraction spectra.

Trapping at lattice defects increases the probability of fast energy loss from the initially excited S_1 state and should lower the SF efficiency. Although R_{int} decreases for the bulk β form crystal with lower temperature, high triplet yields are not restored, suggesting that disorder inferred from bulk crystal structure determinations does not influence SF dynamics. The fit of β–**1** absorption reveals a lower Huang-Rhys factor than that of α-**1**, which could be explained by

a change in ground state molecular conformation. We have measured absorption spectra of the two conformers (C_2 and C_s) and found that they differ primarily by their value of *S*.[80] However, the two molecular geometries as determined from the bulk crystal structure differ only very slightly, and both belong to the C_2 conformer. It is possible that an undetected concentration of C_s conformers or otherwise altered molecular geometries in β**–1** may facilitating trapping.

Excitonic coupling is most often inferred from absorption spectra.[106] The fact that pure β-**1** absorption spectra can be fitted with a single FC progression, while mostly α-**1** films require a more complicated model, suggests that excitonic coupling is different in the two forms. The highest calculated Davydov coupling is larger in β-**1**(751 cm^{-1}) than α-**1**(737 cm^{-1})(Table 3.3) but by only about 15 $cm^{-1}$and does not seem to be responsible for the 600 cm^{-1} red shift for β-**1** crystallites. However, a change in the oscillator strength of the split transitions between polymorphs may modify the absorption envelope. Generally speaking, the higher degree of H-aggregate behavior, the more the higher-lying exciton transition gains oscillator strength at the expense of the lower-lying transition,[134] which may be responsible for the additional amplitude on the blue side of the α-**1** S_0-S_1 absorption. Clear evidence for Davydov splitting in the experimental absorption spectrum of the films is not seen, and may be explained by broad vibronic features that obscure the splitting. In principle, further evidence should be found in polarized spectra, but the fact that the largest excitonic interactions are between molecules in the *a-b* plane leaves the split transitions in the substrate plane. Since the films have uniaxial symmetry (i.e., the spectrum is independent of the polarization direction in the substrate plane), the oppositely polarized Davydov split peaks cannot be modulated by rotating or tilting the film under polarized light. This splitting should be observable for polarized absorption experiments

on an oriented single crystal, but to this point crystal size and purity have not been sufficient enough to achieve high quality absorption spectra.

Excimer formation is most often inferred from steady-state and time-resolved fluorescence. The overall intensity of steady-state fluorescence I_F as a function of temperature (Figure 3.8c) reveals moderate thermal quenching in both crystalline polymorphs. Since it is known that in α-**1** SF is not significantly thermally activated,[56] the fluorescence quenching is not likely due simply to the opening of the SF pathway at higher temperatures. In addition, the similarity in the I_F vs. T trends for the two polymorphs despite the much lower triplet yield in β-**1** films argues against a simple competition between SF and ordinary fluorescence from S_1. Instead, other species are involved in the competition. The variable temperature steady-state fluorescence measurements of TFs of **1** (Figures 3.8a, b) reveal similar progressions in both film polymorphs, which likely arise from the fact that α-**1** films contain a layer of β-**1** crystallites that have a high Φ_F and dominate the fluorescence signal when they are excited directly or receive population via energy transfer. A broad Gaussian feature, more pronounced in β-**1** films, is likely due to a lower-lying (E-type) excimer state. A recent study on peropyrene revealed two different fluorescent states, as deduced from a variable temperature fluorescence data series wherein one (E-type) fluorescence component is unchanged as function of temperature, and another (Y-type) fluorescence component shows considerable temperature dependence (enhanced at low temperature).[135] These low energy species are implicated in quenching of SF.

The time-resolved fluorescence of both TFs and single crystals provides further evidence for the formation of low energy excimers in β-**1**. The ~1.5 and 3-5 ns decay components are dominant in the fluorescence decay of highly β-**1** films and are assigned to prompt fluorescence from S_1 and fluorescence from an excimer state. α-**1** films also contain these decay components

(due to some β-**1** presence in the film) but possess additional decays of less than 0.7 ns and longer than 15 ns, assigned to SF and fluorescence resulting from triplet-triplet annihilation, respectively (Table 3.2). The time-resolved fluorescence data are consistent with ultrafast transient absorption data that suggest the rate of transfer of S_1 population to the excimer state is roughly 10 ps^{-1} in β-**1,** while it is only 0.01 ps^{-1} for α-**1** crystallites.[57]

In bulk crystals a fluorescence rise component of 1.3 ns is found while detecting at 15385 cm^{-1} that matches the decay observed while detecting at 20200 cm^{-1} (Figure 3.11), which is an indication that population exchange between two emissive states occurs, possibly of the E- and Y-type discussed above. The fact that the fluorescence in β-**1** retains some vibronic structure implies that the excimer species may be strongly coupled with the locally-excited (i.e., Frenkel exciton) configuration, which may be the reason for fast population transfer to a state lower than S_1.[57] This type of reasoning has been invoked to explain dual fluorescence in dibenzofuran dimers.[136] In that case unstructured fluorescence arises from excitation below the S_1 threshold, and dual emission arises from excitation of S_1. The situation in crystals of **1** is undoubtedly more complex, including interactions with more than just one nearest neighbor, but the dominant intermolecular species may exhibit behavior similar to that observed in gas phase dimers.

If excimer-like geometries can be achieved without a significant activation barrier then the absorption spectrum and excited state relaxation can be modified. Shifted and broadened absorption due to strong coupling between locally excited and intermolecular species have been found in direct absorption or fluorescence excitation spectra of jet-cooled van der Waals dimers of small acenes.[137] There, calculated excitonic couplings are much smaller than observed spectral shifts, implying the dominance of excited state mixing in determining the absorption spectra. Similar effects are observed in dibenzofuran dimers,[138] in which a similar geometry

between the ground state of the dimer and the excimer facilitates direct absorption into the excimer state that lies below S_1.

There are a number of examples of the preference of certain crystal types to afford even large-scale motions associated with isomerization that results in photodimerization.[139] In most cases, steric hindrance or the presence of void space can be identified as the enabler of more facile motion in one polymorph vs. another.[140] Although large scale motion is probably not necessary to improve the likelihood of excimer formation in films of **1**, subtle differences in interactions between neighboring π-stacks may be responsible. These distinctions in molecular packing may facilitate the preferential formation of excimer-like states, similar to those of perylene,[141,142] in one polymorph but not another. The interactions between stacks in β-**1** are clearly stronger than in α-**1**, which may produce a cooperative effect in stabilizing excimer species.

Ultimately, we ascribe changes in absorption and fluorescence properties of the two polymorphs to a variety of factors, but the lack of high triplet yields in β-**1** is most likely due to competition between SF and facile formation of excimers.[57] Surprisingly, calculations show that excitonic coupling and SF matrix elements are largest between molecules not collocated within slipped π-stacks. Given that the major differences between the α-**1** and β-**1** structures are between and not within such stacks, the distinction in photophysical behavior becomes easier to rationalize.

3.4.3. Connection between Polymorph Structure and Transient Photophysics.

Current theories emphasize the role that π-stacking—particularly slip-stacking—of chromophores plays in optimizing the matrix element for SF.[122,143] The crystalline packing in

both polymorphs leads to very similar π-stacking interactions that form slip-stacked columns. Differences exist in the longer-range order of the crystals; for example, while the unit cells of both α-**1** and β-**1** contain four translationally inequivalent molecules, the unit cell volume of β-**1** is smaller than that of α-**1**. In addition, the interaction geometries between slip-stacked columns are different in the two polymorphs.

The different fates of S_1 despite the very similar "dimer" geometries is something that cannot be explained using existing theories of the role of interchromophore coupling in SF. Rather, it appears that the β polymorph is capable of rapid stable excimer formation that outcompetes SF. The differences in longer range packing may stabilize an excimer-like species in β-**1**, relative to that in α-**1**. Modeling the transient dynamics of α-**1** films (Figure 3.20) showed that rapid trap/excimer formation from higher-lying vibrational levels of S_1 can be an important modifier of Φ_T, and at significantly high temperatures trap/excimer formation can also occur from the thermalized S_1. At high energy excitation trap/excimer formation occurs with k_{trap}^{S1*} = 1-2 ps^{-1}, but is competing with vibrational cooling on the S_1 surface that is much faster, k_{vc} = 13-16 ps^{-1}. If the same k_{vc} rate constants are assumed for β-**1,** formation of the species responsible for the strong stimulated emission feature observed at the t< 200 fs in our transient absorption experiment requires a rate constant comparable to k_{vc}, and leaves k_{EX} (the main competition with k_{sf} in β-**1**) about an order of magnitude larger than k_{trap}^{S1*} (the main competition with k_{sf} in α-**1**).

The longer range crystalline structure appears to also influence the energy of S_1. Modeling of the absorption spectra of a film composed of mostly α-**1** required an H-aggregate model, while the absorption spectra of β-**1** films were modeled with a single vibronic progression. The fits also indicated a 600 cm^{-1}blueshift in the onset of absorption for α-**1** compared to β-**1**, which again must be attributed as arising from the longer range crystalline

structure rather than the geometry of the slip-stacked molecular pairs. The lower S_1 energy in β-**1**should mean that SF is significantly more endergonic than in α-**1**, which is evident in the transient studies presented here.

3.5. Conclusions

3.5.1. Structure and Calculations Explain Differences in Polymorphs

A correlation between two TF polymorphs of **1** has been made with two bulk crystal structures that have been fully characterized. The observation of a red shift and a change in absorption shape after a change in TF morphology has improved our understanding of why the two forms of **1** follow distinct excited state decay pathways. While the SF matrix elements and the Davydov splitting are not strongly modified between the slip-stacked molecules of α-**1** and β-**1** polymorphs, calculations reveal significant interactions between adjacent lattice stacks. The fluorescence quantum yields and lifetimes exhibit a trend that characterizes the transition from SF-dominance in α-**1** to excimer formation and fluorescence dominance in β-**1**. Our data suggest that the distinct behavior is due to longer range differences in molecular packing that facilitate energy loss to low energy states (i.e., excimers, traps) in β-**1** films.

3.5.2. Ultrafast Transient Analysis for Mechanism Determination

The concentrations $[T_1]$ and $[S_1]$ as a function of time were extracted from the ultrafast transient absorption datasets for α-**1** films and were modeled to better understand the SF mechanism in these films. Studies of the fluence dependence of excited state kinetics indicate that the two time scales for triplet formation in α-**1** films arise from i) singlet-singlet annihilation processes to form a S_n state that fissions extremely quickly and ii) a slower fission pathway involving SF from S_1 to $2\times T_1$. A study of the transient kinetics carried out at low fluences, in the

absence of SSA, has provided insight into the role of trapping processes in attenuating Φ_T. A "hot" trapping process is active for excitations well above the absorption onset, while trapping from the thermalized S_1 is important at temperatures above 180 K, consistent with an activation barrier for this process. k_{sf} rates are essentially temperature-independent.

3.5.3. Perspective on Performance and Dynamics

UV-vis absorption and triplet action spectra indicate that SF is significantly slower than competing processes from the thermalized S_1 level of β-**1** crystallites, but a small triplet yield is attained at higher energy excitations. Time-resolved spectroscopy and fluorescence measurements show that the singlet state quickly formed in β-**1** possesses excimer character and decays mostly radiatively. Φ_T values of α-**1** and β-**1** at room temperature were about 1.6 and 0.1, respectively. The diverse behavior observed in films composed of just one type of SF molecule underscore the defining role that even longer-range molecular ordering plays in determining the efficiency of SF. Many parallels can be drawn between this system and Tc, in that both materials exhibit polymorphism and have near-perfect triplet yields.

4. Polymorphism Influences Singlet Fission Rates in Tetracene Thin Films

4.1. Introduction

Tc, a widely investigated system, has been studied experimentally and theoretically for close to a century, and new information is continually uncovered as the breadth of understanding increases. Unlike **1**, Tc is quite stable and both of its polymorphs undergo efficient SF. In this chapter, we present results on the effects of crystal polymorph and crystallite size on the rate of SF in polycrystalline Tc TFs. We deposited films of two polymorphs of Tc[144-146], Tc I and Tc II, and varied the crystallite size for each one. Using ultrafast transient absorption spectroscopy, we show that Tc II films exhibit faster SF than the more commonly deposited and studied Tc I films. In addition, consistent with the results of Piland et al.,[37] we found that for Tc I, smaller crystallites lead to significantly faster SF. However, Tc II films exhibit a drastically reduced dependence on crystallite size. Examination of the crystal structures of the two polymorphs leads to some rationale for the distinct behavior, but calculation of electronic couplings between pairs of molecules does not reproduce the experimental trend.

4.2. Experimental

4.2.1. Materials

Tc (Benz[b]anthracene, 98%, CAS # 92-24-0) was purchased from Aldrich and used without further purification. Glass cover slips were washed with hexane and acetone, plasma cleaned, and kept in a glovebox before depositions.

4.2.2. Film Deposition

Deposition rate and substrate temperature were varied during depositions from 0.5 – 5.0 Å/s and 85 – 340 K, depending on the desired film type and crystallite size. Depending on the desired film type and crystallite size, deposition rate and substrate temperature were varied from 0.5 – 5.0 Å/s and 85 – 340K. The temperature of the crucible housed in the Radak source typically ranged from 185 – 210°C, depending on the desired deposition rate. Prior to transient measurements, films were sealed with Surlyn as described previously.

4.3. Results and Discussion

4.3.1. Film Structural Characterization

Polycrystalline Tc TFs were prepared by thermal evaporation onto microscope cover slips. Substrates at room temperature or heated to 65°C produced predominantly Tc I films while substrates cooled to liquid nitrogen temperature (-180°C) yielded predominantly Tc II films. XRD allows for a simple differentiation between film types (Figure4.1a). The peaks at 7.3° and 6.9° are assigned to Tc I and Tc II, respectively.[146] By fitting to two peak functions and extracting the peak areas, we generally measured ~10:1 and 1:10 polymorph ratios under optimized conditions (Figure4.1a), thus generating films of highly Tc I and others of highly Tc II content, although there is a thickness dependence for the ratio of Tc II:Tc I during cold depositions (thicker films favor more enrichment of Tc I character).

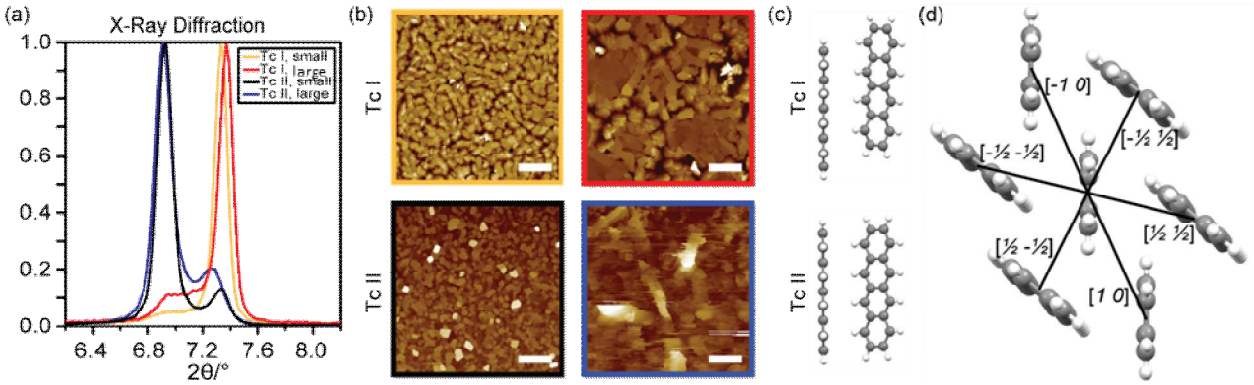

Figure 4.1

(a) XRD showing the (001) peak for the four film types. (b) AFM images of Tc I (top) and Tc II (bottom) films, with small (left) and large (right) crystallites. Scale bars = 2 µm. (c) Orientation of the dimers in the *ab*-plane corresponding to an [*a b*] translation vector of [½ ½] in Tc I (top) and Tc II (bottom). (d) View of the herringbone structure in the *ab*-plane. Centroid molecule distances between the center molecule and the nearest-neighbors are Tc I [*1 0*] = 6.056 Å, [-½½] = 4.773 Å, and [½ ½] = 5.125 Å; Tc II [*10*] = 5.909 Å, [-½ ½] = 4.711 Å, and [½½] = 4.787 Å.

Heated substrates generally induced purer Tc I films compared with room temperature substrates. In addition, Tc II films transform into Tc I films over a few weeks to months, although this could be dramatically slowed by storage below room temperature. Only samples with verified polymorph purity ≥90% were used in the optical experiments. By varying the deposition rate, considerable control of crystallite grain size was achieved (Figure 4.1b). Fast deposition rates near 5.0 Å/s yielded crystallites measured with atomic force microscopy (AFM) to be 100 - 200 nm, whereas slower deposition rates, 0.5-1.0 Å/s, produced much larger micron-sized crystallites. We chose four film types to investigate the complementary effects of crystal structure and film crystallinity (see Figure4.1b) on optical properties and SF dynamics.

Tc molecules deposit with the long axis nearly perpendicular to the substrate plane, causing the crystal *ab*-plane to be parallel to the surface and the c-axis to point towards the normal. Polycrystalline domains are isotropically distributed around the normal, leaving only the (00*c*) peaks observable in XRD. Inspection of the crystal structures of Tc I and Tc II

(Figures4.2a, b) reveals tighter packing in the *c*-axis direction in Tc I than Tc II, leading to the higher angles for the (001), (002), and (003) peaks for Tc I. Figure4.3 also shows the XRD patterns calculated from the crystal structures. The Tc I crystal structure was determined experimentally in the past and was available on the CCDC, while Tc II was calculated by Schatschneider after extrapolation from the Tc II single crystal under high pressure.[146]

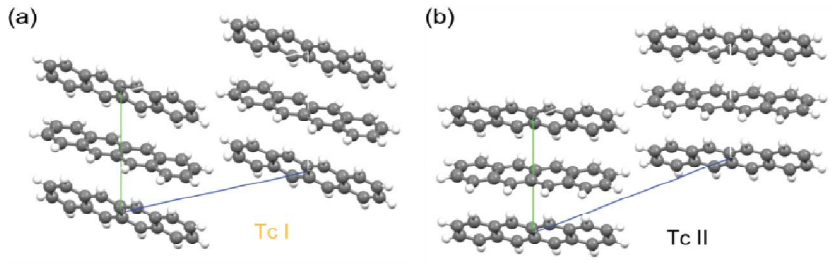

Figure 4.2

(a) Tc I crystal structure looking down the a-axis with the c-axis left to right. (b) Tc II crystal structure.

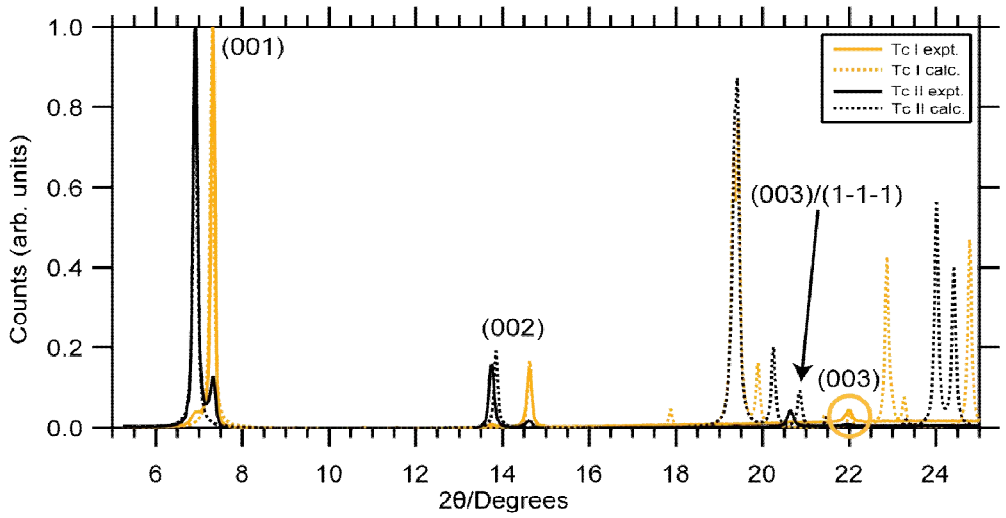

Figure 4.3

Comparison of experimental and calculated diffraction pattern for Tc I and Tc II. The (003) peak for Tc I is circled. The calculated (003) and (1-1-1) peaks for Tc II are strongly overlapped and merge into a single peak with a realistic linewidth of 0.1°-0.2°.

4.3.2. Absorption and Fluorescence

The absorption and fluorescence spectra of the four films are shown in Figure4.4a. All four films exhibit the characteristic Davydov splitting and vibrational progression of polycrystalline Tc in the absorption spectrum; with the two polymorphs having different peak ratios between the Davydov peaks (the higher energy split Davydov peak is much larger in Tc I). However, a simple correlation between absorption and film type, employed in other SF systems,[33] is complicated by film birefringence, which leads to thickness dependent vibronic peak ratios.[147] The fluorescence spectra are qualitatively similar, with both films exhibiting a vibronic progression of peaks and red-shifted feature previously assigned to defects or excimers.[37] However, the amplitude of this feature is greater in Tc II films compared to Tc I films. Time correlated single photon counting (TCSPC) with 395 nm excitation revealed multiexponential singlet decay kinetics (Figure4.4b) that differed primarily in the initial fast decay component, commonly assigned to SF dynamics. Fitting using a series of three exponentials convolved with the instrument response gave fastest time constants of 85 (Tc I large), 65 (Tc I small), 40 (Tc II large), and 50 ps (Tc II small).

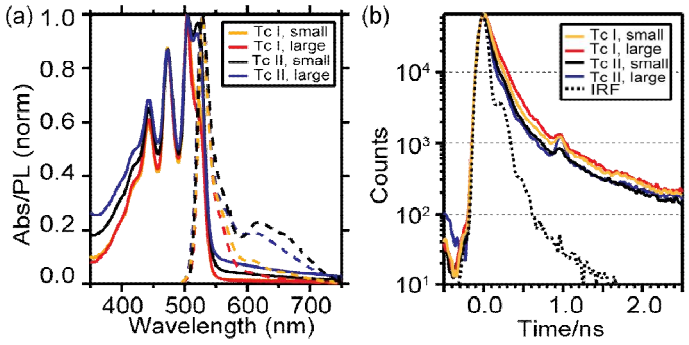

Figure 4.4

(a) 80 nm thick film absorption (solid) and emission (dashed) spectra. (b) Time-resolved emission traces. The Tc II, large film was 20 nm thick. We observed no thickness dependence to SF dynamics.

4.3.3. Ultrafast Transient Absorption

We used ultrafast transient absorption spectroscopy with 400 nm excitation and ~250 fs time resolution to investigate directly both the singlet and triplet dynamics with a higher time resolution and a larger range of excitation densities than is available with TCSPC. Figure4.5a shows the transient spectra at ~1 ps delay for the Tc I large crystallite film and Tc II large crystallite film at moderate excitation densities of ~55 x 10^{17} cm^{-3}. While there is very little spectral difference between films, a combination of spectral fitting and singular value decomposition (SVD) elucidated differences in SF dynamics. At low pump fluences, two main SVD principal components were found; one "singlet-like" and one "triplet-like". Spectral fitting was also performed by treating each transient spectrum as a linear combination of singlet and triplet spectra. The singlet spectrum was chosen as the 1 ps spectrum, as an insignificant concentration of triplets would be formed at this time delay. As the SF time constant is around 100 ps in Tc,[37] we used the ~5 ns spectrum as the triplet spectrum (Figure4.5b). Using these two spectra we fitted each transient spectrum to extract singlet and triplet kinetics (Figure 4.5c). We fitted the curves with a kinetic model including ground, singlet, correlated triplet pair ^{1}(TT), and triplet states, with SF, exciton annihilation, and spontaneous relaxation channels for each state (Figure4.6). The kinetic model required the inclusion of the ^{1}(TT) state that could return population to the singlet in order to properly account for the apparent slowing of the singlet decay at long times >100 ps (Figure 4.5d). Tc I films with large crystallites have a SF time of ~120 ps, which significantly decreases to ~35 ps as the crystallite grain size is decreased. Tc II films, however, have significantly faster SF times that do not show a strong dependence on crystallite grain size, with a SF time ~20-35 ps for both large and small crystallites.

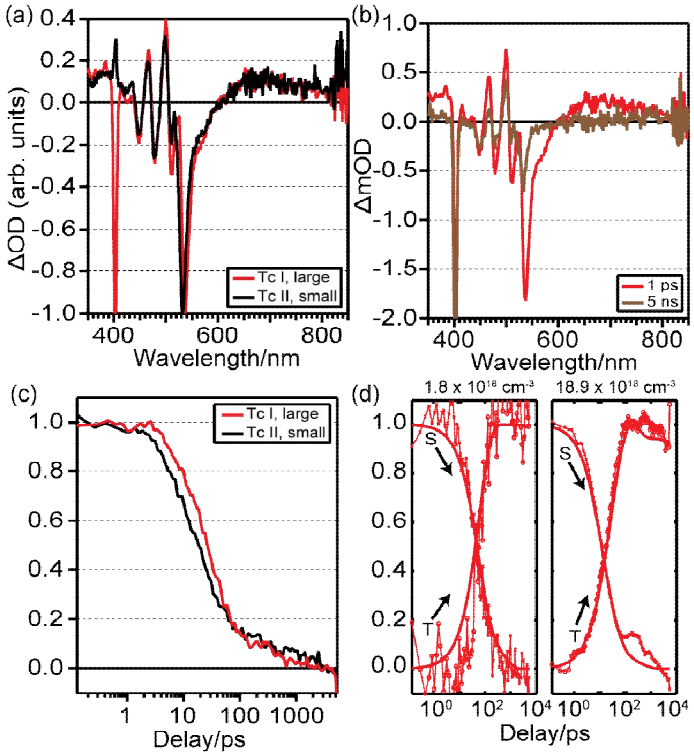

Figure 4.5

(a) Comparison of Tc I, large and Tc II, small film transient spectra at 1 ps delay and ~55x10^{17} cm^{-3} excitation density. The 400 nm feature is due to pump scatter. (b) Tc I, large crystallite film transient spectra at 1 ps and 5 ns. (c) Comparison of deconvolved singlet-triplet dynamics. (d) Tc I, large crystallite film deconvolved singlet-triplet dynamics with kinetic fit (expt. = dots, fit = lines) for low and high excitation densities. The feature at times greater than 100 ps in the high excitation density trace is assigned to an acoustic mode, not captured by the fit.

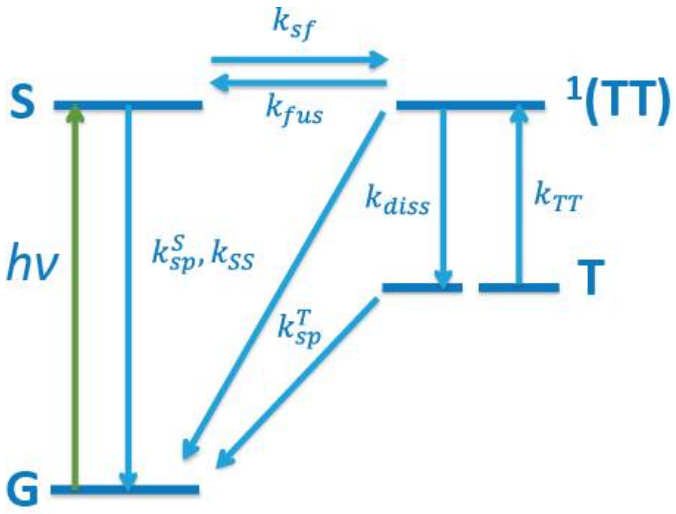

Figure 4.6

Kinetic model used for fitting extracted singlet-triplet dynamics. Included are the ground state (G), singlet state (S), coupled triplet state (^{1}(TT)), and uncoupled triplet state (T); and rate parameters for SF (k_{sf}), triplet fusion (k_{fus}), triplet dissociation (k_{diss}), spontaneous relaxation (k_{sp}), and exciton annihilation (k_{ss}/k_{TT}).

Figure4.7 shows exponential decay time constants extracted using a global fit as a function of fluence for the two principal SVD components. Increasing pump fluence leads to faster decay times, indicative of exciton-exciton annihilation.[52] At low fluences, the trend in decay times from SVD is consistent with the trend in SF rates extracted from the kinetic modeling: Tc I films with large crystallites have the slowest SF rate, which speeds up considerably with small crystallites. The Tc II films have the same SF rate within experimental reproducibility regardless of crystallite grain size, which is faster than either of the Tc I films.

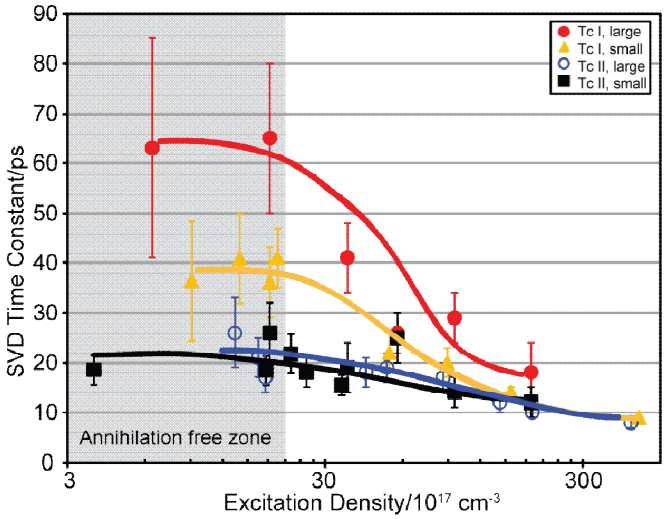

Figure 4.7

Time constants associated with SF from global fit of SVD data for all four film types from low to high fluence. Lines are guide to the eye.

Using the absorption coefficients and measuring the energy of the pump focused through a series of pinholes, we calculated excitation densities from 10^{17} – 10^{19} /cm^{-3}. At higher fluences, SVD revealed an additional principal component with a small singular value that we ascribe to an acoustic mode caused by sample heating; we subtracted off this mode before the spectral fitting procedure and kinetic modeling, as those methods do not include an acoustic mode. Figure4.8presents a comparison of the two lowest fluence data, demonstrating the kinetics are fluence-independent.

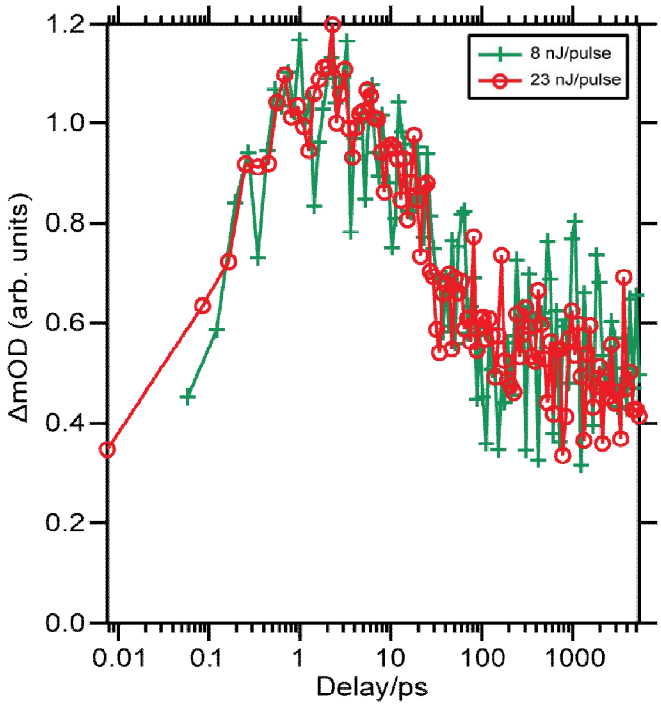

Figure 4.8
Single wavelength slices at 535 nm for Tc I, large crystallite films at two fluences, demonstrating fluence-independent kinetics.

Ultrafast Systems LLC Surface Explorer 4.0 Software Package was used for background and scatter subtraction, chirp correction, singular value decomposition (SVD), and global fitting of the principal components from SVD. At low fluences, SVD revealed two principal components, one decaying and the other rising, consistent with singlet and triplet states. The other components all represent experimental noise (Figure4.9a). At higher fluences, a ~1 ns oscillatory feature with a small singular value emerged, becoming clearer at the highest fluences (Figure 4.9b); we associated this component with an acoustic mode caused by sample heating. Global fitting of the two principal components to a decaying exponential and an offset gave good fits of the kinetics (Figure 4.9c). We associated the decay with a singlet-like component and the offset with a triplet-like component, although assigning the features directly is difficult because SVD requires no physical input, but is a purely mathematical procedure. Figure 4.10

depictsglobal fit decay constants for 80 nm and 40 nm thick films of Tc I and II, demonstrating the kinetics are not dependent on film thickness.

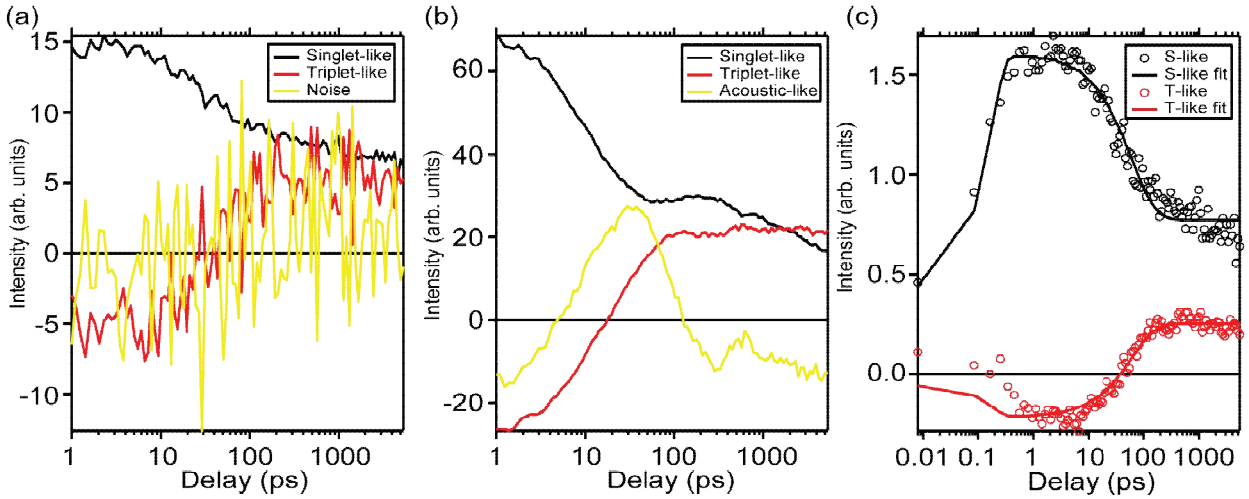

Figure 4.9

(a) Low fluence (1.83 x 10^{18} cm^{-3}) SVD. (b) High fluence (18.9 x 10^{18} cm^{-3}) SVD, with three components. (c) Global fit with a single exponential (61 ps) and offset (1.83 x 10^{18} cm^{-3}).

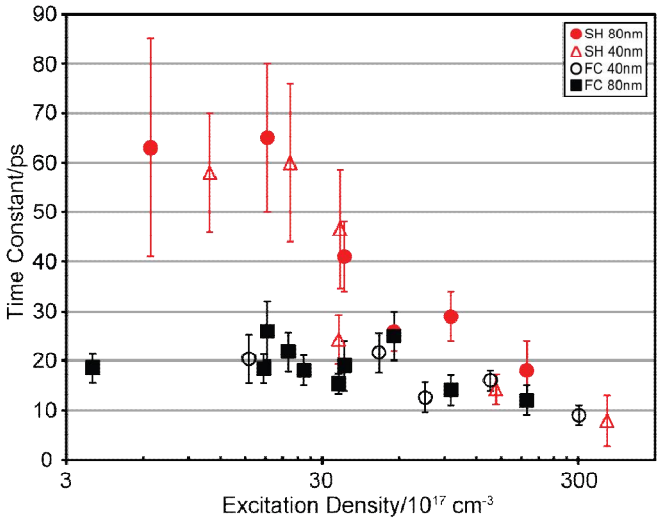

Figure 4.10

Global fit parameters for 80 nm and 40 nm thick films, demonstrating lack of thickness dependence.

Before further spectral and kinetic fitting was performed in Matlab, the oscillatory mode was subtracted from the data. An early time (~1 ps delay) and a late time (~5 ns delay) transient spectrum from the corrected dataset were assigned to represent singlet and triplet states, respectively. From this spectral fitting, amplitudes of singlet and triplet components as a function of time were extracted. This procedure strictly extracts kinetic traces without an absolute magnitude. It is difficult to deconvolute excited state absorption, ground state bleach, and stimulated emission in Tc because these features are broad and overlapping, making it difficult to apply a magnitude, i.e. extinction coefficient, to the kinetic traces and to extract a triplet yield. The resulting kinetic curves were globally fitted to the model in Figure4.6 to extract rate constants for singlet and triplet decays, SF, triplet fusion, triplet dissociation, and singlet exciton annihilation, similar to Wilson et al.[148] The extracted kinetics and fits for all four films are shown in Figure4.11 and the rates are tabulated in Table 4.1. While the model allows for triplet-triplet annihilation, this rate was relatively unconstrained and tended towards the lower bound for the fit. Thus, we set this parameter to zero. Overall, Dylan Arias and his data analysis capabilities were invaluable in teasing out the subtle differences in dynamics observed and presented above.

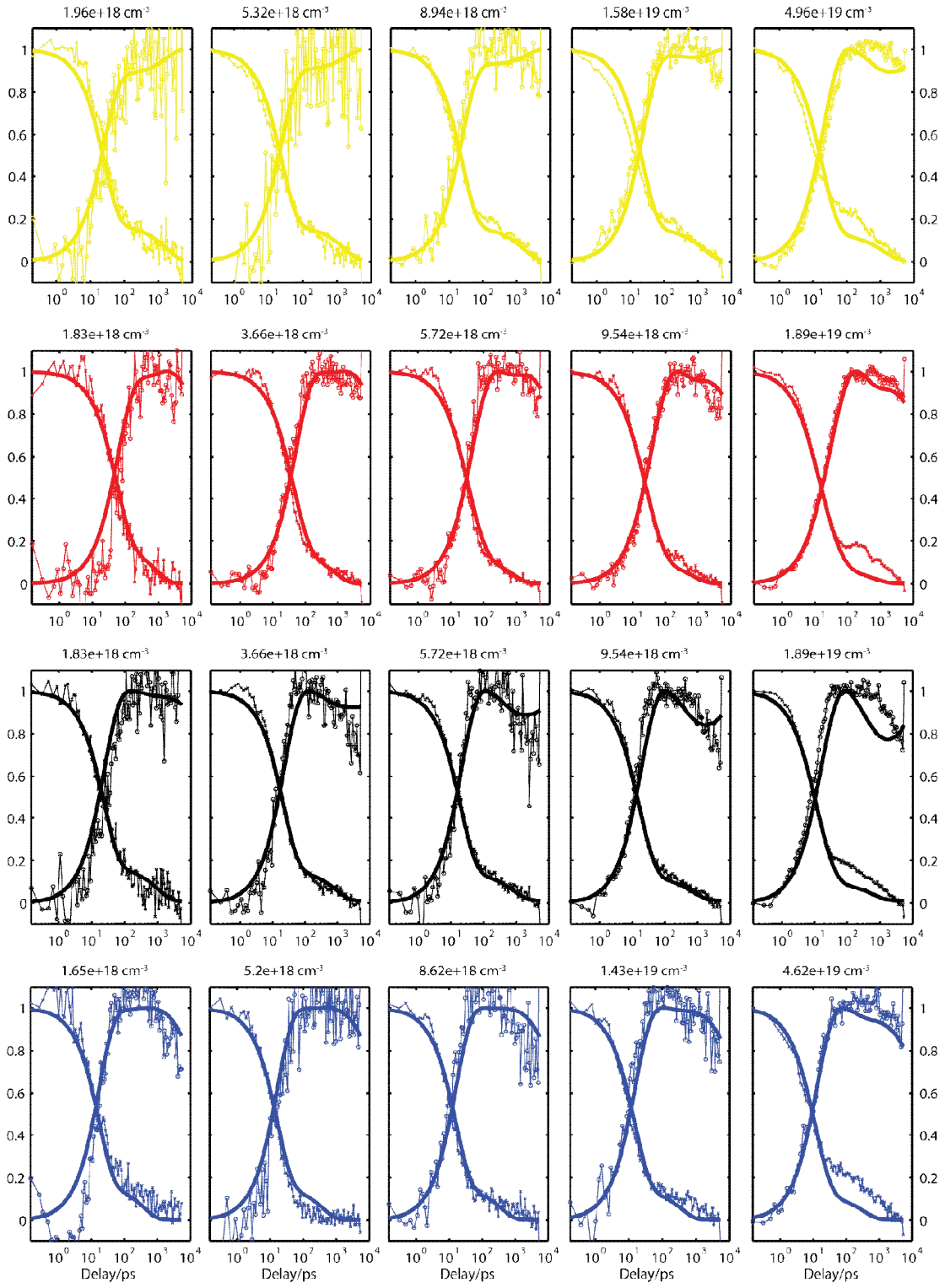

Figure 4.11

All extracted singlet and triplet dynamics and their fits.

Table 4.1

Extracted kinetic parameters for all four films.

	$1/k_{S,sp}$[ps]	$1/k_{sf}$ [ps]	k_{SS} [10^{-21}cm^3/ps]	$1/k_{T,sp}$ [ps]	$1/k_{fus}$ [ps]	$1/k_{diss}$ [ps]	k_{TT} [cm^3/ps]
Tc I, large	524	124	3.62	21,586	360	439	0
Tc I, small	12,500	35	0.56	1 µs	219	1,559	0
Tc II, small	500	36	3.86	31,814	99	268	0
Tc II, large	507	22	0.82	32,267	113	365	0

4.3.4. Dimer Electronic Coupling

Coupling calculations were performed by Niels Damrauer and were similar to those presented in a recent study on tetracene dimers.[68] Figure4.1d shows the relevant dimer pairs in the *ab*-plane associated with any given Tc chromophore for Tc I or II. We assumed the so-called mediated mechanism of SF and utilized one-electron orbital coupling matrix elements, t_{ab}, of these dimer pairs to calculate the diabatic couplings, V, between a singlet exciton state (S_1S_0 or S_0S_1) and the SF product state written as a singlet-coupled pair of triplets, ^{1}TT (Equations4.1 and 4.2).[68]

In Equations 4.1 and 4.2 H = HOMO, L = LUMO, and ΔE_{CT} is the energy difference between S_1 and the virtual intermediate CT state. Using ΔE_{CT} = 600 meV, estimated from electroabsorption,[149] the couplings are summarized in Table 4.2. The largest couplings in both Tc I and Tc II are for the [½ ½] dimer. As depicted in Figure4.1c, Tc I has a substantial slip along the major axis of the molecules whereas this slip is absent in Tc II. This geometric asymmetry causes asymmetry between the electron- and hole-transfer pathways contributing to the coupling so they do not cancel when subtracting. In contrast, geometric symmetry in the Tc II [½ ½]

dimer leads to more closely matched contributions from electron-and hole-transfer pathways, leading to a smaller overall value for the SF coupling. This result highlights the need to account for molecular orientation in addition to the molecular distances.

$$V_{(S_1S_0 \rightarrow {}^1TT)} \approx \frac{\sqrt{3/2}|t_{LH}t_{LL} - t_{HL}t_{HH}|}{\Delta E_{CT}} \qquad (4.1)$$

$$V_{(S_0S_1 \rightarrow {}^1TT)} \approx \frac{\sqrt{3/2}|t_{HL}t_{LL} - t_{LH}t_{HH}|}{\Delta E_{CT}} \qquad (4.2)$$

Table 4.2

Calculated Diabatic Couplings (meV) for SF. Largest SF couplings are highlighted in bold.

	Tc I [-½ ½]	Tc II [-½ ½]	Tc I [½ ½]	Tc II [½ ½]	Tc I [1 0]	Tc II [1 0]
$V_{(S_1S_0 \rightarrow {}^1TT)}$	4.5	3.4	0.6	8.5	0.05	1.4
$V_{(S_0S_1 \rightarrow {}^1TT)}$	7.2	6.2	16	1.8	0.05	1.4

4.4. Conclusions

In summary, we fabricated polycrystalline Tc TFs of two polymorphs with varying crystallite sizes. Using ultrafast transient absorption spectroscopy, we discovered that SF is significantly faster in polymorph Tc II than in Tc I, and that, unlike in Tc I films, in Tc II films the crystallite size has little or no effect on the SF rate. These results highlight the importance of polymorphism and morphology for SF in Tc, and most likely for many organic semiconductors in which exciton delocalization, migration, and fission simultaneously influence excited state dynamics. Contrary to spectroscopic results, calculations of the coupling terms between various dimer pairs suggests that Tc I should undergo SF faster than Tc II, when in fact this is not the case. This prompts the need for more rigorous, many-molecule calculations that elucidate the behavior of excitons as a function of time, tracking delocalization, charge/energy transfer,

vibrational modes, phonon modes, and other electronic, mechanical, and collective effects, some of which can only be accounted for with a larger cross-section of crystal. The simple analysis of an individual pair of dimers is simply insufficient to account for these various effects that inevitably influence dynamics and coupling. Tc remains a relevant and well-known system, although much more work can be done regarding this versatile chromophore. In addition, however, a wider, more diverse range of chromophores must be sought out in order to expand upon the depth of understanding of SF and enable guided and targeted compound engineering.

5. Structural and Photophysical Characterization of Indigo-based Derivatives for Singlet Fission

5.1. Introduction

This chapter focuses on solutions and TFs of Cibalackrot, (7,14-diphenyl-diindolo[3,2,1-de;3',2',1'-ij][1,5]naphthyridine-6,13-dione,(**2**), a material previously demonstrated to have energy levels appropriate for efficient SF[69,150,151], and a recently synthesized t-butyl substituted derivative, 1,8-Bis(3,5-di-*tert*-butylphenyl)diindolo[3,2,1-*de*:3',2',1'-*ij*][1,5]naphthyridine-2,9-dione, (**3**). These versatile, attractive indigo-based chromophores are biradicaloids that have the desirable properties of extremely high photostability and excellent charge transport properties.[69] Solutions of these molecules are highly fluorescent, with yields around 80%,[151] and lifetimes of about 5 ns. If proper intermolecular interactions could be engendered in films or other aggregates, in principle the SF rate could be tuned to out-compete fluorescence. The result would be a thin molecular layer that produces a 200% quantum yield of triplets upon photoexcitation in the blue/green solar spectrum. Due to its fast and ambipolar transport of charge carriers, such a layer could be a versatile partner in quasi-tandem schemes in which SF enhances a high-performing single-junction solar cell.

Prior studies of **2** have shown that fluorescence quantum yields, Φ_F, are quite high in solution (0.76 in dioxane).[151] It has also been shown through electrochemical, cyclic voltammetry (CV) measurements that the CV band gap is about 2.5 eV, compared to an optically measured band gap of 2.0 – 2.1 eV.[150] Singlet (2.136×10^4 $M^{-1}cm^{-1}$) and triplet (3.410×10^4 $M^{-1}cm^{-1}$) molar extinction coefficients, internal conversion quantum yield (Φ_{IC}, 0.13), and fluorescence lifetime (τ_F, 6.10 ns) have also been reported.[151] Disparate from the vast and diverse work surrounding Tc, and the modest number of studies regarding **1**, **2**has only been analyzed in

a limited capacity. Until now, **2** has not been investigated with respect to SF, and very limited electrochemical and photophysical work has focused on TFs.Our approach to evaluation of **2** includes a combination of TF engineering, electronic structure calculations, and spectroscopic characterization, similar to prior studies of **1** and Tc.[33,57,78]

5.2. Experimental

5.2.1. Materials

Reagent grade benzene, toluene, and tetrahydrofuran (THF) were purchased from Aldrich and used without further purification. The solvents were degassed by bubbling argon through them for 30 minutes, and the solutions were kept free of water and oxygen thereafter. Cetyltrimethylammonium bromide (CTAB, ≥99%) was purchased from Sigma-Aldrich. Glass substrates (Fisher) were cleaned with acetone and hexane and exposed to O_2 plasma for 5 minutes.

5.2.2. Calculations

Calculations of singlet transition moments of **2** were carried out using the NWChem TDDFT Module.[152]**2** triplet-triplet excitations were conducted utilizing the RI-MP2/TZVPP (Turbomol) geometry of 3 Au state in the TDDFT CAM-B3LYP/6-31++G Gaussian in a ground to excited state transition electric dipole moment (Au) analysis. These calculations, and others regarding SF matrix elements and Davydov splitting computations currently underway, are attributed to the Michl group (Michl, Havlas, Wahab, and Ludvík).

5.2.3. Synthesis

All reactions were carried out under argon atmosphere with dry solvents freshly distilled under anhydrous conditions, unless otherwise noted. Synthesis of the following compounds was

carried out by Paul Dron in the Michl Group in Boulder. Standard Schlenk and vacuum line techniques were employed for all manipulations of air- or moisture-sensitive compounds. Yields refer to isolated, chromatographically and spectroscopically homogenous materials, unless otherwise stated.2-(3,5-Di-*tert*-butylphenyl)acetyl chloride[153,154] was synthesized according to a previously published procedure. Xylenes were dried over sodium and distilled under argon prior to use. All other reagents were used as supplied unless otherwise stated.

2has been synthesized according to a previously published procedure.[151] The synthesis of **3** was carried out by adding a solution of freshly distilled 2-(3,5-di-*tert*-butylphenyl)acetyl chloride (1.752 g, 6.566 mmol) in dry xylenes (5 mL) dropwise to the refluxing solution/suspension of indigo (393 mg, 1.500 mmol) in dry xylenes (25 mL) over a period of 30 min. The resulting dark blue/purple reaction mixture was refluxed in an oil bath at 170 °C for an additional 6 h and then stirred for 16 h at 140 °C. The reaction mixture turned red during this time. The vessel was allowed to return to room temperature and volatiles were removed under reduced pressure. The dark red honey-like residue was carefully triturated with hexane (5 × 5 mL), and then purified by column chromatography on silica gel (hexane:CH_2Cl_2, 1:4). The crude product was finally triturated with hexane (5 × 1 mL) once again. **3**was obtained as a deeply red crystalline material (101 mg, 0.147 mmol, 10%). Preparations of **2**and **3** are outlined in Figure 5.1.

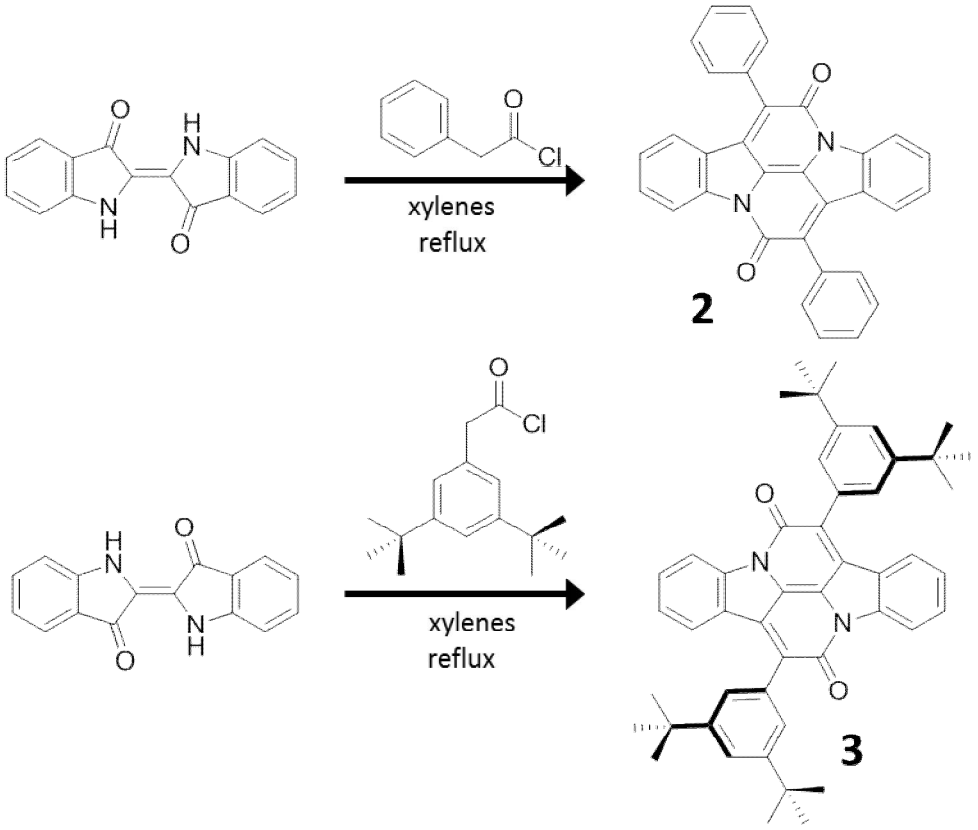

Figure 5.1

Synthesis of **2** (top) and **3** (bottom)

5.2.4. Electrochemistry and Transport

Electrochemical current-voltage scans were conducted against a Ag/AgCl reference, with a Pt counter electrode, in a CH_3CN 0.1 M $TBAPF_6$ electrolyte. The data match very closely with previously published results, and no further analysis or experimentation was performed.[150]

5.2.5. Single Crystal Growth and Characterization

Single crystals suitable for X-ray diffraction (XRD) were grown by sublimation at 250 °C in a stream of dry nitrogen (5 L/min flow rate). A bulk **2α** crystal was characterized by XRD single-crystal structure analysis on a Bruker Smart X2S diffractometer operating with MoKα radiation (λ = 0.71073 Å). The structures were solved by Direct Methods, SHELXS-97[155] and

refined by full-matrix least-squares on F^2, SHELXL-97.[95] The H atoms were calculated geometrically and a riding model was applied during the refinement process. Single crystals of **2β** and **3α** were selected and mounted on Mitegen loops in Paratone oil and data were collected on beamline 11.3.1 at the Advanced Light Source with λ= 0.7749Å. Data for **2β** were collected on a Bruker D8 diffractometer with an APEXII CCD detector. Crystallographic data for 3α were collected on Nonius Kappa CCD diffractometer equipped with Bruker APEX-II CCD detector by monochromatized MoKα radiation (λ = 0.71073 Å) at a temperature of 150 K. The structures were solved by direct methods (SHELXS)[95] and refined by full matrix least squares based on F^2 (SHELXL97).[154]Bulk crystal growth and characterization was performed by various contributors including Stepp, Dron, Teat, Głowacki, Irimia-Vladu, and Monkowius.

5.2.6. Thin Film Preparation

During thermal evaporation, substrate temperature varied from 80 – 473 K and deposition rates typically ranged from 0.5 – 5.0 Å/s. The temperature of vaporization was 240 – 275 K, depending on desired rate, and film thicknesses varied from 50 – 250 nm. Deposition rate and total thickness were measured by an Inficon quartz crystal microbalance. Solution drop casting this material was not explored comprehensively, because the solubility of **2** is very low. Initial attempts led to poor quality, non-continuous films that were unsuitable for optical measurements, and therefore, the study herein focuses on thermally evaporated TFs. Annealing was performed on a hot plate at 250 °C for 5 – 60 min depending on film thickness and preferred degree of annealing, although most measurements were performed on as-prepared films.

5.2.7. Nanoparticle Synthesis

Nanoparticles (NPs) of **1** were synthesized analogous to methods outlined in previous work.[28,156-158] In brief, the reprecipitation method was utilized by first preparing a 100 μM

solution of **1** in tetrahydrofuran (THF). About 200 μL of this **1** THF solution was rapidly injected into a vigorously stirring aqueous solution of CTAB (100 μM). The mixture was allowed to stir for 30 minutes and appeared pale pink in color. This NP suspension was concentrated in a rotary evaporator to concentrate the sample to optical densities suitable for optical measurements. Before measurements took place, the sample was filtered through a 200 nm pore size Whatman PVDF GD/X sterile Filter to remove large particles. CTAB, a widely used surfactant, was essential in maintaining small NP sizes during reprecipitation.[159,160]

5.2.8. Transient Absorption

In general, low fluence excitation was used to avoid singlet-singlet annihilation, multi-photon absorption, and other effects that result from using high fluence excitation.[52]

TF fluorescence and transient absorption spectra were collected at various temperatures. The elevated temperature (295 – 500 K) transient absorption was performed on a highly annealed **2α** type film to maintain morphology, as heating induces interconversion to the **α** polymorph. The 77 – 295 K transient absorption was performed on **2α**, **2β**, and **2a** films.

5.3. Results

5.3.1. Calculations

Transition dipole moments were calculated and the transitions with the highest oscillator strengths appear in Figure 5.2. The arrows, scaled with oscillator strength, mostly lie within the plane of the core of molecule. These dipole alignments are taken into consideration in subsequent analysis.

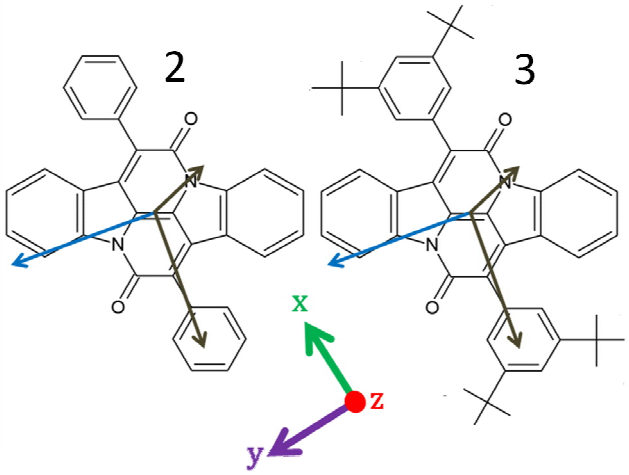

Figure 5.2

Molecular structure of **2** (left) and **3** (right) with relevant singlet (blue) and triplet (charcoal) dipole orientations.

5.3.2. Polymorphs and Thin Film Preparation

Crystals grown from sublimation yielded two polymorphs which could be identified by visual inspection. The main constituent, **2α,** consisted of long, band-like, highly brittle crystals that split into multiple fibrous strings upon mechanical stress. The minority crystal growth species, **2β**, were prism-shaped, and broke into well shaped crystals without disintegrating into numerous pieces. Bulk crystals of **2** were grown from solution and two polymorphs of **2**, monoclinic $P2_1/n$ (**2α**) and monoclinic $P2_1/c$ (**2β**), have been discovered and characterized. Bulk crystals of **3** were grown and characterized, and determined to be triclinic with a P1 space group (**3α**).

TFs of **2** prepared by thermal evaporation were of **2α**, **2β**, and amorphous (**2a**) character. Unit cell parameters are outlined in Table 5.1. Significant morphological growth control was achieved by varying substrate temperature and deposition rate. Thermal evaporation utilizing a deposition rate of 0.5 Å/s onto substrates cooled to 80 K yields **2β** films, whereas evaporation

using a deposition rate of 0.5 Å/s onto substrates that are heated to 473 K yields films that are predominantly **2α**. Furthermore, depositing**2** onto room temperature substrates at a rate of 10 Å/s yielded **2a** films, until a certain thickness was achieved (> 100 nm), at which point **2β** begins to grow. In addition to deposition onto a cold substrate, 1β films can also be grown by fast, thick deposition onto room temperature substrates. Changes in morphological growth occurring beyond a certain thickness threshold have also been observed in the recent study on **1**.[33] Although the XRD patterns are sparse, it is apparent that the two crystalline TF polymorphs match the bulk forms of **2**, as seen in Figure 5.3. The **2α** films have diffractions at 2θ angles of 7.5, 10.2, and 14.1° corresponding to the (002), (10-1), and (111) diffraction planes, respectively. The **2β** films show a characteristic diffraction at a 2θ angle of 10.0 ° from the (011) plane, and lacks strong intensity peaks around 7 and 14 °, although there are small peaks present suggesting some portion of the film has **2β** content. The **2a** films give no X-ray diffraction peaks,and the relevant data are displayed in Figure 5.4a. As-deposited **3a** films show no diffraction peaks, but upon annealing these **3a** films, crystallinity is achieved, with a diffraction peak appearing around 5° corresponding to the (002) diffraction plane, as seen in Figure 5.4b.

Table 5.1

Crystallographic parameters for single crystals of **2α**, **2β**, and **3α.**

Parameter	2α	2β	3α
Structure	Monoclinic	Monoclinic	Triclinic
Space Group	$P2_1/n$	$P2_1/c$	P1
a / Å	8.9	6.2	5.7
b / Å	10.2	10.4	9.0
c / Å	23.8	16.9	18.2
α / °	90	90	78.3
β / °	97.5	97.4	87.8
γ / °	90	90	88.6
Vol. / $Å^3$	2159	1086	915

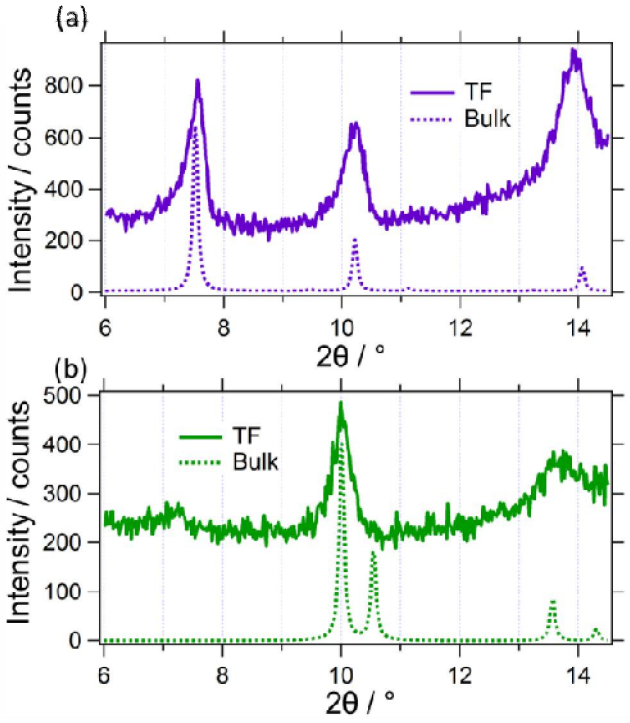

Figure 5.3

(a) **2α** and (b) **2β** TF vs. bulk XRD patterns.

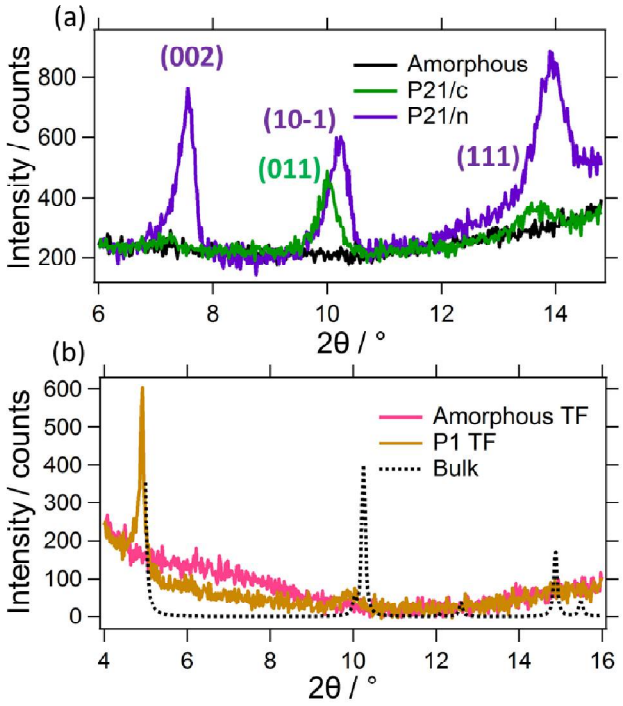

Figure 5.4
(a) XRD diffraction patterns of **2α**, **2β**, and **2a** TFs and corresponding diffraction planes and (b) XRD diffraction patterns of **3a**, **3α**, and bulk **3**.

Upon annealing, either slowly at room temperature in air or rapidly on a hot plate, **2β** and **2a** films interconvert to the **2α** form, which appears to be the thermodynamically stable polymorph. Exposing **2β** and **2a** to solvent vapors also induces annealing and reorganization to **2α**. The nomenclature by no means asserts that the films are purely of one polymorph or purely amorphous, however. For instance **2α** films probably have some **2a** character as well, because the XRD peak intensity increases upon annealing. Moreover, it is likely that all of these films are a mix of two or even three phases. This will be explored in greater detail below.

Molecules in **2β** have the largest intermolecular distance between closest slip-stacked molecular pairs, (6.24 Å) whereas **3α** (5.70 Å) and **2α** (4.71 and 5.52 Å) are significantly smaller, as depicted in Figure 5.5. Likewise, **2β** molecules have the largest slip distance (5.23

Å), while **3α** (4.53 Å) and **2α** (3.28 and 4.23 Å) slip distances are somewhat smaller. Slip directions are generally observed along the long axis of the molecular core, d_L, although **2β** molecules possess a minor component of slip along the short axis of the molecular core, d_S (**2α**: d_L = 3.3 and 4.2 Å, d_s = -.05 and 0.1 Å; **2β**: d_L = 5.1 Å, d_S = 1.3 Å; **3α**: d_L = 4.53, d_S = 0.2). The interplanar spacing is slightly larger in **3α** than in **2α** and **2β**, but the centroid to centroid distances do not share that attribute. Although the geometries and space groups were altered considerably and the interplanar spacing of **3α** is slightly increased, the t-butyl groups on **3** did not significantly increase the nearest neighbor intermolecular distance. Unit cell volumes are also quite different, with **2α** being the largest at 2159 $Å^3$, whereas **2β** and **3α** have unit cell volumes of 1086 and 915 $Å^3$, respectively. The phenyl groups on **2α** polymorph are twisted in a disrotatory manner and are tilted by about 54.7 ° with respect to the molecular plane, whereas those of **2β** are coplanar, or conrotatory, and are tilted by 52.9 ° relative to the molecular plane. Solubility was drastically improved in **3** as compared with **2**, making solution work much more facile.

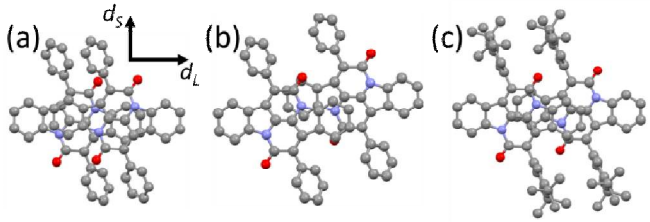

Figure 5.5
(a) **2α**, (b) **2β**, and (c) **3α** dimer pairs highlighting direction and extent of slip.

5.3.3. Steady-State Absorption

The absorption and PL spectra of the various films and solutions of **2** and **3** are gathered in Figure 5.6.The lowest energy vibronic absorption feature of **2** in toluene resides at 1.81 x

$10^4 cm^{-1}$, whereas TFs of **2** tend to be red-shifted by about 4.5×10^2 cm^{-1}. The relative intensities of the vibronic features within S_1 vary by film type and thickness. The ratio of amplitude of the lowest energy vibronic absorption feature, A_1, to the second vibronic absorption feature, A_2, is highest for **2α**, intermediate in **2β**, and lowest for **2a** for films of similar thicknesses. There exists, however a dependence on film thickness, such that A_1:A_2 is slightly inflated for thicker films, as the A_2 feature begins to saturate. While this provides a quick estimation of film type, XRD remains the most reliable measure of film composition. Absorption onsets for thicker films (> 250 nm) are red-shifted by about 250 cm^{-1} with respect to thinner films (< 50 nm). In **3** solution and **3a** TF, absorption onset are around 1.79×10^4 cm^{-1}, whereas upon annealing the TF to **3α**, absorption blue-shifts by almost 6×10^2 cm^{-1} to about 1.85×10^4 cm^{-1}.TF of **2** and **3** exhibit Davydov splitting and a shift in the relative amplitude of peaks of the vibronic envelope compared to solution data.

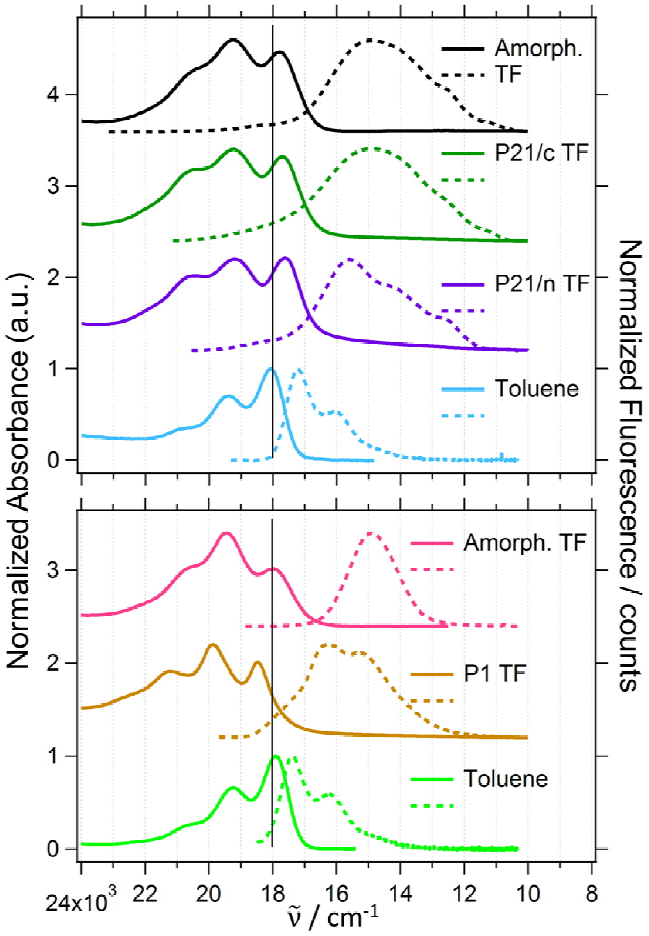

Figure 5.6

Normalized absorption and fluorescence of TF and solutions of **2** (top panel) and **3** (bottom panel).

5.3.4. Steady-State Photoluminescence

2β and **2a** TF steady-state PL spectra are rather broad, although there is some vibronic structure present. The **2α** PL spectra are somewhat sharper and slightly blue-shifted from those of the other film types. The maxima of the PL spectra of the three film types of **2** are red-shifted from the absorption onset by about 2.0 x 10^3 cm^{-1}. Solution PL of **2** is red-shifted by about 1.0 x 10^3 cm^{-1} from its absorption spectrum, and is quite close to being a mirror image of the absorption spectrum. As deposited **3a** TF PL spectra are broad and essentially featureless, and

are about 3.0 x 10^3 cm^{-1} red shifted from the absorption spectrum. Upon annealing, the TF PL spectrum is shifted by about 2.0 x 10^3 cm^{-1} from the absorption, and now has a clear vibronic progression, although it is not quite a mirror image of the absorption. PL for **3** in solution is red-shifted from the absorption by about 5 x 10^2 cm^{-1} and is a mirror image of the absorption spectrum. A broad and red-shifted emission feature on the low energy edge of the emission curves of **2α**, **2β**, and **2a** appears with a relatively low intensity. At low temperatures (13 K) the blue end of the emission lineshape has a large relative intensity, and as the temperature rises much of the relative intensity shifts towards the red (Figure 5.7).

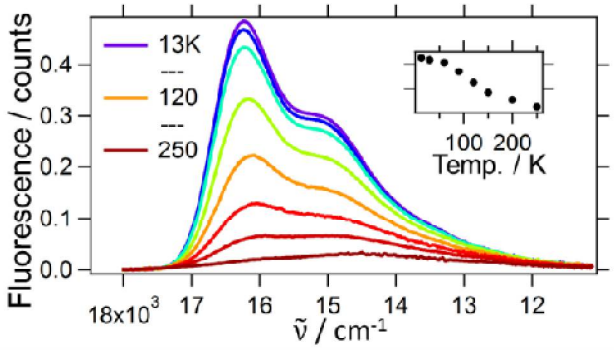

Figure 5.7
Variable temperature steady state fluorescence of **2α** TF. Inset is plot of integrated area as a function to temperature.

Toluene solutions of **2** and **3** have fluorescence quantum yields, Φ_F, of 80-90 %. Fluorescence in TFs, however, is strongly quenched with Φ_F values less than 1 x 10^{-3}, whereas **3** TF values are slightly higher at 3 x 10^{-3}.

5.3.5. Time-Resolved Photoluminescence

Fluorescence decays of **2** in solution are monoexponential, as seen in Figure 5.8c, and do not change as a function of emission wavelength. Unlike solution fluorescence decay kinetics, time-resolved photoluminescence (TRPL) decays collected on **2** and **3** TFs change as a function

of emission wavelength, exhibiting multiexponential kinetics with time constants on the order of several 10s of ps, 400 ps, and a small amplitude component of about 2 ns. The fast component is instrument response limited and has significant uncertainty. Nonetheless, it can be observed from Figure 5.8a, that among the three film types, the **2α** 650 nm (1.54 x 10^4 cm^{-1}) emission kinetics are faster, **2a**is intermediate, and **2β**is slightly slower. The relevant time constants of the individual decay components, their amplitudes, as well as Φ_F values can be found in Table 5.2. Emission decays of **2** and **3** TFs become significantly slower and approach monoexponential behavior as the red edge of the fluorescence is monitored, which is most evident in the 800 nm (1.25 x 10^4 cm^{-1}) decay, as depicted in Figures5.8b, d. In other molecular systems, this is commonly interpreted as excimer emission.[33,57,161]

Table 5.2

TRPL multiexponential fit coefficients (lifetimes and amplitudes) and Φ_F values for **2α**, **2β**, and **2a** TFs.

	2α 650 nm	**2β** 650 nm	**2a** 650 nm
A_1 (%)	95.2	89.3	94.1
τ_1 / ps	90	60	50
A_2 (%)	4.6	9.5	5.3
τ_2 / ps	390	430	400
A_3 (%)	0.3	1.1	0.5
τ_3 / ps	2010	2090	2490
Φ_F	0.001	0.001	0.001

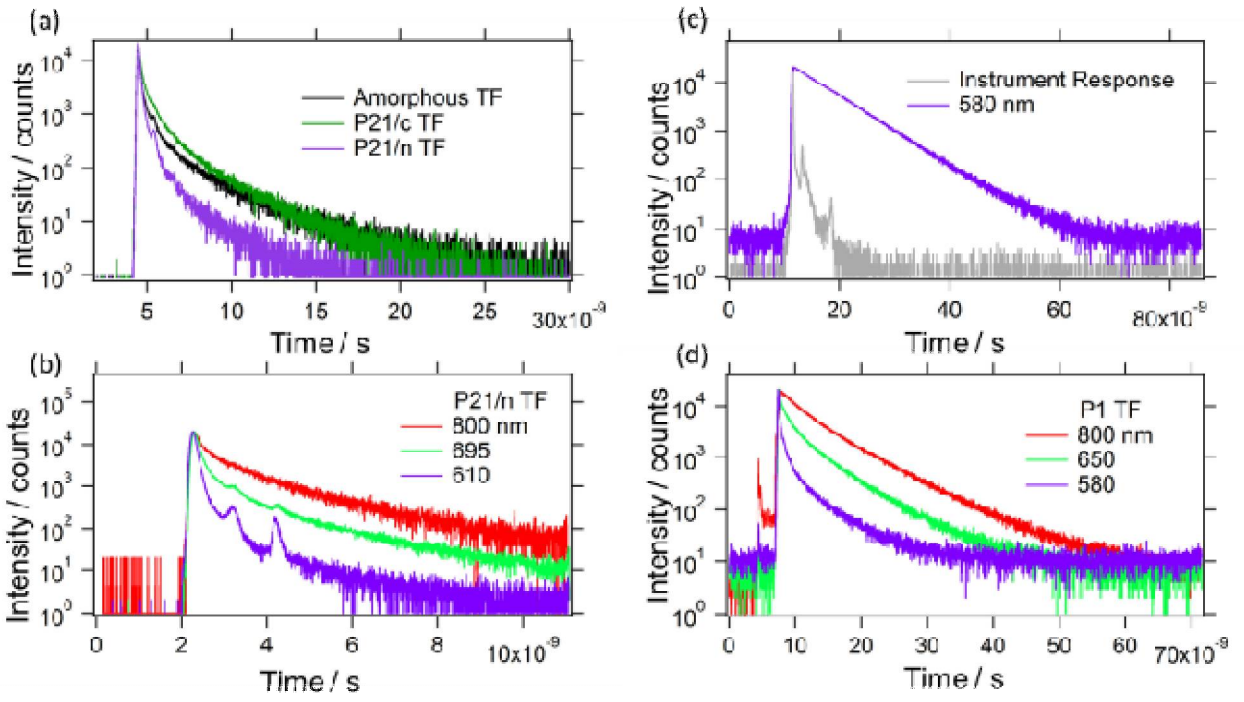

Figure 5.8

(a) TRPL decays of **2α**, **2β**, and **2a** TFs at an emission wavelength of 650 nm, (b) **2α**, (c) **2** toluene solution, and (d) **3α** TF TRPL decays at various emission wavelengths.

5.3.6. Transient Absorption

The transient absorption spectra of **2** have several characteristic features, and the photo induced absorptions and ground-state bleach (GSB) line shapes are broad and overlap extensively. The GSB is identical to the observed steady-state absorption (*vide supra*), and gives a negative transient signal. The singlet excited state absorptions, $S_1 \rightarrow S_n$, highlighted in pink in Figure 5.9a, are broad and appear around 1.4 and 2.3 x 10^4 cm^{-1}, and decay within the first few ps. The $T_1 \rightarrow T_n$ photo induced absorption features, accented in blue in Figure 5.9a, emerge at about 1.8 x 10^4 cm^{-1}. TF transient absorption spectra of **2α** at various times are collected in Figure 5.9a, whereas transient data of the other films and solutions appear in Figure 5.10. Singlet populations in TFs of **2** largely decay within the first 30-50 ps, with triplet formation

times occurring with a similar time constant, while **3α** TFs are approximately an order of magnitude slower with correlated time constants of about 300 ps. **2** and **3**solution kinetics are about 2 orders of magnitude slower than in polycrystalline and amorphous **2** TFs, with time constants around 5 ns.

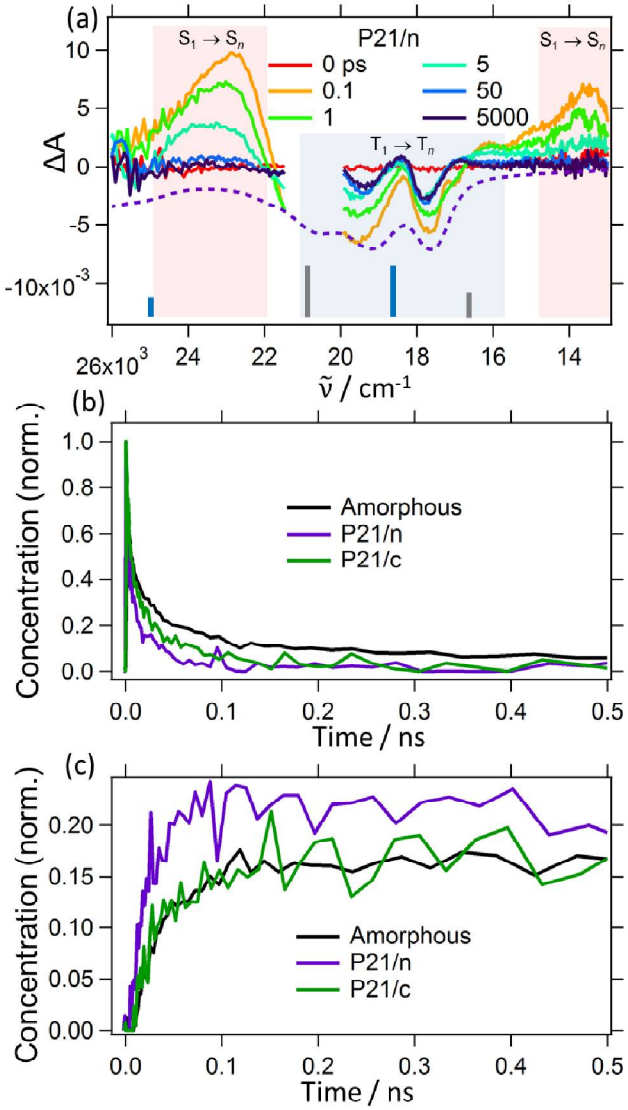

Figure 5.9

(a) Transient absorption spectra of 1α TF at various times from 0 – 5 ns along with overlaid GSB (dotted). Calculated singlet ground state (blue vertical bars) and triplet excited state (cobalt vertical bars) transitions depicted here, as well as experimentally observed, broad excited state singlet, $S_1 \rightarrow S_n$(pink shaded area), and triplet, $T_1 \rightarrow T_n$ (blue shaded area) . (b) **2α**, **2β**, and **2a** normalized singlet, and (c) triplet kinetics from concentration analysis.

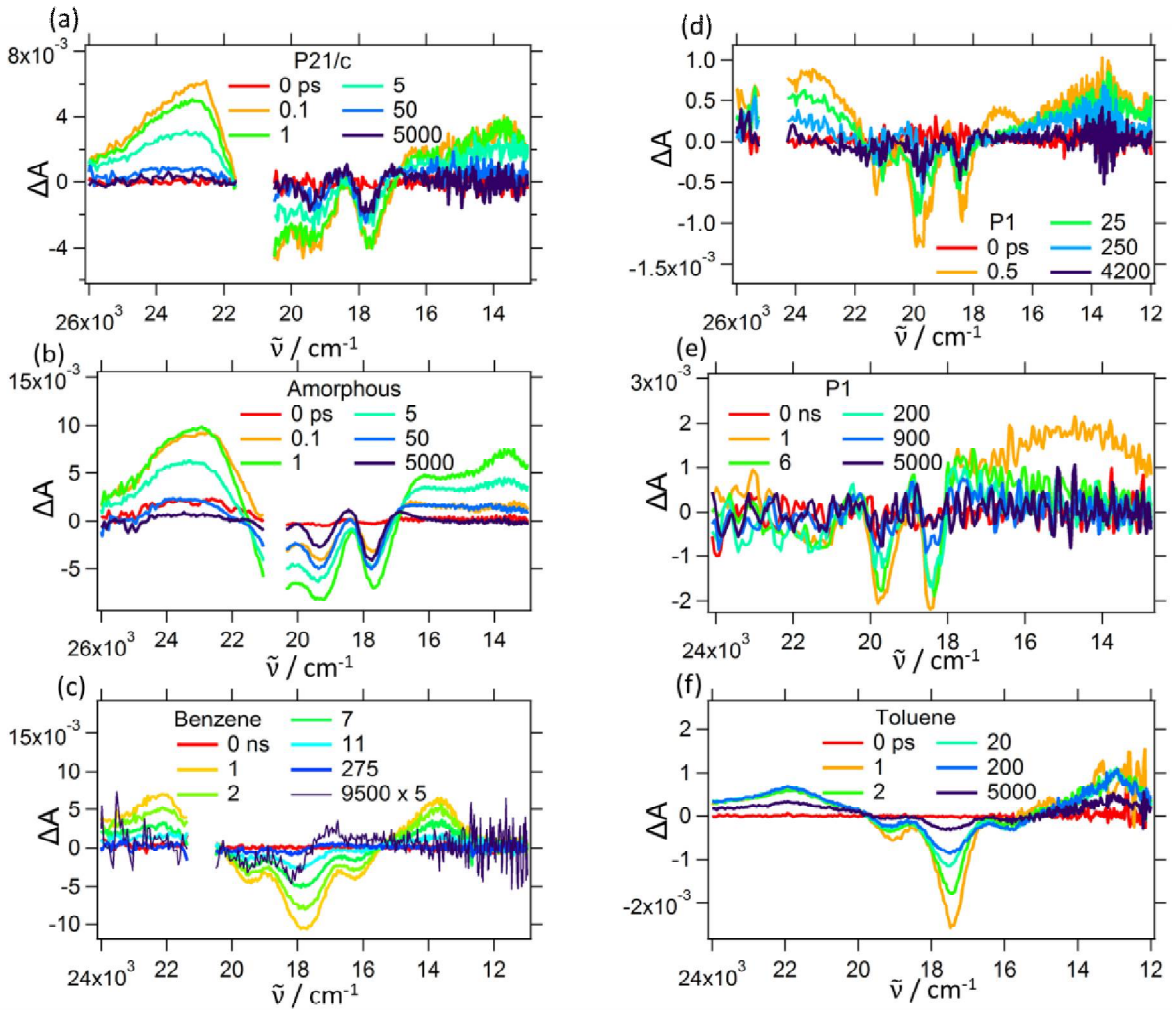

Figure 5.10

(a) Transient absorption spectra of **2β**TF at various time delays from 0 – 5 ns, (b) **2a** TF from 0 – 5 ns, (c) **2**benzene solution from 0 – 10 μs with the 9.5 μs spectra multiplied by 5 for clarity, (d) **3α** TF from 0 – 4 ns, (e) **3α**from 0 – 5 μs, and (f) **3** toluene solution from 0 – 5 ns.

Transient absorption data were interpreted by two methods: (i) spectral analysis and (ii) concentration analysis.

(i) An early time (~1 ps) transient trace and a late time (~5 ns or greater) transient trace are used to represent the spectral signature of states that are assumed to be of purely singlet and purely triplet character, respectively. The whole transient data series are then globally fitted using a linear combination of the two aforementioned states, in a similar manner to an analys is

thoroughly described and carried out in a previous study involving Tc polymorphs.[78] Spectral analysis requires no subtraction of the ground state bleach, and thus minimizes uncertainty in that respect. Normalized plots of the spectral components of the species as a function of time are obtained. This method effectively generates kinetics associated with singlet decay and triplet formation, but triplet quantum yield (Φ_T) is only calculable from rate constants considering there are no extinction coefficients involved. Although a Φ_T calculation from dynamics alone is somewhat adequate, a more robust analysis is required to gain certainty and incorporate additional photophysically significant factors, such as extinction coefficients, molecular orientation, and concentration of states.

(ii) Concentration analysis also begins with early time (a few hundred fs) and late time (~5 ns) transient spectra, extracted as a starting point to estimate singlet and triplet spectra. A steady state absorption spectrum was scaled and overlaid on the ground state bleach (GSB) and then subtracted from these transient absorption data to make these spectra purely absorptive. The $S_1 \rightarrow S_n$ excited state absorption, $T_1 \rightarrow T_n$ excited state absorption, and steady state absorption spectra were then scaled to the extinction coefficients determined from values found in the literature.[151] Once the three extinction coefficient scaled spectra are obtained, the entire transient data set is globally fitted using the aforementioned spectra. The global fit takes the spectra of these three states (proportional to electronic populations) and fits ~100 transient curves at various times to extract the concentrations of states, or populations, as a function of time. Φ_T, again, is calculated with Equation 3.3, which is reiterated here for convenience, which is valid at normal incidence $\Phi_T = \frac{\Delta A^T}{\Delta A^{S_1}} \frac{\varepsilon_{S_1}}{\varepsilon_{T_1}} r$, where, again, ΔA^T is the transient signal of the triplet absorption (T1 $\rightarrow$ Tn, late time), ΔA^{S_1} is the transient signal of the excited state singlet absorption, (S1 $\rightarrow$ Sn, early time), ε_{S1} is the extinction coefficient of the S1 state, ε_{T1} is the

extinction coefficient of the T_1 state. The factor r is the correction that accounts for the special case of non-aligned (molecular frame) and non-isotropic (laboratory frame) bleach and triplet transition dipole moment orientations.

A detailed description and definition of r, and of concentration analysis in general have been outlined previously.[57] In this context, r is the ratio of the amount of T_1-T_n absorption at the wavelength represented by ΔA^T that has a transition dipole moment that is parallel to the surface normal compared to the to the corresponding quantity for the bleach, ΔA^{S_1}. In solution, these transition moments are oriented isotropically, thus r = 1 (each transition has 1/3 orientation factor along each axis in the laboratory frame). An amorphous film has the same factor. Similarly, a film with molecules with S0-S1 and relevant T_1-T_n transition moments that are aligned would have r = 1, regardless of the degree of molecular alignment. Films that are textured (i.e., polycrystalline) without this condition would require knowledge of the crystal structure, the crystal plane orientation in the laboratory frame, and the transition dipole moment directions in the molecular frame to predict r. Equivalently, one can perform a series of experiments in which the incident polarized light vector takes varying angles with respect to the surface normal. We have performed both the calculations and the experiments to arrive at a consistent set of results. In some cases, considerable deviation between experimental and calculated results suggests that a portion of the film is amorphous in character, which can be challenging to quantify because it lacks an XRD signal, and cannot be clearly identified with any optical signature.

In order to determine Φ_T, the GSB was subtracted from the spectra of interest, the resulting curves were scaled to known extinction coefficients, and the concentration analysis fitting was performed. Transient spectra of the **2α** TF at various times, as well as steady state

absorption (scaled to GSB), calculated transition moments (vertical bars), and experimentally observed excited state spectral signal regions are depicted in Figure 5.9a. The singlet and triplet kinetics of the three TF types of **2** displayed in Figures 5.9b, c were generated from concentration analysis fitting. Φ_T values calculated from concentration analysis (incorporating orientation correction factors when necessary) range from 17 – 43 % and are listed in Table 5.3. The spectral and concentration transient global fitting analyses yielded almost identical results, with the only discernible difference being that the spectral analysis method provided a better fit of the very early time data (0 – 10 ps) (Figure 5.11c).

Table 5.3

Φ_T of **2**and **3** TFs and solution, determined from concentration analysis.

	Φ_T (%)
2 Benzene	4 +/- 2
2α TF	23 +/- 3
2β TF	48 +/- 5
2a TF	17 +/- 2
3 Toluene	< 1
3α TF	14 +/- 3

The kinetic data and Φ_T estimates reported here were from experiments using low fluence (~25 nJ/pulse, excitation density ~10^{18} cm^{-3}) and have been confirmed to be in the annihilation-free regime. To verify this, the fluence was decreased until no further change in kinetics was observed. Variable temperature transient absorption measurements were performed on these TFs and surprisingly there was no change in the observed spectra or kinetics from 77 – 500 K.

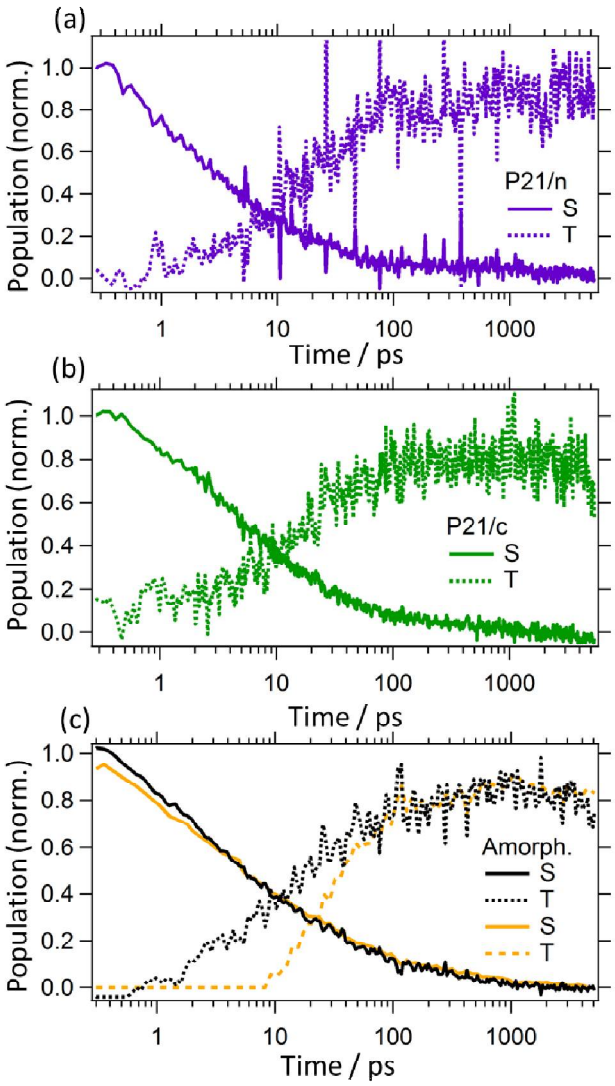

Figure 5.11

Singlet and triplet dynamics generated from transient absorption spectral analysis global fitting of (a) **2α**, (b) **2β**, and (c) **2a**. The orange traces in (a) were generated from concentration analysis.

The aqueous NP suspension absorption was measured and the spectrum closely matches that of **2α**, and upon dropcasting NPs and running XRD, it was confirmed that the particles were indeed of **2α** morphology. This result is not surprising, however, because **2α** is the thermodynamically stable polymorph, and also because the NPs are exposed to THF solvent vapors that have been shown to induce crystalline reorganization to **2α**. TA results were

interpreted using the concentration analysis, and the NP Φ_T value was found to be 22%, in close agreement with the **2α** TF results. The NPs in the aqueous suspension are isotropic in orientation, so no *r* correction factor was incorporated in this yield calculation.

5.3.7. Orientation Considerations

There was no observed change in absorption at various film rotations about film surface normal, indicating **2** and **3** TFs are uniaxial (or amorphous). Films of **2α** showed three diffraction peaks in its XRD pattern, corresponding to three diffraction planes that are considerably distinct and non-parallel. Inspection of these planes leads us to conclude that the net orientation of the six unique molecular orientations (two molecules per unit cell and three distinct crystallite orientations) will represent a situation approaching a distribution close to an isotropic approximation. Similarly amorphous films can be approximated to have an isotropic distribution of molecular orientations. Ultimately, these two film types are considered isotropic and have no orientation factor associated with their Φ_T estimates. However, **2β** films have only one diffraction peak, corresponding to the (011) plane. The calculated transition dipole moment directions for the relevant singlet and triplet transitions, shown in Figure 5.2, were incorporated into a model simulating a uniaxial **2β** system with the (011) plane parallel to the substrate. The dot products between the light vector and the dipole vectors were calculated and summed at various sample tilt angles. The ratio of r_T:r_S was plotted as a function of tilt angle to explore the theoretical *r* factor, which was evaluated to be 7.5.In other words, the ratio of signal from T to the signal from S is at normal incidence is smaller by a factor of 7.5 compared to that at 90 ° tilt angle, because of transition dipole orientations. Polarized tilt angle steady state absorption and transient experiments were carried out at various tilt angles ranging from normal incidence (0 °) to 75 °. Changes in the ratio of $\Delta A^{T}/\Delta A^{S_1}$ over the tilt series were observed in **2β** films, but not

2α or **2a** TFs, thus confirming the necessity of a correction factor for **2β** and justifying the omission for the others. In addition, **1α** NP Φ_T calculations (*sine r* correction) agree remarkably well with those from **1α**TF TA analysis, thus asserting that indeed no *r* correction is necessary.

Polarized tilt angle steady state absorption measurements reveal that **2β** films are actually only about 30% **2β**, (estimated by observing experimental ΔAbs changing by about 30 % as compared to calculations), suggesting that the rest is likely isotropically oriented **2a**(Figure 5.12). This is not surprising, considering the thickness threshold needed to obtain **2β**. TF XRD data also alludes that there is a small presence of **2α** in **2β** polycrystalline TFs. At normal incidence, the apparent $\Delta A^T/\Delta A^{S_1}$ value for **1β** films is suppressed due to transition dipole moment orientation. Upon tilting, the $\Delta A^T/\Delta A^{S_1}$value increases at very high tilt angles, thus revealing the true 1β TF ΦT value of 48 %. Whereas, according to calculations, if the film were purely 1β uniaxially oriented (with the (011) face parallel to the substrate as previously described), Φ_T could be as high as 135 % (incorporating a multiplicative *r* factor of 7.5).Since a large majority of the film composition is **2a** (and **2α**), and also because the observed ΦT is only 48%, the film is likely only about 26 % **2β**. The calculated and experimentally observed Φ_T values are presented in Figure 5.13 (normalized to Φ_T = 18% at 0 °, normal incidence).

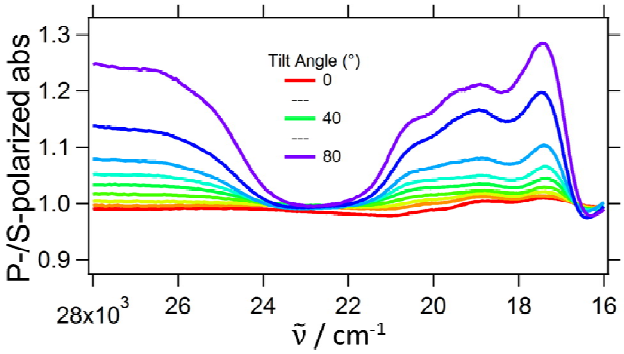

Figure 5.12

P-polarized divided by S-polarized absorption spectra at various tile angles (0 – 80 °).

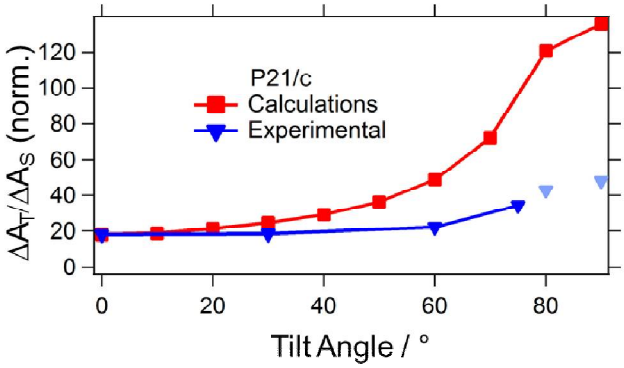

Figure 5.13

Calculated and experimentally determined **2β** $\Delta A^{T}/\Delta A^{S_1}$ as a function of tilt angle. The light blue markers have been extrapolated from observed results.

Φ_T values are relatively low, ranging from about 14 – 23 % in **2α**, **2a**, and **3α** TFs, to an upper limit of approximately 50 % in **2β** films. If a pure **2β** film could be produced, theoretical Φ_T values could be as high as 135 %. **2** and **3** TFs appear to suffer from ultrafast excimer formation that depopulates the S_1 state significantly, prohibiting efficient SF, and could help explain why the Φ_F is so low in the films. This claim is supported by the observation of i.) excimer-like emission on the red end of the steady-state PL, ii.) shifting of the relative amplitude

of the steady-state PL towards the red upon when moving from low to high temperature, and iii.) long lived emission lifetimes toward the lower energy region of the PL.

The addition of bulky t-butyl groups to form **3**, which is expected to reduce intermolecular coupling in the solid phase that causes a red-shift and excimer formation, did not significantly increase the intermolecular distance. Despite the differences in structure between the two **2** polymorphs and the **3α** polymorph, the films have some degree of amorphous character, and thus geometries that give rise to excimer formation could exist in overwhelming abundance.[162] It is also possible that, contrary to calculated energy levels, the S_1 state is considerably lower in energy (> 100 meV) than the ^{1}(TT) state, thus suppressing k_{SF} significantly.

5.4. Conclusions

Despite **2** possessing several attractive attributes, such as stability, absorbing in the optimal spectral region, and having biradical character, Φ_T values remain low, likely due to excimer formation. Further derivatization of **2** could enable variation in intermolecular geometries, alteration of energy levels, and increased solubility. Perhaps different preparation techniques could yield films that are highly enriched in **2β** character, such that a Φ_T of 135 % could be observed. A thorough kinetic fitting examination could be performed in the future. Target analysis could help reveal rate constants and potentially elucidate why triplet yields are quite low as well as which competing processes are dominating. Target analysis, similar to that performed in the studies of **1** and Tc, would likely be the most thorough approach.

6. Conclusions

In depth studies on **1**, Tc, **2**, and**3** have helped shape detailed photophysical pictures, and much insight has been gained via TF preparation and spectroscopic studies. Polymorphism is commonly encountered and even subtle dissimilarities in crystal structures can lead to drastic changes in dynamics, yields, and stability. Unfortunately in some cases, i.e. **1** and **2**, the unstable polymorph demonstrates enhanced performance. Much discussion of various fundamental characteristics of these systems has been presented above, but it is important to also assess how viable these materials could be in a working device.

6.1. 1,3-Diphenylisobenzofuran

α-**1** TFs efficiently generate triplet excitons with high yields, but instability in air and light, as well as interconversion to β-**1**, remain hurdles in making TFs that can maintain **α** character. Reliable methods for producing TFs of two polymorphs of **1** have been developed, utilizing thermal evaporation as well as solution dropcasting.α-**1** films were grown by thermally evaporating TFs >80 nm, whereas β-**1** TFs could be grown by depositing thinner layers, depositing onto a heated substrate, or interconverted by subsequently thermal annealing. Alternatively, α-**1** films could were solution dropcast from a 1:1 chloroform:toluene**1** solution, while β-**1** films were cast from solutions of different ratios, or from a different solvent altogether. Bulk crystals and TFs of the two polymorphs were prepared and structurally characterized. A major finding in the study of **1** TFs is that α-**1**has a higher S_1 energy level, making the $S_1 \rightarrow {}^1(TT)$ SF process energetically downhill. The β-**1** polymorph has a lower S_1 energy level, and thus the ${}^1(TT)$ is energetically inaccessible, hindering SF and instead promoting excimer formation. In addition to high triplet yields, **1** has some other redeeming

qualities. **1** is a biradicaloid, absorbs in the appropriate range of the electromagnetic spectrum, it is relatively cheap and has also been incorporated as a sensitizer into a dye-sensitized solar cell and generated current upon illumination.[163] Transient data were thoroughly analyzed, SF mechanisms were determined by globally fitting transient data to a kinetic scheme by global target analysis, and yields were determined for both polymorphs. α-**1**TF Φ_T yields are close to 2, whereas those of β-**1** TFs are much lower, about 0.1.

6.2. Tetracene

Tc, shown to have remarkably high, near 200 % triplet yields, has been incorporated into solar cells, although efficiency remains quite low. Tc is quite stable, absorbs in the appropriate spectral range, and has been studied quite thoroughly. In general, functionalization of this chromophore has led to some exciting results recently and will continue to be a relevant pursuit. Polymorphism in Tc has been addressed, and, along with crystallite size, will now be considered in future TF or bulk crystal investigations. Thermally evaporating films onto hot substrates yielded Tc I films, whereas depositing onto cryo substrates reproducibly yielded Tc II TFs. Tc I and Tc II TFs were structurally characterized and differentiated, and compared to the bulk powder patterns of the two polymorphs. Deposition rate determined crystallite size, with faster rates producing smaller crystals and slower rates producing larger crystals. Moreover, the work presented here it was found that SF occurs faster in the Tc II polymorph as compared with Tc I, and also that Tc II crystallite size has no effect on SF time constants. SF occurs more slowly in Tc I, and SF time constants are quite dependent on crystallite size, increasing by about a factor of 5 as crystallite size varies from about 200 nm to several μm. Calculations on nearest neighbor dimer couplings suggest that Tc I should be faster overall, but that result was not observed

experimentally, prompting a need for more rigorous, multimolecule (>3) coupling calculations, especially if the singlet is highly delocalized.

6.3. Indigo Derivatives

The indigo derivatives **2** and **3** are remarkably stable, biradical in nature, have excellent transport properties, and absorb in the optimal spectral range. While initial calculations and high Φ_F values suggested that SF should be quite efficient in this system, excimer formation appears to dominate, thus outcompeting SF. Reproducible methods to produce **2α**, **2β**, **2a**, **3α,** and **3a** TFs were developed by exploiting capabilities such as deposition rate and substrate temperature, as described above.In addition to TFs, **2α** NPs were synthesized by reprecipitation. Because **2** has very low solubility, solution processing and preparation of TF from solution phase would be somewhat impractical. Despite the exciting aspect of improved solubility of **3**, itsSF performance is stifled. **2α** (TFs and NPs), **2a**, and **3α** TFs have Φ_T values of 15-25%, while **2β** has slightly better performance with a Φ_T value of 48%. Theoretically, $\Phi_T$of **2β** could be as high as 135% if a purely uniaxial **2β** TF could be generated. However, attempts to make such a film have proved fruitless, because similar to α-**1**, there is a thickness threshold needed to obtain the **2β** polymorph. If alternative TF preparation techniques could generate a purely **2β** film, or if varied reprecipitation methods could produce purely **2β** NPs, yields could be checked against calculations, and the 135% Φ_T could be potentially realized.[164]Further derivatization or alternate TF and NP preparation techniques could aid in arriving at other geometries more favorable for SF.

7. References

(1) Nozik, A. J.; Miller, J.: Introduction to Solar Photon Conversion. *Chem. Rev.* **2010**, *110*, 6443-6445.

(2) UN: Conference of the Parties - Paris Agreement. *Framework Convention on Climate Change.* **2015**, *21*, 1-32.

(3) Tsao, J.; Lewis, N.; Crabtree, G.: Solar FAQs. *US Department of Energy.* **2006**.

(4) Shockley, W.; Queisser, H. J.: Detailed Balance Limit of Efficiency of pn Junction Solar Cells. *J. Appl. Phys.* **1961**, *32*, 510-519.

(5) NCPV; NREL: Best Research-Cell Efficiencies. *US Department of Energy.* **2016**.

(6) Beard, M. C.; Johnson, J. C.; Luther, J. M.; Nozik, A. J.: *Philos. Trans. R. Soc., A* **2015**, *373*, 2014012.

(7) Beard, M. C.; Johnson, J. C.; Luther, J. M.; Nozik, A. J.: Multiple exciton generation in quantum dots versus singlet fission in molecular chromophores for solar photon conversion. *Philos. T. R. Soc. A.* **2015**, *373*.

(8) Smith, M. B.; Michl, J.: Singlet Fission. *Chem. Rev.* **2010**, *110*, 6891.

(9) Singh, S.; Jones, W. J.; Siebrand, W.; Stoicheff, B. P.; Schneider, W. G.: Laser Generation of Excitons and Fluorescence in Anthracene Crystals. *J. Chem. Phys.* **1965**, *42*, 330-342.

(10) Pope, M.; Geacintov, N. E.; Vogel, F. E.: Singlet Exciton Fission and Triplet-Triplet Exciton Fusion in Crystalline Tetracene. *Mol. Cryst. Liq. Cryst.* **1969**, *6*, 83-104.

(11) Singh, S.; Jones, W. J.; Siebrand, W.; Stoicheff, B. P.; Schneider, W. G.: Laser Generation of Exictons and Fluorescence in Anthracene Crystals. *J. Chem. Phys.* **1965**, *42*.

(12) Merrifield, R. E.; Avakian, P.; Groff, R. P.: Fission of Singlet Excitons into Pairs of Triplet Excitons in Tetracene Crystals. *Chem. Phys. Lett.* **1969**, *3*, 386-388.

(13) Merrifield, R. E.: Magnetic Effects on Triplet Exciton Interactions. *Pure Appl. Chem.* **1971**, *27*, 481-498.

(14) Klein, G.; Voltz, R.: Formation and Decay of Superexcited States in Dense Organic Matter Under High Energy Radiation. *Int. J. Radiat. Phys. Chem.* **1975**, *7*.

(15) Rademaker, H.; Hoff, A. J.; Grondelle, R. v.; Duysens, L. N. M.: Carotenoid Triplet Yields in Normal and Deuterated Rhodospirillum Rubrum. *Biochim. Biophys. Acta, Bioenerg.* **1980**, *592*, 240-257.

(16) Austin, R. H.; Baker, G. L.; Etemad, S.; Thompson, R.: Magnetic Field Effects on Triplet Exciton Fission and Fusion in Polydiacetylene. *J. Phys. Chem.* **1989**, *90*, 6642-6646.

(17) Hanna, M. C.; Nozik, A. J.: Solar Conversion Efficiency of Photovoltaic and Photoelectrolysis Cells with Carrier Multiplication Absorbers. *J. Appl. Phys.* **2006**, *100*, 074510.

(18) Hanna, M. C.; Nozik, A. J.: Solar conversion efficiency of photovoltaic and photoelectrolysis cells with carrier multiplication absorbers. *J. Appl. Phys.* **2006**, *100*, 074510.

(19) Shpaisman, H.; Niitsoo, O.; Lubomirsky, I.; Cahen, D.: Can up- and down-conversion and multi-exciton generation improve photovoltaics? *Sol. Energ. Mat. Sol. Cells.* **2008**, *92*, 1541-1546.

(20) Tayebjee, M. J. Y.; Gray-weale, A. A.; Schmidt, T. W.: Thermodynamic Limit of Exciton Fission Solar Cell Efficiency. *J. Phys. Chem. Lett.* **2012**, *3*, 2749-2754.

(21) Smith, M. B.; Michl, J.: Recent Advances in Singlet Fission. *Ann. Rev. Phys. Chem.* **2013**, *64*, 361-386.

(22) Johnson, J. C.; Nozik, A. J.; Michl, J.: The Role of Chromophore Coupling in Singlet Fission. *Acc. Chem. Res.* **2013**, *46*, 1290-1299.

(23) Sanders, S. N.; Kumarasamy, E.; Pun, A. B.; Trinh, M. T.; Choi, B.; Xia, J.; Taffet, E. J.; Low, J. Z.; Miller, J. R.; Roy, X.; Zhu, X.-Y.; Steigerwald, M. L.; Sfeir, M. Y.; Campos, L. M.: Quantitative Intramolecular Singlet Fission in Bipentacenes. *J. Am. Chem. Soc.* **2015**, *137*, 8965-8972.

(24) Wang, R.; Zhang, C.; Zhang, B.; Liu, Y.; Wang, X.; Xiao, M.: Magnetic Dipolar Interactions Between Correlated Triplets Created by Singlet Fission in Tetracene Crystals. *Nat. Commun.* **2015**, *6*, 1-6.

(25) Scholes, G. D.: Correlated Pair States Formed by Singlet Fission and Exciton-Exciton Annihilation. *J. Phys. Chem. A* **2015**, *119*, 12699-12705.

(26) Smith, M. B.; Michl, J.: Singlet Fission. *Chem. Rev.* **2010**, *110*, 6891-6936.

(27) Busby, E.; Xia, J.; Wu, Q.; Low, J. Z.; Song, R.; Miller, J. R.; Zhu, X.-Y.; Campos, L. M.; Sfeir, M. Y.: A design strategy for intramolecular singlet fission mediated by charge-transfer states in donor–acceptor organic materials. *Nat. Mater.* **2015**, *14*, 426-433.

(28) Pensack, R. D.; Tilley, A. J.; Parkin, S. R.; Lee, T. S.; Payne, M. M.; Gao, D.; Jahnke, A. A.; Oblinsky, D. G.; Li, P.-F.; Anthony, J. E.; Seferos, D. S.; Scholes, G. D.: Exciton Delocalization Drives Rapid Singlet Fission in Nanoparticles of Acene Derivatives. *J. Am. Chem. Soc.* **2015**, *137*, 6790-6803.

(29) Eaton, S. W.; Miller, S. A.; Margulies, E. A.; Shoer, L. E.; Schaller, R. D.; Wasielewski, M. R.: Singlet Exciton Fission in Thin Films of tert-Butyl-Substituted Terrylenes. *J. Phys. Chem. A.* **2015**, *119*, 4151-4161.

(30) Kolata, K.; Breuer, T.; Witte, G.; Chatterjee, S.: Molecular Packing Determines Singlet Exciton Fission in Organic Semiconductors. *ACS Nano.* **2014**, *8*, 7377-7383.

(31) Herz, J.; Buckup, T.; Paulus, F.; Engelhart, J. U.; Bunz, U. H. F.; Motzkus, M.: Unveiling Singlet Fission Mediating States in TIPS-pentacene and its Aza Derivatives. *J. Phys. Chem. A* **2015**, *119*, 6602-6610.

(32) Dillon, R. J.; Piland, G. B.; Bardeen, C. J.: Different Rates of Singlet Fission in Monoclinic versus Orthorhombic Crystal Forms of Diphenylhexatriene. *J. Am. Chem. Soc.* **2013**, *135*, 17278-17281.

(33) Ryerson, J. L.; Schrauben, J. N.; Ferguson, A. J.; Sahoo, S. C.; Michl, J.; Nozik, A. J.; Johnson, J. C.: Two Thin Film Polymorphs of the Singlet Fission Compound 1,3- Diphenylisobenzofuran. *J. Phys. Chem. C.* **2014**, *118*, 12121-12132.

(34) Feng, X.; Kolomeisky, A. B.; Krylov, A. I.: Dissecting the Effect of Morphology on the Rates of Singlet Fission: Insights from Theory. *J. Phys. Chem. C* **2014**, *118*, 19608-19617.

(35) Moon, H.; Zeis, R.; Borkent, E.-J.; Besnard, C.; Lovinger, A. J.; Siegrist, T.; Kloc, C.; Bao, Z.: Synthesis, Crystal Structure, and Transistor Performance of Tetracene Derivatives. *J. Am. Chem. Soc.* **2004**, *126*, 15322-15323.

(36) Knipp, D.; Street, R. A.; Volkel, A.; Ho, J.: Pentacene thin film transistors on inorganic dielectrics: Morphology, structural properties, and electronic transport. *J. Appl. Phys.* **2003**, *93*, 347-355.

(37) Piland, G. B.; Bardeen, C. J.: How Morphology Affects Singlet Fission in Crystalline Tetracene. *J. Phys. Chem. Lett.* **2015**, *6*, 1841-1846.

(38) Musser, A. J.; Al-Hashimi, M.; Maiuri, M.; Brida, D.; Heeney, M.; Cerullo, G.; Friend, R. H.; Clark, J.: Activated Singlet Exciton Fission in a Semiconducting Polymer. *J. Am. Chem. Soc.* **2013**, *135*, 12747-12754.

(39) Eaton, S. W.; Shoer, L. E.; Karlen, S. D.; Dyar, S. M.; Margulies, E. A.; Veldkamp, B. S.; Ramanan, C.; Hartzler, D. A.; Savikhin, S.; Marks, T. J.; Wasielewski, M. R.: Singlet Exciton Fission in Polycrystalline Thin Films of a Slip-Stacked Perylenediimide. *J. Am. Chem. Soc.* **2013**, *135*, 14701-14712.

(40) Renaud, N.; Grozema, F. C.: Intermolecular Vibrational Modes Speed Up Singlet Fission in Perylenediimide Crystals. *J. Phys. Chem. Lett.* **2015**, *6*, 360-365.

(41) Musser, A. J.; Maiuri, M.; Brida, D.; Cerullo, G.; Friend, R. H.; Clark, J.: The Nature of Singlet Exciton Fission in Carotenoid Aggregates. *J. Am. Chem. Soc.* **2015**, *137*, 5130-5139.

(42) Wang, C.; Tauber, M. J.: High-Yield Singlet Fission in a Zeaxanthin Aggregate Observed by Picosecond Resonance Raman Spectroscopy. *J. Am. Chem. Soc.* **2010**, *132*, 13988-13991.

(43) Roberts, S. T.; McAnally, R. E.; Mastron, J. N.; Webber, D. H.; Whited, M. T.; Brutchey, R. L.; Thompson, M. E.; Bradforth, S. E.: Efficient Singlet Fission Discovered in a Disordered Acene Film. *J. Am. Chem. Soc.* **2012**, *134*, 6388-6400.

(44) Burdett, J. J.; Bardeen, C. J.: The Dynamics of Singlet Fission in Crystalline Tetracene and Covalent Analogs. *Acc. Chem. Res.* **2013**, *46*, 1312-1320.

(45) Thorsmølle, V. K.; Averitt, R. D.; Demsar, J.; Smith, D. L.; Tretiak, S.; Martin, R. L.; Chi, X.; Crone, B. K.; Ramirez, A. P.; Taylor, A. J.: Morphology Effectively Controls Singlet-Triplet Exciton Relaxation and Charge Transport in Organic Semiconductors. *Phys. Rev. Lett.* **2009**, *102*, 017401.

(46) Wilson, M. W. B.; Rao, A.; Clark, J.; Kumar, R. S. S.; Brida, D.; Cerullo, G.; Friend, R. H.: Ultrafast Dynamics of Exciton Fission in Polycrystalline Pentacene. *J. Am. Chem. Soc.* **2011**, *133*, 11830-11833.

(47) Musser, A. J.; Liebel, M.; Schnedermann, C.; Wende, T.; Kehoe, T. B.; Rao, A.; Kukura, P.: Evidence for conical intersection dynamics mediating ultrafast singlet exciton fission. *Nat. Phys.* **2015**, *11*, 352-357.

(48) Congreve, D. N.; Lee, J.; Thompson, N. J.; Hontz, E.; Yost, S. R.; Reusswig, P. D.; Bahlke, M. E.; Reineke, S.; Van Voorhis, T.; Baldo, M. A.: External Quantum Efficiency Above 100% in a Singlet-Exciton-Fission-Based Organic Photovoltaic Cell. *Science* **2013**, *340*, 334-337.

(49) Lee, J.; Jadhav, P.; Reusswig, P. D.; Yost, S. R.; Thompson, N. J.; Congreve, D. N.; Hontz, E.; Van Voorhis, T.; Baldo, M. A.: Singlet Exciton Fission Photovoltaics. *Acc. Chem. Res.* **2013**, *46*, 1300-1311.

(50) Yang, L.; Tabachnyk, M.; Bayliss, S. L.; Bo, M. L.; Broch, K.; Greenham, N. C.; Friend, R. H.; Ehrler, B.: Solution-Processable Singlet Fission Photovoltaic Devices. *Nano Lett.* **2015**, *15*, 354-358.

(51) Wilson, M. W. B.; Rao, A.; Clark, J.; Kumar, R. S. S.; Brida, D.; Cerullo, G.; Friend, R. H.: Ultrafast Dynamics of Exciton Fission in Polycrystalline Pentacene. *J. Am. Chem. Soc.* **2011**, *133*, 11830-11833.

(52) Burdett, J. J.; Gosztola, D.; Bardeen, C. J.: The dependence of singlet exciton relaxation on excitation density and temperature in polycrystalline tetracene thin films: Kinetic evidence for a dark intermediate state and implications for singlet fission. *J. Chem. Phys.* **2011**, *135*, 214508.

(53) Burdett, J. J.; Müller, A. M.; Gosztola, D.; Bardeen, C. J.: Excited state dynamics in solid and monomeric tetracene: The roles of superradiance and exciton fission. *J. Chem. Phys.* **2010**, *133*, 144506.

(54) Thompson, N. J.; Wilson, M. W. B.; Congreve, D. N.; Brown, P. R.; Scherer, J. M.; Bischof, T. S.; Wu, M.; Geva, N.; Welborn, M.; Voorhis, T. V.; Bulovic, V.; Bawendi, M.; Baldo, M. A.: Energy harvesting of non-emissive triplet excitons in tetracene by emissive PbS nanocrystals. *Nat. Mater.* **2014**, *13*.

(55) Lee, J.; Jadhav, P.; Baldo, M. A.: High efficiency organic multilayer photodetectors based on singlet fission. *Appl. Phys. Lett.* **2009**, *95*, 033301.

(56) Johnson, J. C.; Nozik, A. J.; Michl, J.: High Triplet Yield from Singlet Fission in a Thin Film of 1,3-Diphenylisobenzofuran. *J. Am. Chem. Soc.* **2010**, *132*, 16302-16303.

(57) Schrauben, J. N.; Ryerson, J.; Michl, J.; Johnson, J. C.: The Mechanism of Singlet Fission in Thin Films of 1,3-Diphenylisobenzofuran. *J. Am. Chem. Soc.* **2014**, *136*, 7363-7373.

(58) Tabachnyk, M.; Ehrler, B.; Gelinas, S.; Bohm, M. L.; Walker, B. J.; Musselman, K.; Greenham, N. C.; Friend, R. H.; Rao, A.: Resonant energy transfer of triplet excitons from pentacene PbSe nanocrystals. *Nat. Mater.* **2014**, *13*, 1033-1038.

(59) Busby, E.; Berkelbach, T. C.; Kumar, B.; Chernikov, A.; Zhong, Y.; Hlaing, H.; Zhu, X.-Y.; Heinz, T. F.; Hybersten, M. S.; Sfeir, M. Y.; Reichman, D. R.; Nuckolls, C.; Yaffe, O.: Multiphonon Relaxation Slows Singlet Fission in Crystalline Hexacene. *J. Am. Chem. Soc.* **2014**, *136*, 10654-10660.

(60) Wang, C.; Tauber, M. J.: High-Yield Singlet Fission in a Zeaxanthin Aggregate Observed by Picosecond Resonance Raman Spectroscopy. *J. Am. Chem. Soc.* **2010**, *132*, 13988-13991.

(61) Grumstrup, E. M.; Johnson, J. C.; Damrauer, N. H.: Enhanced Triplet Formation in Polycrystalline Tetracene Films by Femtosecond Optical-Pulse Shaping. *Phys. Rev. Lett.* **2010**, *105*, 257403.

(62) Paci, I.; Johnson, J. C.; Chen, X. D.; Rana, G.; Popovic, D.; David, D. E.; Nozik, A. J.; Ratner, M. A.; Michl, J.: Singlet Fission for Dye-Sensitized Solar Cells: Can a Suitable Sensitizer be Found? *J. Am. Chem. Soc.* **2006**, *128*, 16546-16553.

(63) Anthony, J.: Functionalized Acenes and Heteroacenes for Organic Electronics. *Chem. Rev.* **2006**, *106*, 5028-5048.

(64) Jundt, C.; Klein, G.; Moigne, J. L.: Yield of Tirplet Exciton Pairs in Polydiacetylene Films. *Chem. Phys. Lett.* **1993**, *203*, 37-40.

(65) Johnson, J. C.; Nozik, A. J.; Michl, J.: The Role of Chromophore Coupling in Singlet Fission. *Acc. Chem. Res.* **2013**, *46*, 1290-1299.

(66) Schrauben, J. N.; Akdag, A.; Wen, J.; Havlas, Z.; Ryerson, J. L.; Smith, M. B.; Michl, J.; Johnson, J. C.: Excitation Localization/Delocalization Isomerism in a Strongly Coupled Covalent Dimer of 1,3-Diphenylisobenzofuran. *J. Phys. Chem. A.* **2016**.

(67) Berkelbach, T. C.; Hybertsen, M. S.; Reichman, D. R.: Microscopic theory of singlet exciton fission. II. Application to pentacene dimers and the role of superexchange. *J. Chem. Phys.* **2013**, *138*, 114103.

(68) Alguire, E. C.; Subotnik, J. E.; Damrauer, N. H.: Exploring Non-Condon Effects in a Covalent Tetracene Dimer: How Important Are Vibrations in Determining the Electronic Coupling for Singlet Fission? *J. Chem. Phys. A.* **2015**, *119*, 299-311.

(69) Smith, M. B.; Michl, J.: Recent Advances in Singlet Fission. *Ann. Rev. Phys. Chem.* **2013**, *64*, 361-386.

(70) Wang, L.; Olivier, Y.; Prezhdo, O. V.; Beljonne, D.: Maximizing Singlet Fission by Intermolecular Packing. *J. Phys. Chem. Lett.* **2014**, *5*, 3345-3353.

(71) Yost, S. R.; Lee, J.; Wilson, M. W. B.; Wu, T.; McMahon, D. P.; Parkhurst, R. R.; Thompson, N. J.; Congreve, D. N.; Rao, A.; Johnson, K.; Sfeir, M. Y.; Bawendi, M. G.; Swager, T. M.; Friend, R. H.; Baldo, M. A.; Van Voorhis, T.: A transferable model for singlet-fission kinetics. *Nat. Chem.* **2014**, *6*, 492-497.

(72) Parker, S. M.; Seideman, T.; Ratner, M. A.; Shiozaki, T.: Model Hamiltonian Analysis of Singlet Fission from First Principles. *J. Phys. Chem. C.* **2014**, *118*, 12700-12705.

(73) Teichen, P. E.; Eaves, J. D.: Collective aspects of singlet fission in molecular crystals. *The J. Chem. Phys.* **2015**, *143*, 044118.

(74) Teichen, P. E.; Eaves, J. D.: A Microscopic Model of Singlet Fission. *J. Phys. Chem. B.* **2012**, *116*, 11473-11481.

(75) Wu, Y.; Liu, K.; Liu, H.; Zhang, Y.; Zhang, H.; Yao, J.; Fu, H.: Impact of Intermolecular Distance on Singlet Fission in a Series of TIPS-Pentacene Compounds. *J. Phys. Chem. Lett.* **2014**, *5*, 3451-3455.

(76) Herz, J.; Buckup, T.; Paulus, F.; Engelhart, J.; Bunz, U. H. F.; Motzkus, M.: Acceleration of Singlet Fission in an Aza-Derivative of TIPS-Pentacene. *J. Phys. Chem. Lett.* **2014**, *5*, 2425-2430.

(77) Mirjani, F.; Renaud, N.; Gorczak, N.; Grozema, F. C.: Theoretical Investigation of Singlet Fission in Molecular Dimers: The Role of Charge Transfer States and Quantum Interference. *J. Phys. Chem. C.* **2014**, *118*, 14192-14199.

(78) Arias, D. H.; Ryerson, J. L.; Cook, J. D.; Damrauer, N. H.; Johnson, J. C.: Polymorphism influences singlet fission rates in tetracene thin films. *Chem. Sci.* **2016**, *7*, 1185-1191.

(79) Wan, Y.; Guo, Z.; Zhu, T.; Yan, S.; Johnson, J. C.; Huang, L.: Cooperative singlet and triplet exciton transport in tetracene crystals visualized by ultrafast microscopy. *Nat. Chem.* **2015**.

(80) Schwerin, A. F.; Johnson, J. C.; Smith, M. B.; Sreearunothai, P.; Popovic, D.; Cerny, J.; Havlas, Z.; Paci, I.; Akdag, A.; MacLeod, M. K.; Chen, X. D.; David, D. E.; Ratner, M. A.; Miller, J. R.; Nozik, A. J.; Michl, J.: Toward Designed Singlet Fission: Electronic States and Photophysics of 1,3-Diphenylisobenzofuran. *J. Phys. Chem. A.* **2010**, *114*, 1457-1473.

(81) Johnson, J. C.; Akdag, A.; Zamadar, M.; Chen, X. D.; Schwerin, A. F.; Paci, I.; Smith, M. B.; Havlas, Z.; Miller, J. R.; Ratner, M. A.; Nozik, A. J.; Michl, J.: Toward Designed Singlet Fission: Solution Photophysics of Two Indirectly Coupled Covalent Dimers of 1,3-Diphenylisobenzofuran. *J. Phys. Chem. B.* **2013**, *117*, 4680-4695.

(82) Johnson, J. C.; Reilly, T. H.; Kanarr, A. C.; van de Lagemaat, J.: The Ultrafast Photophysics of Pentacene Coupled to Surface Plasmon Active Nanohole Films. *J. Phys. Chem. C.* **2009**, *113*, 6871-6877.

(83) Marciniak, H.; Pugliesi, I.; Nickel, B.; Lochbrunner, S.: Ultrafast Singlet and Triplet Dynamics in Microcrystalline Pentacene Films. *Phys. Rev. B.* **2009**, *79*.

(84) Rao, A.; Wilson, M. W. B.; Hodgkiss, J. M.; Albert-Seifried, S.; Bassler, H.; Friend, R. H.: Exciton Fission and Charge Generation via Triplet Excitons in Pentacene/C-60 Bilayers. *J. Am. Chem. Soc.* **2010**, *132*, 12698-12703.

(85) Congreve, D. N.; Lee, J.; Thompson, N. J.; Hontz, E.; Yost, S. R.; Reusswig, P. D.; Bahlke, M. E.; Reineke, S.; Van Voorhis, T.; Baldo, M. A.: External Quantum Efficiency Above 100% in a Singlet-Exciton-Fission–Based Organic Photovoltaic Cell. *Science.* **2013**, *340*, 334-337.

(86) Albrecht, W. G.; Michelbeyerle, M. E.; Yakhot, V.: Exciton Fission in Excimer Forming Crystal - Dynamics of an Excimer Buildup in Alpha-Perylene. *Chem. Phys.* **1978**, *35*, 193-200.

(87) Voigt, M.; Langner, A.; Schouwink, P.; Lupton, J. M.; Mahrt, R. F.; Sokolowski, M.: Picosecond Time Resolved Photoluminescence Spectroscopy of a Tetracene Film on Highly Oriented Pyrolytic Graphite: Dynamical Relaxation, Trap Emission, and Superradiance. *J. Chem. Phys.* **2007**, *127*.

(88) Roberts, S. T.; McAnally, R. E.; Mastron, J. N.; Webber, D. H.; Whited, M. T.; Brutchey, R. L.; Thompson, M. E.; Bradforth, S. E.: Efficient Singlet Fission Discovered in a Disordered Acene Film. *J. Am. Chem. Soc.* **2012**, *134*, 6388-6400.

(89) Dillon, R. J.; Piland, G. B.; Bardeen, C. J.: Different Rates of Singlet Fission in Monoclinic versus Orthorhombic Crystal Forms of Diphenylhexatriene. *J. Am. Chem. Soc.* **2013**, *135*, 17278-17281.

(90) Balandier, J. Y.; Henry, N.; Arlin, J. B.; Sanguinet, L.; Lemaur, V.; Niebel, C.; Chattopadhyay, B.; Kennedy, A. R.; Leriche, P.; Blanchard, P.; Cornill, J.; Geerts, Y. H.: Synthesis and Characterization of Isomerically Pure anti- and syn-Anthradiindole Derivatives. *Org. Lett.* **2013**, *15*, 302-305.

(91) Bernstein, J.: Polymorphism - A Perspective. *Cryst. Growth Des.* **2011**, *11*, 632-650.

(92) Bruker AXS Inc. APEX2 V2012.10-0. Madison, WI, USA. **2012**.

(93) Bruker AXS Inc. SAINT V8.27b. Madison, WI, USA. **2012**.

(94) Sheldrick, G. M.: SADABS V2008/2. University of Göttingen, Göttingen, Germany. **2008**.

(95) Sheldrick, G. M.: A Short History of SHELX. *Acta Crystallogr. A* **2008**, *64*, 112-122.

(96) Sheldrick, G. M.: SHELXS-97. University of Göttingen: Göttingen, Germany. **2008**.

(97) Sheldrick, G. M.: SHELXL-97. University of Göttingen: Göttingen, Germany. **2008**.

(98) Bruker AXS Inc. APEX2 V2.1-4, SAINT V734A. Madison, WI, USA. **2007**.

(99) Altomare, A.; Cascarano, G.; Giacovazzo, G.; Guagliardi, A.; Burla, M. C.; Polidori, G.; Camalli, M.: SIR92 - A Program for Automatic Solution of Crystal Structures by Direct Methods. *J. Appl. Crystallogr.* **1994**, *27*, 435-436.

(100) Sheldrick, G. M.: SHELXS-97. University of Göttingen, Göttingen, Germany. **1997**.

(101) Ditchfield, R.; Hehre, W. J.; Pople, J. A.: Self-Consistent Molecular-Orbital Methods. IX. An Extended Gaussian-Type Basis for Molecular-Orbital Studies of Organic Molecules. *J. Chem. Phys.* **1971**, *54*, 724.

(102) Crawford, T. D.; Sherrill, C. D.; Valeev, E. F.; Fermann, J. T.; King, R. A.; Leininger, M. L.; Brown, S. T.; Janssen, C. L.; Seidl, E. T.; Kenny, J. P.; Allen, W. D.: PSI3: An Open-Source Ab Initio Electronic Structure Package. *J. Comput. Chem.* **2007**, *28*, 1610.

(103) Bergmann, W.; McLean, M. J.: Transannular Peroxides. *Chem. Rev.* **1941**, *28*, 367-394.

(104) Howard, J. A.; Mendenhall, G. D.: Autoxidation and Photooxidation of 1,3-Diphenylisobenzofuran: A Kinetic and Product Study. *Can. J. Chem.* **1975**, *53*, 2199-2201.

(105) Clark, J.; Chang, J.-F.; Spano, F. C.; Friend, R. H.; Silva, C.: Determining Exciton Bandwidth and Film Microstructure in Polythiophene Films Using Linear Absorption Spectroscopy. *Appl. Phys. Lett.* **2009**, *94*, 163306.

(106) Spano, F. C.: The Spectral Signatures of Frenkel Polarons in H- and J-Aggregates. *Acc. Chem. Res.* **2010**, *43*, 429-439.

(107) These concentrations are extracted by fitting the spectrum at a given pump-probe delay with the expression d*([S1]*eS1 + [T1]*eT1 - [S0]*eS0), where d is the film thickness, taken as 100 nm for all of the fitting done in this report.

(108) The error in [T1] reflects the variability in the extracted [T1] in the time window of 160-170 ps, well after T1 is fully formed. This variability in [T1] arises from instrumental noise, primarily due to instability in the pump and probe power. A similar error is not presented for [S1] because this state depopulates rapidly.

(109) Johnson, J. C.; Nozik, A. J.; Michl, J.: High Triplet Yield from Singlet Fission in a Thin Film of 1,3-Diphenylisobenzofuran. *J. Am. Chem. Soc.* **2010**, *132*, 16302-16303.

(110) Roberts, S. T.; McAnally, R. E.; Mastron, J. N.; Webber, D. H.; Whited, M. T.; Brutchey, R. L.; Thompson, M. E.; Bradforth, S. E.: Efficient Singlet Fission Discovered in a Disordered Acene Film. *J. Am. Chem. Soc.* **2012**, *134*, 6388-6400.

(111) For these films it can be difficult to assign a definitive rate constant for triplet fusion because the films undergo photodamage at higher fluences, which can manifest as a decay in the T1-Tn signal that looks like triplet fusion.

(112) Ryerson, J.; Schrauben, J.; Ferguson, A.; Sahoo, S.; Naumov, P.; Havlas, Z.; Michl, J.; Nozik, A. J.; Johnson, J. C.: Two Thin Film Polymorphs of The Singlet Fission Compound 1,3-diphenylisobenzofuran. J. Phys. Chem. C. **2014**, *118*, 12121-12132.

(113) Spano, F. C.: Excitons in conjugated oligomer aggregates, films, and crystals. *Ann. Rev. Phys. Chem.* **2006**; Vol. 57; pp 217-243.

(114) Spano, F. C.: The Spectral Signatures of Frenkel Polarons in H- and J-Aggregates. *Acc. Chem. Res.* **2010**, *43*, 429-439.

(115) Lim, S. H.; Bjorklund, T. G.; Spano, F. C.; Bardeen, C. J.: Exciton delocalization and superradiance in tetracene thin films and nanoaggregates. *Phys. Rev. Lett.* **2004**, *92*.

(116) Seko, T.; Ogura, K.; Kawakami, Y.; Sugino, H.; Toyotama, H.; Tanaka, J.: Excimer emission of anthracene, perylene, coronene and pyrene microcrystals dispersed in water. *Chem. Phys. Lett.* **1998**, *291*, 438-444.

(117) Albrecht, W. G.; Michelbeyerle, M. E.; Yakhot, V.: Exciton Fission in Excimer Forming Crystal - Dynamics of an Excimer Buildup in Alpha-Perylene. *Chem. Phys.* **1978**, *35*, 193-200.

(118) Albrecht, W. G.; Michelbeyerle, M. E.; Yakhot, V.: Exciton Fission in Excimer-Forming Crystal Dynamics of Excimer Buildup. *J. Lumin.* **1979**, *20*, 147-149.

(119) Schwerin, A. F.; Johnson, J. C.; Smith, M. B.; Sreearunothai, P.; Popovic, D.; Cerny, J.; Havlas, Z.; Paci, I.; Akdag, A.; MacLeod, M. K.; Chen, X. D.; David, D. E.; Ratner, M. A.; Miller, J. R.; Nozik, A. J.; Michl, J.: Toward Designed Singlet Fission: Electronic States and Photophysics of 1,3-Diphenylisobenzofuran. *J. Phys. Chem. A.* **2010**, *114*, 1457-1473.

(120) Ma, L.; Zhang, K.; Kloc, C.; Sun, H.; Soci, C.; Michel-Beyerle, M. E.; Gurzadyan, G. G.: Fluorescence from rubrene single crystals: Interplay of singlet fission and energy trapping. *Phys. Rev. B.* **2013**, *87*, 201203.

(121) Ma, L.; Zhang, K. K.; Kloc, C.; Sun, H. D.; Michel-Beyerle, M. E.; Gurzadyan, G. G.: Singlet fission in rubrene single crystal: direct observation by femtosecond pump-probe spectroscopy. *Phys. Chem. Chem. Phys.* **2012**, *14*, 8307-8312.

(122) Smith, M.; Michl, J.: Singlet Fission. *Chem. Rev.* **2010**, *110*, 6891.

(123) Grumstrup, E. M.; Johnson, J. C.; Damrauer, N. H.: Enhanced Triplet Formation in Polycrystalline Tetracene Films by Femtosecond Optical-Pulse Shaping. *Phys. Rev. Lett.* **2010**, *105*.

(124) Tayebjee, M. J. Y.; Clady, R. G. C. R.; Schmidt, T. W.: The exciton dynamics in tetracene thin films. *Phys. Chem. Chem. Phys.* **2013**, *15*, 14797-14805.

(125) The diffusion length in tetracene crystals increases exponentially as the temperature is lowered (G. Vaubel and H. Baessler, Mol. Cryst. Liq. Cryst., 1970, 12, 47). In contrast, exciton diffusion in conjugated polymers (O.V. Mikhnenko, F. Cordella, et al. J. Phys. Chem. B. 2008, 112, 11601) is temperature-independent at low temperatures (4-150 K), and temperature-dependent at higher temperatures, arising from activated hopping.

(126) Wilson, M. W. B.; Rao, A.; Johnson, K.; Gélinas, S.; di Pietro, R.; Clark, J.; Friend, R. H.: Temperature-Independent Singlet Exciton Fission in Tetracene. *J. Am. Chem. Soc.* **2013**, *135*, 16680-16688.

(127) Kakudate, T.; Yoshimoto, N.; Saito, Y.: Polymorphism in Pentacene Thin Films on SiO2 Substrate. *Appl. Phys. Lett.* **2007**, *90*, 081903.

(128) LBNL: X-Ray Attenuation Length. *LBNL Center for X-Ray Optics: X-Ray Database* **2010**, *http://www.cxro.lbl.gov/*.

(129) Salammal, S. T.; Balandier, J. Y.; Arlin, J. B.; Olivier, Y.; Lemaur, V.; Wang, L. J.; Beljonne, D.; Cornil, J.; Kennedy, A. R.; Geerts, Y. H.; Chattopadhyay, B.: Polymorphism in Bulk and Thin Films: The Curious Case of Dithiophene-DPP(Boc)-Dithiophene. *J. Phys. Chem. C.* **2014**, *118*, 657-669.

(130) Mobus, M.; Karl, N.; Kobayashi, T.: Structure of Perylene-Tetracarboxylic-Dianhydride Thin-Films on Alkali-Halide Crystal Substrates. *J. Cryst. Growth.* **1992**, *116*, 495-504.

(131) Leonhardt, M.; Mager, O.; Port, H.: Two-Component Optical Spectra in Thin PTCDA Films Due to the Coexistence of Alpha- and Beta-Phase. *Chem. Phys. Lett.* **1999**, *313*, 24-30.

(132) Ferguson, A. J.; Jones, T. S.: Photophysics of PTCDA and Me-PTCDI Thin Films: Effects of Growth Temperature. *J. Phys. Chem. B.* **2006**, *110*, 6891-6898.

(133) Sakurai, T.; Hayakawa, S.: Optical-Properties of Tetracene Evaporated-Films. *Jap. J. Appl. Phys.* **1974**, *13*, 1733-1740.

(134) Scheblykin, A. G.; Bataiev, M. M.; Auweraer, M. V. d.; Vitukhnovsky, A. G.: Dimensionality and Temperature Dependence of the Radiative Lifetime of J-Aggregates with Davydov Splitting of the Exciton Band. *Chem. Phys. Lett.* **2000**, *316*.

(135) Nichols, V. M.; Rodriguez, M. T.; Piland, G. B.; Tham, F.; Nesterov, V. N.; Youngblood, W. J.; Bardeen, C. J.: Assessing the Potential of Peropyrene as a Singlet Fission Material: Photophysical Properties in Solution and the Solid State. *J. Phys. Chem. C.* **2013**, *117*.

(136) Chakraborty, T.; Lim, E. C.: Dual Fluorescence from the Photoexcited Vanderwaals Dimer of Dibenzofuran in a Supersonic Jet - Intermediate-Case Level Structure of the Coupling between the Dimer Excited-State and the Lower-Lying Excimer State. *Chem. Phys. Lett.* **1993**, *207*, 99-104.

(137) Piuzzi, F.; Dimicoli, I.; Mons, M.; Millie, P.; Brenner, V.; Zhao, Q.; Soep, B.; Tramer, A.: Spectroscopy, Dynamics and Structures of Jet Formed Anthracene Clusters. *Chem. Phys.* **2002**, *275*, 123-147.

(138) Yip, W. T.; Levy, D. H.: Excimer/Exciplex Formation in van der Waals Dimers of Aromatic Molecules. *J. Phys. Chem.* **1996**, *100*, 11539-11545.

(139) Harada, J.; Ogawa, K.: Pedal Motion in Crystals. *Chem. Soc. Rev.* **2009**, *38*, 2244-2252.

(140) Natarajan, A.; Mague, J. T.; Venkatesan, K.; Arai, T.; Ramamurthy, V.: Volume-Demanding Cis-Trans Isomerization of 1,2-Diaryl Olefins in the Solid State. *J. Org. Chem.* **2006**, *71*, 1055-1059.

(141) Furube, A.; Murai, M.; Tamaki, Y.; Watanabe, S.; Katoh, R.: Effect of Aggregation on the Excited-State Electronic Structure of Perylene Studied by Transient Absorption Spectroscopy. *J. Phys. Chem. A.* **2006**, *110*, 6465-6471.

(142) Sumi, H.: 2 Kinds of Excimers in Alpha-Perylene and Pyrene Crystals - Origin of Y and V Emissions. *Chem. Phys.* **1989**, *130*, 433-449.

(143) Johnson, J. C.; Nozik, A. J.; Michl, J.: The Role of Chromophore Coupling in Singlet Fission. *Acc. Chem. Res.* **2013**, *46*, 1290-1299.

(144) Sondermann, U.; Kutoglu, A.; Bässler, H.: X-ray Diffraction Study of the Phase Transition in Crystalline Tetracene. *J. Phys. Chem.* **1985**, *33*, 1735-1741.

(145) Venuti, E.; Della Valle, R. G.; Farina, L.; Brillante, A.; Masino, M.; Girlando, A.: Phonons and structures of tetracene polymorphs at low temperature and high pressure. *Phys. Rev. B.* **2004**, *70*, 104106.

(146) Schatschneider, B.; Monaco, S.; Tkatchenko, A.; Liang, J. J.: Understanding the Structure and Electronic Properties of Molecular Crystals Under Pressure: Application of Dispersion Corrected DFT to Oligoacenes. *J. Phys. Chem. A.* **2013**, *117*, 8323-8331.

(147) Hofberger, W.: Structure and Optical Properties of Polycrystalline Evaporated Tetracene Films. *Phys. Status Solidi A.* **1975**, *30*, 271-278.

(148) Wilson, M. W. B.; Rao, A.; Johnson, K.; Gélinas, S.; Di Pietro, R.; Clark, J.; Friend, R. H.: Temperature-Independent Singlet Exciton Fission in Tetracene. *J. Am. Chem. Soc.* **2013**, *135*, 16680-16688.

(149) Sbastian, L.; Weiser, G.; Bassler, H.: Charge transfer transitions in solid tetracene and pentacene studied by electroabsorption. *Chem. Phys.* **1981**, *61*, 125-135.

(150) Leonat, L.; Sbarcea, G.; Branzoi, I. V.: Cyclic Voltammetry for Energy Levels Estimation of Organic Materials. *U.P.B. Sci. Bell. B.* **2013**, *75*, 111-118.

(151) Melo, J. S. d.; Rondao, R.; Burrows, H. D.; Melo, M. J.; Navaratnam, S.; Edge, R.; Voss, G.: Photophysics of an Indigo Derivative (Keto and Leuco Structures) with Singular Properties. *J. Phys. Chem. A.* **2006**, *110*, 13653-13661.

(152) Valiev, M.; Bylaska, E. J.; Govind, N.; Kowalski, K.; Straatsma, T. P.; Dam, H. J. J. v.; Wang, D.; Nieplocha, J.; Apra, E.; Windus, T. L.; Jong, W. A. d.: NWChem: A Comprehensive and Scalable Open-Source Solution for Large Scale Molecular Simulations. *Comput. Phys. Commun.* **2010**, *181*.

(153) Mayer, M. F.; Nakashima, S.; Zimmerman, S. C.: Synthesis of a Soluble Ureido-Naphthyridine Oligomer that Self-Associates via Eight Contiguous Hydrogen Bonds. *Org. Lett.* **2005**, *7 (14)*, 3005-3008.

(154) Hahn, B.; Köpke, B.; Voß, J.: Darstellung von Diaryl- und Aryl-tert-butyl-α-thioxoketonen. *Liebigs Ann. Chem.* **1981**, 10-19.

(155) Sheldrick, G. M.: A Short History of SHELX. *Acta Crystallogr. A.* **1990**, *46*, 467-473.

(156) Patra, A.; Chandaluri, C. G.; Radhakrishnan, T. P.: Optical Materials Based on Molecular Nanoparticles. *Nanoscale.* **2011**, *4*, 343-359.

(157) Mastron, J. N.; Roberts, S. T.; McAnally, R. E.; Thompson, M. E.; Bradforth, S. E.: Aqueous Colloidal Acene Nanoparticles: A New Platform for Studying Singlet Fission. *J. Phys. Chem. B.* **2013**, *117*, 15519-15526.

(158) Kim, H. Y.; Bjorklund, T. G.; Lim, S.-H.; Bardeen, C. J.: Spectroscopic and Photocatalytic Properties of Organic Tetracene Nanoparticles in Aqueous Solution. *Langmuir.* **2003**, *19*, 3941-3946.

(159) Fu, H.; Xiao, D.; Yao, J.; Yang, G.: Nanofibers of 1,3-Diphenyl-2-pyrazoline Induced by Cetyltrimethylammonium Bromide Micelles. *Angew. Chem. Int. Ed.* **2003**, *42*, 2883-2886.

(160) Hu, J.-S.; Guo, Y.-G.; Liang, H.-P.; Wan, L.-J.; Jiang, L.: Three-Dimensional Self-Organization of Supramolecular Self-Assembled Porphyrin Hollow Hexagonal Nanoprisms. *J. Am. Chem. Soc.* **2005**, *127*, 17090-17095.

(161) Nichols, V. M.; Broch, K.; Schreiber, F.; Bardeen, C. J.: Excited-State Dynamics of Diindenoperylene in Liquid Solution and in Solid Films. *J. Phys. Chem. C.* **2015**, *119*, 12856-12864.

(162) Liu, H.; Nichols, V. M.; Shen, L.; Jahansouz, S.; Chen, Y.; Hanson, K. M.; Bardeen, C. J.; Li, X.: Synthesis and Photophysical Porperties of a "Face-to-Face" Stacked Tetracene Dimer. *Phys. Chem. Chem. Phys.* **2015**, *17*, 6523-6531.

(163) Schrauben, J. N.; Zhao, Y.; Mercado, C.; Dron, P. I.; Ryerson, J. L.; Michl, J.; Zhu, K.; Johnson, J. C.: Photocurrent Enhanced by Singlet Fission in a Dye-Sensitized Solar Cell. *ACS Appl. Mater. Interfaces.* **2015**, *7*, 2286-2293.

(164) Ryerson, J. L.; Stepp, B. R.; Dron, P.; Arias, D. H.; Smith, M. B.; Kaleta, J.; Teat, S. J.; Havlas, Z.; Wahab, A.; Ludvík, J.; Głowackie, E.; Irimia-Vladu, M.; Monkowius, U.; Michl, J.; Nozik, A. J.; Johnson, J. C.: Structural and Photophysical Characterization of Indigo-based Derivatives for Singlet Fission. *Phys. Chem. Chem. Phys.* **2016**, In Preparation.